

NAVAL POSTGRADUATE SCHOOL Monterey, California

AD-A226 736



DTIC
ELECTE
SEP 27, 1990
S B D

DISSERTATION

APPLICATION OF CHAOS METHODS
TO HELICOPTER VIBRATION REDUCTION
USING HIGHER HARMONIC CONTROL

by

Martinus M. Sarigul-Klijn

March 1990

Dissertation Supervisor: Ramesh Kolar

Approved for public release; distribution is unlimited.

REPORT DOCUMENTATION PAGE				Form Approved OMB No 0704 0188	
1a REPORT SECURITY CLASSIFICATION Unclassified			1b RESTRICTIVE MARKINGS		
2a SECURITY CLASSIFICATION AUTHORITY			3 DISTRIBUTION AVAILABILITY OF REPORT Approved for public release; distribution is unlimited.		
2b DECLASSIFICATION/DOWNGRADING SCHEDULE					
4 PERFORMING ORGANIZATION REPORT NUMBER(S)			5 MONITORING ORGANIZATION REPORT NUMBER(S)		
6a NAME OF PERFORMING ORGANIZATION Naval Postgraduate School		6b OFFICE SYMBOL (If applicable) 67		7a NAME OF MONITORING ORGANIZATION Naval Postgraduate School	
6c ADDRESS (City, State, and ZIP Code) Monterey, CA 93943-5000			7b ADDRESS (City, State, and ZIP Code) Monterey, CA 93943-5000		
8a NAME OF FUNDING/SPONSORING ORGANIZATION		8b OFFICE SYMBOL (If applicable)		9 PROCUREMENT INSTRUMENT IDENTIFICATION NUMBER	
8c ADDRESS (City, State, and ZIP Code)			10 SOURCE OF FUNDING NUMBER		
			PROGRAM ELEMENT NO		PROJECT NO
			TASK NO		WORK UNIT ACCESSION NO
11 TITLE (Include Security Classification) APPLICATION OF CHAOS METHODS TO HELICOPTER VIBRATION REDUCTION USING HIGHER HARMONIC CONTROL					
12 PERSONAL AUTHOR(S) Sarigul-Klijn, Martinus M.					
13a TYPE OF REPORT PhD Dissertation		13b TIME COVERED FROM TO		14 DATE OF REPORT (Year, Month, Day) March 1990	
				15 PAGE COUNT 203	
16 SUPPLEMENTARY NOTES The views expressed in this dissertation are those of the author and do not reflect the official policy or position of the Department of Defense or the U. S. Government.					
17 COSATI CODES			18 SUBJECT TERMS (Continue on reverse if necessary and identify by block number)		
FIELD	GRO IP	SUB-GRO IP	Chaos, Higher Harmonic Control, Nonlinear dynamics, Strange attractor, Fractal dimension, Lyapunov exponent, Poincare section, Van der Pol plane, Control systems.		
19 ABSTRACT (Continue on reverse if necessary and identify by block number) Chaos is a discipline used in understanding complex nonlinear dynamics. The geometric and topological methods of Chaos theory are applied, for the first time, to the study of flight test data. Data analyzed is from the McDonnell Douglas OH-6A Higher Harmonic Control (HHC) test aircraft. HHC is an active control system used to suppress helicopter vibrations. Some of the first practical applications of Chaos methods are demonstrated with the HHC data. Although helicopter vibrations are mostly periodic, evidence of chaos was found. The presence of a strange attractor was shown by computing a positive Lyapunov exponent and computing a noninteger fractal correlation dimension. Also, a broad band Fourier spectrum and a well defined attractor in pseudo phase space are observed. A limit exists to HHC vibration reduction due to the presence of					
20 DISTRIBUTION/AVAILABILITY OF ABSTRACT <input checked="" type="checkbox"/> UNCLASSIFIED/UNLIMITED <input type="checkbox"/> SAME AS RPT <input type="checkbox"/> DTIC USERS			21 ABSTRACT SECURITY CLASSIFICATION Unclassified		
22a NAME OF RESPONSIBLE INDIVIDUAL Ramesh Kolar			22b TELEPHONE (Include Area Code) (408) 646-2936		22c OFFICE SYMBOL 67Kj

Unclassified

SECURITY CLASSIFICATION OF THIS PAGE

chaos. A new technique based on a relationship between the Chaos methods (the Poincare section and Van der Pol plane) and the vibration amplitude and phase was discovered. This newly introduced technique results in the following: 1) it gives the limits of HHC vibration reduction, 2) it allows rapid determination of best phase for a HHC controller, 3) it determines the minimum HHC controller requirement for any helicopter from a few minutes duration of flight test data, (for the OH-6A, a scheduled gain controller for HHC appears to be adequate for steady level flight), 4) it shows that the HHC controller transfer matrix is linear and repeatable when the vibrations are defined in the "Rotor Time Domain" and that the matrix is nonlinear and nonrepeatable when the vibrations are defined in the "Clock Time Domain."

This technique will reduce future HHC flight test requirements. Further, the technique does not require the helicopter to be equipped with HHC. These methods may be applicable to other vibration control and flight testing problems.

Accession For	
NTIS GRA&I	<input checked="checked" type="checkbox"/>
DTIC TAB	<input type="checkbox"/>
Unannounced	<input type="checkbox"/>
Justification	
By	
Distribution/	
Availability Codes	
Dist	Avail and/or Special
A-1	



Approved for public release; distribution is unlimited.

Application of Chaos Methods to Helicopter Vibration
Reduction Using Higher Harmonic Control

by

Martinus M. Sarigul-Klijn
Lieutenant Commander, United States Navy
B. S., U. S. Naval Academy, 1977
M. S., U. S. Naval Postgraduate School, 1988

Submitted in partial fulfillment of the
requirements for the degree of

DOCTOR OF PHILOSOPHY

from the

NAVAL POSTGRADUATE SCHOOL
March 1990

Author:

M. M. Sarigul-Klijn
Martinus M. Sarigul-Klijn

Approved by:

Gilles Cantin

Gilles Cantin
Professor of Mechanical
Engineering

Ramesh Kolar

Ramesh Kolar
Assistant Professor of
Aeronautics & Astronautics
Dissertation Supervisor

E. R. Wood

E. Roberts Wood
Professor of Aeronautics
& Astronautics

Approved by:

E. R. Wood
E. Roberts Wood, Chairman, Department of
Aeronautics and Astronautics

Approved by:

Harrison Shull
Provost/Academic Dean

D. D. Danielson

Donald D. Danielson
Associate Professor of
Mathematics

M. F. Platzer

Max F. Platzer
Professor of Aeronautics
& Astronautics

ABSTRACT

Application of Chaos Methods to Helicopter Vibration Reduction Using Higher Harmonic Control

by

Lcdr Martinus M. Sarigul-Klijn, USN

Chaos is a discipline used in understanding complex nonlinear dynamics. The geometric and topological methods of Chaos theory are applied, for the first time, to the study of flight test data. Data analyzed is from the McDonnell Douglas OH-6A Higher Harmonic Control (HHC) test aircraft. HHC is an active control system used to suppress helicopter vibrations. Some of the first practical applications of Chaos methods are demonstrated with the HHC data.

Although helicopter vibrations are mostly periodic, evidence of chaos was found. The presence of a strange attractor was shown by computing a positive Lyapunov exponent and computing a non-integer fractal correlation dimension. Also, a broad band Fourier spectrum and a well defined attractor in pseudo phase space are observed.

A limit exists to HHC vibration reduction due to the presence of chaos. A new technique based on a relationship between the Chaos methods (the Poincare section and Van der Pol plane) and the vibration amplitude and phase was discovered. This newly introduced technique results in the following: 1) it gives the limits of HHC vibration reduction, 2) it allows rapid determination of best phase for a HHC controller, 3) it determines the minimum HHC controller requirement for any helicopter from a few minutes duration of flight test data (for the OH-6A, a scheduled gain controller for HHC appears to be adequate for steady level flight), 4) it shows that the HHC controller transfer matrix is linear and repeatable when the vibrations are defined in the "Rotor Time Domain" and that the matrix is nonlinear and nonrepeatable when the vibrations are defined in the "Clock Time Domain."

This technique will reduce future HHC flight test requirements. Further, the technique does not require the helicopter to be equipped with HHC. These methods may be applicable to other vibration control and flight testing problems.

TABLE OF CONTENTS

I.	INTRODUCTION.....	1
	A. BACKGROUND.....	1
	B. OVERVIEW OF DISSERTATION.....	3
	FIGURE 1-1.....	6
II.	BACKGROUND - HELICOPTER VIBRATIONS.....	7
	A. PURPOSE.....	7
	B. FORCES IN THE ROTOR.....	7
	C. ROTOR DESIGN AND CONTROL.....	8
	D. ROTOR AS A FILTER.....	9
	E. OTHER SOURCES OF HELICOPTER VIBRATIONS.....	11
	F. SUMMARY.....	12
	FIGURE 2-1 & 2-2.....	13
III.	BACKGROUND - HIGHER HARMONIC CONTROL.....	15
	A. PURPOSE.....	15
	B. WHAT IS HHC ?.....	15
	C. CONTROLLERS.....	18
	D. PREVIOUS RESEARCH.....	22
	E. THE MCDONNELL DOUGLAS/NASA/ARMY HHC TEST PROGRAM.....	26
	FIGURES 3-1 TO 3-3.....	32
IV.	TIME DOMAIN ANALYSIS.....	35
	A. PURPOSE.....	35
	B. DIGITAL SIGNALS.....	35
	C. MEASUREMENTS IN THE TIME DOMAIN.....	37
	D. ERGODIC AND STATIONARY DATA.....	38
	E. SUMMARY.....	39
	FIGURES 4-1 TO 4-4.....	41
V.	ANALYSIS IN THE FREQUENCY DOMAIN.....	44
	A. PURPOSE.....	44
	B. FOURIER TRANSFORMS.....	44
	C. PARSEVAL'S THEOREM.....	46
	D. PHASE SPECTRUMS.....	46
	E. DIFFERENT METHODS FOR PSD's.....	47
	F. LIMITATIONS AND RESTRICTIONS.....	48
	G. SUMMARY.....	53
	FIGURES 5-1 TO 5-6.....	54
VI.	GEOMETRIC AND TOPOLOGICAL METHODS OF CHAOS.....	60
	A. PURPOSE AND INTRODUCTION.....	60
	B. ILLUSTRATIVE EXAMPLES.....	61
	C. TIME HISTORY.....	63
	D. FOURIER SPECTRUM.....	64
	E. THE 2-DIMENSIONAL PHASE PLANE.....	65
	F. TAKENS'S THEOREM.....	67
	G. 2-D PHASE PLANE AGAIN.....	71
	H. EMBEDDING TIME.....	71
	I. ENERGY IN THE PHASE PLANE.....	72
	J. 3-DIMENSIONAL PHASE SPACE.....	73
	K. POINCARÉ SECTION.....	75
	L. TOROIDAL PHASE SPACE.....	77
	M. POINCARÉ SECTIONS AGAIN.....	79

N.	VAN DER POL PLANE.....	79
O.	HIGHER DIMENSIONAL POINCARÉ SECTIONS.....	81
P.	LYAPUNOV EXPONENTS.....	82
Q.	STRANGE ATTRACTORS.....	85
R.	FRACTAL DIMENSION.....	87
S.	SUMMARY.....	90
	TABLE 6.1 AND FIGURES 6-1 TO 6-22.....	91
VII.	NATURE OF THE HHC CONTROLLER TRANSFER MATRIX...	114
A.	PURPOSE.....	114
B.	TRANSFER MATRIX.....	114
C.	SIGNIFICANCE OF POINCARÉ SECTION AND VAN DER POL PLANE.....	115
D.	COMPARISON OF TWO METHODS OF PLOTTING.....	117
E.	IMPLICATIONS.....	119
F.	CONCLUSION.....	120
	FIGURES 7-1 TO 7-4.....	121
VIII.	LIMITS OF HHC PERFORMANCE.....	125
A.	PURPOSE.....	125
B.	EFFECTS OF HHC.....	125
C.	PHASE DETERMINATION.....	127
D.	LINEAR MOVEMENT OF THE ATTRACTOR AND THE TRANSFER MATRIX.....	129
E.	LIMIT OF HHC PERFORMANCE.....	129
F.	SUMMARY.....	131
	FIGURES 8-1 TO 8-6.....	132
IX.	HHC CONTROLLERS.....	138
A.	PURPOSE.....	138
B.	REVIEW ON TYPES OF CONTROL SYSTEM.....	138
C.	DETERMINATION OF MINIMUM CONTROLLER FROM FLIGHT TEST.....	139
D.	FUTURE APPLICATION OF CHAOS METHODS ON HHC.....	140
E.	SUMMARY.....	141
	FIGURES 9-1 AND 9-2.....	142
X.	THE HUNT FOR CHAOTIC HELICOPTER VIBRATIONS.....	144
A.	PURPOSE.....	144
B.	PRELIMINARIES.....	144
C.	AIRCRAFT FLIGHT TEST MEASUREMENTS.....	146
D.	SEARCH FOR CHAOS.....	151
E.	CHAOS IN HELICOPTERS - WHAT DOES IT MEAN ?.....	156
F.	HOW ABOUT HHC ?.....	158
E.	SUMMARY	159
	FIGURES 10-1 TO 10-16.....	160
XI.	CONCLUSIONS AND SCOPE FOR FUTURE RESEARCH.....	176
	APPENDIX A - DESCRIPTION OF COMPUTER CODE.....	178
	APPENDIX B - HHC MEASUREMENT LIST.....	184
	LIST OF REFERENCES.....	187
	INITIAL DISTRIBUTION LIST.....	194

ACKNOWLEDGMENTS

I like to recognize the assistance of my dissertation supervisor, Prof. Ramesh Kolar, who managed to keep up with me as we explored a new topic. I like to thank Prof. E. Roberts Wood, for suggesting the topic of Higher Harmonic Control. From McDonnell Douglas Helicopter Company, I like to acknowledge the assistance of Dr. Friedrich Straub who authorized the HHC data transfer to the Naval Postgraduate School, Mr. Roger Gould who converted the data from PCM format to VAX format, and Mr. Don Duel who provided me with valuable insight on time and frequency domain analysis. I like to thank all my committee members, including Prof. Gilles Cantin, Prof. Donald Danielson, and Prof. Max Platzer, who provided me with important comments which are now included in the final version.

Finally, I like to acknowledge the assistance of my wife, Prof. Nesrin Sarigul-Klijn of the University of California, Davis, who proofread my work and provided important advice and moral support. I like to also thank Nesrin's parents who took care of our 3 month old son, Deniz, while I finished this dissertation.

I. INTRODUCTION

A. BACKGROUND

Chaos is a motion which is sensitive to initial conditions. Figure 1-1 depicts chaotic motion. From nearly the same starting point, trajectories which represent the motion of a dynamical system grow farther and farther apart until all resemblance disappears. The study of chaotic motion like this has inspired new methods of analysis. Some methods, like the phase plane, have their origin as far back as 1904 with Henri Poincare. Other methods, like the pseudo phase space, were discovered as recently as 1980 by Floris Takens. The concept of chaos and these geometric methods have revolutionized the investigation of problems in nonlinear dynamics.

The accurate prediction of helicopter vibrations from first principles has been the goal of helicopter dynamic analysis. NASA's joint-industry DAMVIBS program [Ref 1.1] shows encouraging progress. Presently, one way to get accurate vibration data is from a flight survey of an instrumented helicopter. The literature shows that only time domain and frequency domain spectral analysis methods are used to study flight test data.

The work in this dissertation is devoted to the analysis of flight test data using the geometric and topological methods of chaos, and is believed to be the first such engineering application of the science of chaos. The data analyzed is obtained from the McDonnell Douglas Helicopter Company. They provided the flight test data from the McDonnell Douglas/NASA/Army OH-6A Higher Harmonic Control (HHC) test helicopter. HHC is an active control system used to suppress helicopter vibrations. This OH-6A helicopter demonstrated the first successful application of HHC in a series of flight tests during 1982 to 1984. The aircraft was heavily instrumented and the results were digitized and stored on magnetic tapes. McDonnell Douglas retrieved these magnetic tapes from archives. They then translated them from a flight test pulse code modulation (PCM) format to a ASCII format, readable by a Digital VAX series computer. This data was provided to the Naval Postgraduate School for in-depth analysis.

During the course of this research, a comprehensive Fortran program was developed to analyze experimental data using a wide variety of classical as well as the new chaos methods. These new geometric and topological methods are completely independent of all preconceived helicopter models. Only actual measured data are used. The program includes classical time and frequency domain

analysis, including statistical estimates. The geometric and topological methods allow analysis in 2-D and 3-D phase-space, toroidal phase space, Poincare sections (time strobed and space strobed), and the Van der Pol plane. Further, options to characterize attractors by computation of the fractal correlation dimension and Lyapunov exponents are provided.

Some of the first practical applications of the chaos methods are demonstrated using the HHC data. Many of the ideas presented here may be applicable to other vibration control and flight test data analysis problems.

B. OVERVIEW OF DISSERTATION

The second and third chapters cover background. Chapter two provides an overview of helicopter dynamics. The source of helicopter vibrations is also addressed. The third chapter discusses aspects of Higher Harmonic Control (HHC). It presents the mechanism of HHC, HHC controllers and control law, some pertinent research, and sketches the details of the McDonnell Douglas flight test program.

The fourth and fifth chapters cover the classical time and frequency domain methods of analysis. These methods are the current state-of-the-art in flight test data reduction and interpretation.

The sixth chapter describes the geometric and topological methods of chaos. Only those methods with applicability to flight test data reduction are given.

Chapter seven presents the analysis of HHC data. Some researchers have shown that the transfer matrix, 'T,' in the HHC control law may be linear and repeatable while other researchers have shown that it may be non-linear and non-repeatable. This chapter shows how the transfer matrix is linear and repeatable when vibrations are defined in the rotor time domain, while it is non-linear and non-repeatable when vibrations are defined in the clock time domain.

The results from the chaos methods indicate a lower limit to HHC vibration reduction due to chaos introduced by the nonlinear nature of the dynamics. The eighth chapter discusses the two Chaos methods, the Poincare section and Van der Pol plane, that will reduce flight test requirements by showing the limits of HHC performance. The aircraft does not need a HHC system for these methods to work.

The characteristics of the 'T' matrix and how it changes with flight conditions determine the design of a control system. Chapter nine demonstrates, for the OH-6A, that a scheduled gain controller is adequate for steady level flight. A new technique is presented that provides insight into the design of the controller for a

helicopter, based on a few minutes duration of flight test data. The method does not require the aircraft to be equipped with a HHC system.

The tenth chapter discusses helicopter vibrations using classical and chaos methods. Although helicopter vibrations are mostly periodic, evidence of chaos was found in the form of a strange attractor. Chaos places a lower limit on HHC vibration reduction. Also, the determination of the exact nature of helicopter vibrations has important implications in helicopter simulations. Many helicopter simulation codes assume that the helicopter vibrations are periodic.

Chapter eleven summarizes the conclusions of this dissertation.

Appendix A gives a description of the program CHAOS, which was developed during the course of this research. Appendix B lists the available flight test measurements.

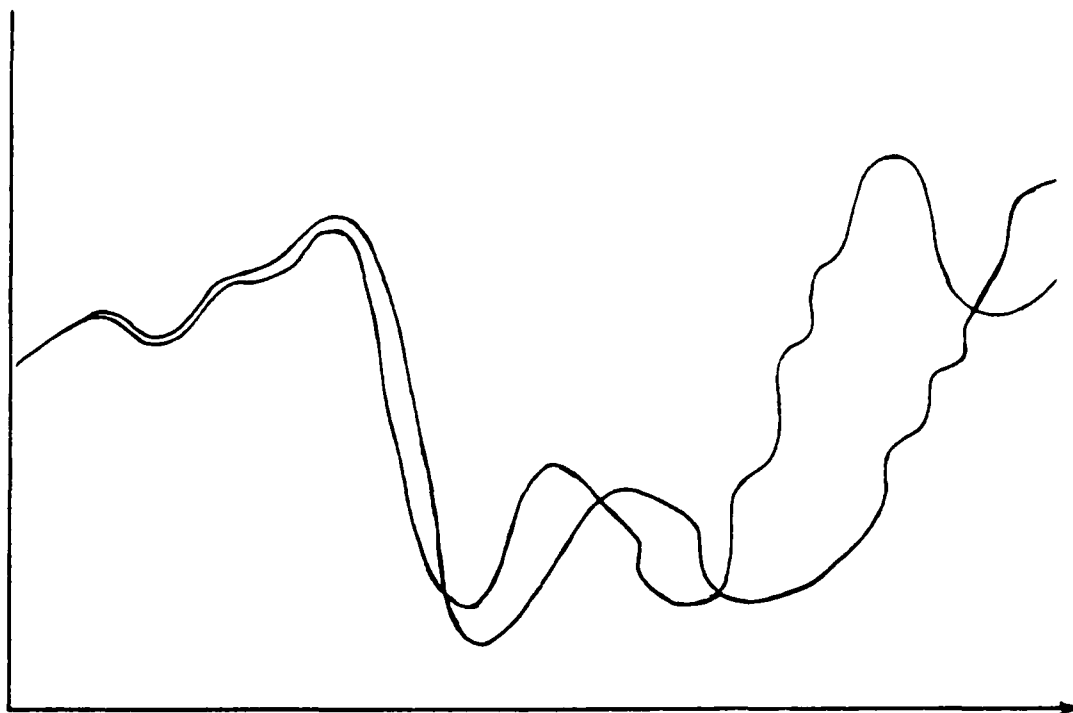


Figure 1-1. Chaotic Motion. Starting from the same starting point, two trajectories representing the motion of a chaotic system diverge exponentially until all resemblance disappears. Chaos is motion which has sensitive dependence on initial conditions.

II. BACKGROUND - HELICOPTER VIBRATIONS

A. PURPOSE

The purpose of this chapter is to review some aspects of helicopter vibrations.

B. FORCES IN THE ROTOR

The forces in the rotor blades are primarily periodic components of the rotor's rotational rate and its harmonics [Ref 2.1]. One per revolution or '1P' are the forces at the rotors rotational rate. Harmonics are multiples of this 1P; for example, 2P, 3P, 4P and so on are the second, third, and fourth harmonics, respectively. For the OH-6A, the rotor rotates at an average of 483 rpm or 8.05 Hertz. Hence the 1P is 8.05 Hertz, the 2P is 16.1 Hertz, the 3P is 24.15 Hertz and so on. Note the 1P, 2P, 3P and so on, are exact multiples of the rotor's rotational speed. In flight, the helicopter rotor operates at nearly a constant rotational rate, varying less than 2 percent. Since the rotor rotational speed varies slightly with time, then the frequencies associated with 1P, 2P, 3P and so on also vary a small amount with time and are not constant. The first 6 or so harmonics are important contributors to the vibrations of a helicopter.

The primary cause of the rotor blade vibratory forces is due to the asymmetric loading of the rotor blades in forward flight [Ref 2.1]. Forward flight causes the rotor blades to experience a constantly changing airflow. This causes a periodic variation of the rotor blade section angle of attack. In addition, each blade interacts with the vortices shed by other rotor blades. These varying air loads cause the blades to vibrate. A nonuniform inflow contributes to the vibration. Figure 2-1 from Prouty [Ref 2.2] illustrates the varying air loads. In addition, at high forward speeds the rotor blades will experience aerodynamic stall of the retreating blade and Mach compressibility effects on the advancing blade.

Figure 2-1 also provides the convention used to measure rotor azimuthal position. From this figure, note that zero degrees azimuth is over the tail boom, 90 degrees is on the starboard side (also known as the advancing blade), 180 degrees is over the nose, and 270 degrees on the port side (retreating blade).

C. ROTOR DESIGN AND CONTROL

The trend up to the 1970's was to use symmetric airfoils for rotor blades. For track and balance, they closely match each other in aerodynamic shape, stiffness, mass and inertia distribution. Also, airfoil sections

are designed to minimize control loads or changes of aerodynamic pitching moment with changes of blade section angle of attack. [Ref 2.3]

The rotor blade attachment to the hub is, typically, articulated. The blades can move freely normal to and in the plane of the rotor by the use of hinges or elastomeric bearings at the rotor hub. The motion normal to the plane of the rotor is called "flapping" while "lead-lag" is the motion in the plane of the rotor. Flapping and lead-lag motion prevent rotor blade bending moments from being transmitted to the hub. There are two other common mechanical attachments of the rotor blades to the rotor hub, in addition to the articulated rotor. These attachments are the teetering rotor and the hingeless rotor. They all accommodate the rotor blade flap and lag motion. The OH-6A uses an articulated rotor hub. Figure 2-2 presents a sketch of an articulated rotor hub. Control of the rotor blade is accomplished by changing the pitch of the rotor blade. The resulting change of rotor blade angle of attack changes the aerodynamic forces on the rotor.

D. ROTOR AS A FILTER

Flapping and lead-lag hinges at the rotor hub relieve bending moments, but shear forces still exist at the rotor hub attachment point. "Flapwise" root shears are

those forces normal to the plane of the rotor.

"Chordwise" root shears are those forces in the plane of the rotor. These forces sum at the rotor hub and form the loads transmitted to the fuselage.

Many of the root shear summations at the rotor hub are zero. This is because rotor blade root shears are periodic in nature (1P, 2P, 3P and so on) and because of the symmetric arrangement of the rotor blades about the rotor hub. The rotor acts as a filter, letting only a limited number of vibrations reach the fuselage [Ref 2.4]. In the case of a 4 bladed rotor, the only vibrating components reaching the fuselage is the 4P, 8P, 12P, etc. For a 4-bladed rotor:

3P and 5P flapwise blade root shears result in 4P hub pitching and rolling moments in the airframe.

4P flapwise blade root shears feed into the airframe as 4P vertical forces.

3P and 5P chordwise root shears produce 4P airframe hub forces in the fore and aft and lateral directions.

4P chordwise root shears result in 4P hub yawing moments.

The 4P is at about 32 hertz in the OH-6A. The higher harmonics on 4P (8P, 12P, 16P, etc.) will also filter from the rotor to the fixed fuselage system. The amplitudes of these forces are much lower than the 4P and

are often ignored in analysis. Notice that the force transmitted to the fuselage from the hub is not at the same frequency as the exciting frequency in the rotating system.

Some caveats apply to this filtering process. First this filtering works only for a perfectly symmetric rotor system. Asymmetries in the rotor blades can produce terms at frequencies other than the 4P. Also, maneuvering flight will lead to leakage of vibrations at frequencies other than the 4P to the fuselage. In fact Gunsallus et al. [Ref 2.5] demonstrated the capability of computing all the harmonics of the rotating rotor blade motion by measuring vibrations only in the fixed fuselage. Clearly the rotor is not a perfect filter. The filtering process allows components of all frequencies to pass to the fuselage.

These rotor hub forces are the primary cause of the fuselage vibrations. The rotor shakes the fuselage at the rotor hub attachment to the rotor mast, far above the fuselage. The fuselage will respond to these excitations and cause the pilot's seat to vibrate. Finally, the pilot's seat vibration causes the pilot to vibrate.

E. OTHER SOURCES OF HELICOPTER VIBRATIONS

Although the main rotor is the major source of helicopter vibrations, there are other sources. The tail

rotor, its drive shaft, the engine and transmission all produce vibration. The frequency of their contribution is usually much higher than the rotors. The impact of the rotor downwash on the fuselage is yet another source. Finally, the fuselage response to turbulence adds to the total vibration picture of the helicopter.

F. SUMMARY

The major source of vibration in a helicopter is the aerodynamic excitation that comes from the rotor. This vibration, in theory, is at a single frequency. The next chapter discusses a method of eliminating this vibration.

$$U_T = \Omega r + V \sin \psi$$

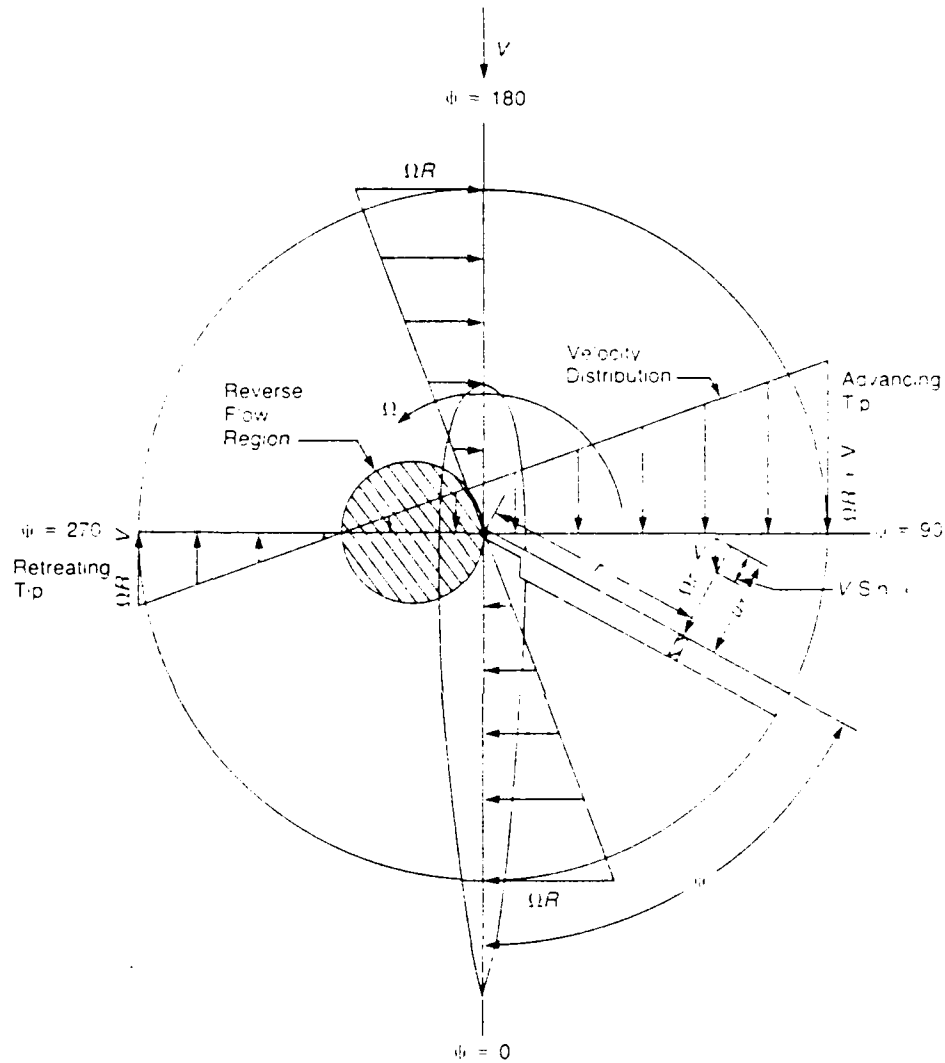


Figure 2-1. Airflow in Forward Flight. The velocity acting on a blade is a function of radial station, blade azimuth position, rotation of rotor, and forward speed of the helicopter [from Prouty (1986) with permission of PWS Publishers, Copyright 1986].

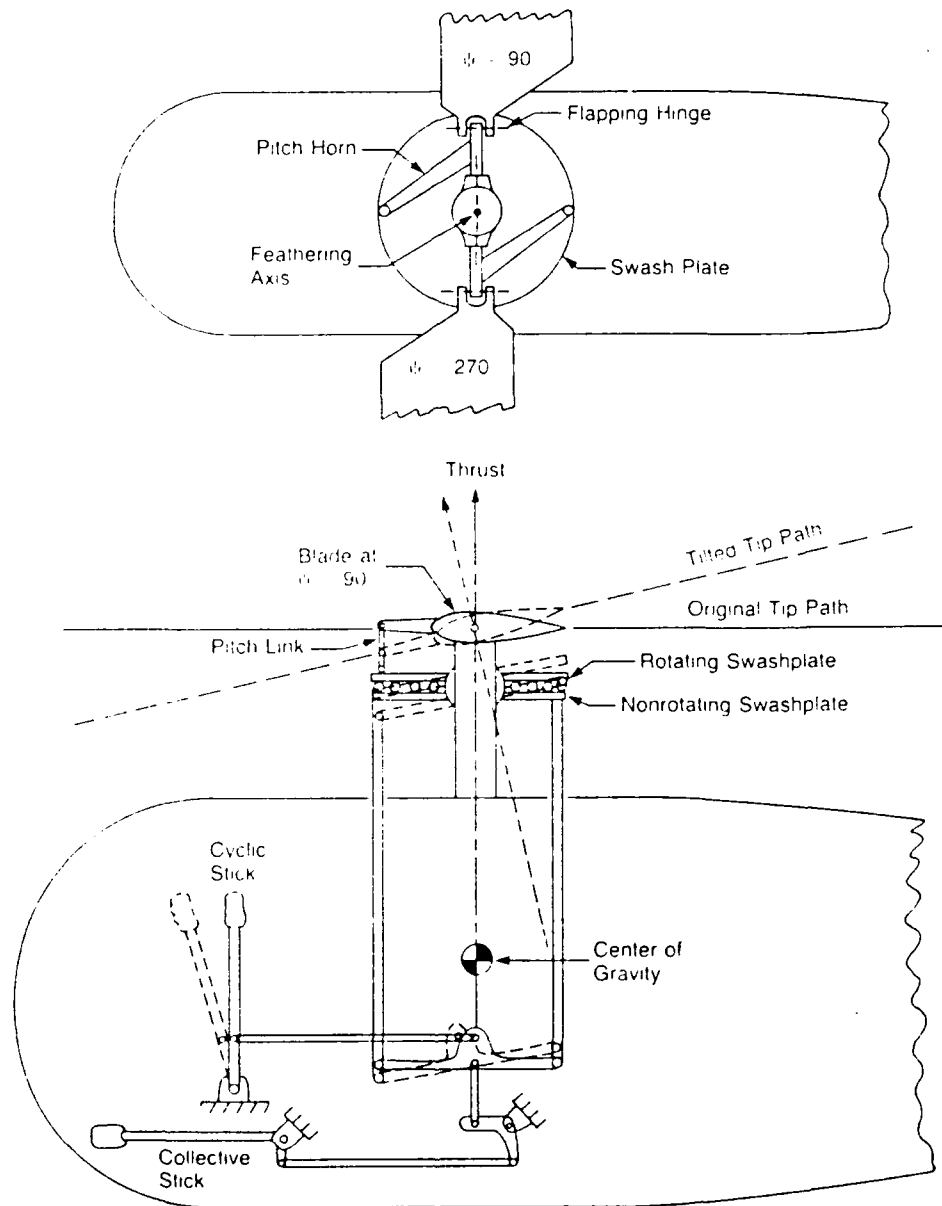


Figure 2-2. Schematic of Helicopter Control System.
 For clarity only two rotor blades are drawn [from Prouty (1986) with permission of PWS Publishers, Copyright 1986].

III. BACKGROUND - HIGHER HARMONIC CONTROL

A. PURPOSE

This chapter reviews Higher Harmonic Control (HHC). Also described are various controllers used for vibration control. A brief overview of research efforts in HHC is given followed by a description of the McDonnell Douglas/Army/NASA OH-6A HHC flight tests.

B. WHAT IS HHC ?

The rotor is the principal source of vibrations in a helicopter. Also, these vibrations are caused essentially at a single frequency. Active vibration suppression systems can counter single frequency vibrations. In contrast to other helicopter vibration control devices, such as fixed-tuned fuselage vibration absorbers, HHC alleviates vibration by modifying the excitation (aerodynamic loading) at the source. HHC is a computer controlled active vibration suppression system which counters, in the case of a 4-bladed rotor, the 4P vibration induced from the rotor. It continuously monitors vibrations caused by the rotor and suppresses them through high frequency rotor blade feathering. The feathering is at an integer multiple (higher harmonic) of

the rotor rotational rate. The name comes from this fact.

Two schemes currently exist for HHC. All flight tests to date and all wind tunnel tests but one, have used "direct HHC." In this scheme, HHC works through the existing flight control swashplate. The swashplate is a part of the helicopter control system. It transmits the control inputs from the stationary or fuselage frame to the rotor or rotating frame. The stationary portion of the swashplate is oscillated by actuators fixed to the fuselage with continuous variations of amplitude, frequency and phase. Certain combinations of these parameters result in significant reductions of rotor vibrations. The amplitude of swashplate excitation is usually small, in the order of 0.20 inches measured at the actuators. The swashplate is oscillated at a frequency equal to the number of rotor blades times the rotational rate. In the OH-6A this turns out to be the 4P or at approximately 32 hertz. The swashplate excitation generates new incremental airloads which cancel the vibratory blade loads that cause vibration. There are several modes of motion of the swashplate which may be described as follows:

The "lateral" mode refers to tilting the swashplate laterally or in side-to-side direction only.

The "longitudinal" mode refers to tilting the swashplate in the longitudinal direction or in the fore and aft direction only.

The "collective" mode refers to moving the swashplate collectively or in the up and down direction only.

Optimal vibration reduction is seen to occur with simultaneous application of lateral, longitudinal and collective swashplate excitation.

As explained earlier, the rotor acts as a filter. This process may also work in the opposite direction. Tilting or translating the stationary portion of a 4-bladed rotors swashplate at a 4P frequency results in blade feathering at frequencies of 3P, 4P, and 5P in the rotating system. This is summarized as follows:

4P collective swashplate movement results in 4P rotor blade feathering.

4P lateral or longitudinal swashplate movement results in 3P and 5P blade feathering.

By carefully varying the amount of collective, lateral, and longitudinal swashplate excitations any combination of 3P, 4P, and 5P blade feathering may be obtained.

The second approach is to control the pitch of each rotor blade independently. Known as "individual blade control" (IBC), each rotor blade has an individual electro-hydraulic actuator. Signals from sensors mounted

on the blades supply appropriate control commands. To transmit the pilot's commands requires a reliable means of going from the fixed to the rotating system. The IBC is seen to have one major advantage. It can control more than three swashplate degrees of freedom. For example, IBC for a four bladed rotor can control more than just the 3P, 4P, and 5P frequencies. However, concerns of reliability prevent its current implementation on any full scale helicopter.

C. CONTROLLERS

A control system (controller) is responsible for the swashplate tilting in a direct HHC system. The objective of the controller is to reduce helicopter vibrations by determining the proper amount of lateral, longitudinal, and collective swashplate excitation. Best vibration reduction may be obtained by exciting all three modes of swashplate tilting simultaneously. In a direct HHC system, the controller attempts to reduce the vibrations in a "measured response." Usually, the measured response is the vibrations under the pilot's seat. In contrast, in IBC HHC, the measured response is always located on the rotor blade.

Helicopters can vibrate in three different directions: fore and aft (longitudinally), sideways (laterally) and up and down (vertically). To describe a

single frequency vibration requires two quantities, an amplitude and a phase. However, any single frequency vibration can be broken into a sine and cosine part. It is simpler to use the two amplitudes of the sine and cosine parts in numerical computations. It follows, then, that six quantities, two each for vertical, lateral, and longitudinal, respectively, is enough to describe helicopter vibrations. Using this concept, most wind tunnel and flight tests use the following model for HHC:

$$z = z_0 + Tu \quad (3.1)$$

where, for the four-bladed OH-6A:

'z' is a 6x1 vector of measured 4P (32 hertz) vibrations (g's).

'z₀' is a 6x1 vector of baseline 4P (32 hertz) vibrations (g's). The 'z' and 'z₀' vectors consist of the sine and cosine components of lateral, longitudinal, and vertical vibrations for a total size of six elements.

'T' is a 6x6 control response matrix that relates the swashplate movements to the vibration response of the helicopter (g's/inches).

'u' is a 6x1 vector of swashplate 4P (32 hertz) movement. It consists of the sine and cosine components

of lateral, longitudinal and collective swashplate excitation (inches).

This control law assumes a linear static transfer relationship (matrix ' T ') between command 4P swashplate motion and 4P fuselage vibrations. The equation states that the system 4P response (vector ' z ') consists of a baseline response (vector ' z_0 ') plus a response which is related to the 4P swashplate inputs (vector ' u ') by a transfer matrix (' T '). The transfer matrix ' T ' and the baseline vibrations ' z_0 ' depend on flight conditions such as forward speed.

Controllers are classified as being either "open-loop" or "closed-loop." There is no direct feedback of a measured response for open-loop controllers while there is a feedback of a measured response for closed-loop controllers.

Furthermore, two versions of the above control law exist. The "local model" assumes the control law is linear about the current control value. The local model is applicable even for nonlinear conditions, since the transfer matrix ' T ' is linearized about the current value and changes in swashplate excitation ' u ' are small. The 'global model' assumed the control law is linear for the entire range of control.

There are two methods for identifying the transfer matrix, ' T ,' and the baseline vibrations vector, ' z_0 .'

In the "off-line identification method," the characteristics of the ' T ' and ' z_0 ' are assumed invariant. This assumption is appropriate only to the global model. Generally, these matrices are generated as a result of a least squares estimate of wind tunnel or flight test data. These matrices are then used during later flights. The off-line controllers are further classified. In the "fixed-gain controller" the control law matrix remains unchanged for all flight conditions. The "scheduled-gain control" uses pre-determined libraries of matrices, based on "measured flight conditions" such as aircraft airspeed.

"On-line identification" continuously updates the characteristics of the matrix with time. The update time is normally in the order of once every rotor revolution. These controllers are also called "adaptive controllers" since the "control gains" vary with time. The on-line identification is applicable to both the global and local models. Many versions of this identification scheme are used. While some algorithms update the ' z_0 ' vector only, some update both ' z_0 ' and ' T '. Methods of updating the matrices include Kalman estimators and Least Mean Square adaptive inverse control. Finally, to limit the rate at which the control law changes many adaptive controllers add "caution" terms.

Considerable disagreement prevails over which controller is appropriate. Also, other control models exist, but are not tested. Controllers are the subject of much research, as shown in the next section.

D. PREVIOUS RESEARCH

The foregoing review of previous research efforts is by no means comprehensive, but it covers some important contributions. The review is categorized under three headings: theoretical analysis and numerical simulation, wind tunnel tests, and lastly, flight tests.

1. Theoretical Analysis and Numerical Simulation

HHC is modelled in most major helicopter comprehensive simulation codes. Wayne Johnson [Ref 3.1] has modelled HHC in CAMRAD (Comprehensive Analytical Model of Rotorcraft Aerodynamics and Dynamics). Karan Sangha [Ref 3.2] modelled HHC using McDonnell Douglas's RACAP (Rotor/Airframe Comprehensive Aeroelastic Program) in 1987. He concluded that HHC is independent of the modal character of the rotor. Kip Nygren [Ref 3.3] in 1989 investigated controllers using Kaman's DYSCO (Dynamic System Coupler Program). He showed that fixed-gain control can adequately reduce vibrations. However, the flight conditions are required to be within about 20 knots of the flight conditions used to calculate gains for the controller.

Daughaday in 1967 [Ref 3.4] conducted a study of HHC on a two-bladed teetering rotor. Early studies include that of Shaw in 1968 [Ref 3.5] and Balcerak and Erickson in 1969 [Ref 3.6]. McHugh and Shaw in 1978 [Ref 3.7] suggested one of the earliest HHC algorithms. In 1980, Yen [Ref 3.8] conducted a theoretical investigation of HHC for two and four bladed rotors. In 1981, Chopra and McCloud [Ref 3.9] investigated four different HHC feedback controllers. Johnson [Ref 3.10] provides a review of self-tuning regulators available before 1982 on both a theoretical and experimental basis. Gupta and Du Val [Ref 3.11] investigated an optimal control approach. Unlike other control algorithms, their approach was able to lock on the vibration gain and phase without resorting to harmonic analysis. However, they assumed the system to be linear-time-invariant, which is not always valid. In 1983, Molusis [Ref 3.12] conducted a simulation study which showed that nonlinearity is the main reason for the failure of HHC algorithms to fully minimize vibrations in his previous wind tunnel tests. Ham studied the application of individual blade control (IBC) to HHC [Ref 3.13]. Davis [Ref 3.14] in 1984 compared different controller configurations. He used a computer simulation that models the H-34 rotor mounted on the NASA Ames Rotor Test Apparatus and found no distinct advantage for any of the three controller types evaluated. Jacklin in 1985

[Ref 3.15] used a Least Mean Square algorithm to solve for the control transfer matrix. Hanagud et al. in 1986 [Ref 3.16] developed a technique to identify the transfer matrix in a HHC model. Robinson and Friedmann in 1989 [Ref 3.17] included the use of quasi-steady aerodynamics in their study of HHC. Hall and Wereley in 1989 [Ref 3.18] used classical control theory to study HHC. They concluded that real time adaptation of the control transfer matrix is not crucial for satisfactory performance of HHC.

2. Wind tunnel Investigations

There have been seven wind tunnel investigations of HHC reported to date. In 1974, McCloud and Kretz [Ref 3.19], and Sissingh and Donham [Ref 3.20] concluded that HHC would work with blade feathering of less than one degree. In 1980, Wood et al. [Ref 3.21] tested a 4 bladed articulated rotor model using open loop collective mode only. In 1980, Shaw and Alboin [Ref 3.22], first applied closed loop HHC experimentally. They achieved 90 % suppression of the three independent vibratory hub loads. Also in 1980, Hammond [Ref 3.23] attempted the first experimental application of adaptive identification. He used a Kalman filter estimation with stochastic (cautious) control to identify the transfer matrix required to minimize vibration. Molusis, Hammond, and Cline extended this work in 1981 to include fixed

gain controllers [Ref 3.24]. The scheduled gain controllers would saturate without achieving reductions in vibration levels. They concluded that the transfer matrix was both nonrepeatable and nonlinear. Shaw et al. [Ref 3.25] demonstrated in 1985 that a fixed gain control could provide 90 % reduction throughout a large flight envelope. In contrast, he found the control transfer matrix was linear and highly repeatable.

3. Flight Tests of HHC

There have been four known flight tests of HHC to date. Bell Helicopter attempted HHC in 1962 with a two bladed Bell UH-1A helicopter without success. Drees and Wernicke [Ref 3.26] reported that the vibration reductions were small. The first successful flight demonstration of HHC was in 1983 by Wood et al. [Ref 3.27] on a four bladed OH-6A. Wood and Powers in 1980 [Ref 3.28] presented a preliminary design study for this aircraft. Straub and Byrns in 1986 [Ref 3.29] fully documented this flight test. Walsh [Ref 3.30] and Miao et al. [Ref 3.31] reported on the open loop HHC flight demonstration on a four bladed S-76A helicopter during 1985. They achieved significant vibration reductions at forward speeds up to 150 knots. Polychroniadis and Achache [Ref 3.32] reported the open loop and closed loop HHC flight tests on a three bladed SA 349 Gazelle helicopter conducted in France in 1985. They also

achieved 80 % reductions in the cabin vibrations at 150 knots.

E. THE MCDONNELL DOUGLAS/NASA/ARMY HHC TEST PROGRAM

1. Scope of Tests

This section briefly describes the OH-6A flight tests. The flight test program consisted of three distinct phases covering the period of 1980 to 1984. First, the flight test OH-6A underwent major changes to include the HHC system. Then, approximately 15 flight hours were devoted to open loop testing. In open loop testing, the phase and amplitude of the HHC blade feathering was set manually. Over 26 flight hours were devoted to testing of the closed loop system. In closed loop operation, a microprocessor controlled the phase and amplitude. Figure 3-1 presents a summary of the results, the flight conditions, and modes tested. The figure presents the 4P pilot seat vertical acceleration obtained by Fourier analysis using the McDonnell Douglas HARMONS program. Tests include all three open loop (manual) modes and eight closed loop (computer controlled) modes using different controller softwares. The figure depicts two of the best closed loop modes. The airspeed ranged from hover and 40 to 100 knots, in 10 knot increments. In open loop testing, for each airspeed, the amplitude of excitation was fixed, and the phase was varied in

increments of 30 degrees over a total range of 0 to 360 degrees. Each phase sweep for a given airspeed required an average of 15 minutes. Figure 3-1 presents data at the best phase setting obtained from open loop testing.

2. Description of Test Aircraft

The OH-6A used for HHC testing was a one of a kind aircraft. A previous flight test program modified the OH-6A to include a 1,500 psi boost system for its primary controls. This irreversible control system prevented feedback from the HHC actuators to the pilot's controls. Three electro-hydraulic actuators replaced existing links in the primary control system. They were located between the mixer and the stationary swashplate just below the rotor head. The actuators were capable of changing the blade feathering angle by 2 degrees, about 11 % of the total range available. The three accelerometers mounted under the pilot's seat sensed the vibrations. The analog acceleration signals were sent to an electronic control unit (ECU) for conversion to digital signals and then transferred to the airborne digital computer. A Sperry Flight Systems multiplex remote terminal unit Type 3A served as the on-board computer and determined the required blade feathering. The computer sent its digital commands back to the ECU, which in turn converted them to analog signals. These analog signals drove the three actuators that tilted the

stationary swashplate. The resulting swashplate movement caused the blades to change pitch. The high frequency feathering of the rotor blades generated aerodynamic forces. These forces were transmitted through the rotor blades, rotor hub and the fuselage to reduce the vibration sensed under the pilot's seat. Figure 3-2 presents a sketch of the HHC system installed on the OH-6A test aircraft.

The Airborne Data Acquisition System measured and recorded the flight test data. Strain gages placed on one rotor blade of the main rotor measured flapwise bending, chordwise bending, and torsion moments. An LVDT measured HHC actuator positions while potentiometers measured blade feathering, flapping and lead-lag angles. There were three groups of triaxial accelerometers that measured fuselage accelerations. There were strain gages that measured tail boom and main rotor mast bending moments. The pitch link loads, the main rotor RPM, the main rotor shaft torque, the aircraft airspeed and the main rotor azimuth position were all sensed. Appendix B presents a list of measurements made available from these flights to the Naval Postgraduate School.

3. Method of Tests

The pilot stabilized the aircraft at the flight test airspeed for at least 20 seconds, while the flight test engineer operated the HHC system. In open loop

testing, he turned the system on and off, selected mode, amplitude and phase of excitation. In closed loop testing, he turned the system on and off and selected gains on the control matrices. The flight test engineer turned on data recording for about ten seconds during the most stable conditions. After the flight, five second time slices of the most stabilized portion of the data were selected. These time slices constitute the data used in the flight tests reports.

4. Results

The principal objective of the flight test was to minimize 4P vibration only, rather than to counter all vibrations inherent in the helicopter. Figure 3-3 presents the open loop test results for lateral swashplate excitation equivalent to + 0.33 degree of blade angle of attack change at airspeeds from 60 to 100 knots. The figure depicts the 4P (32 hertz only) accelerations in g's as measured vertically and laterally by accelerometers mounted under the pilot's seat. These values were obtained by Fourier analysis by a HP 5423 spectral analyzer. Notice that there exists up to 100 percent difference between these estimates and those in Figure 3-1. The estimates in Figure 3-1 and Figure 3-3 were computed using different methods. The frequency domain chapter discusses the difficulties in obtaining accurate Fourier estimates.

The input phase refers to the phase of the swashplate tilting in relation to the main rotor position. In the lateral mode, zero degree controller phase corresponds to tilting the swashplate to the port when the four rotor blades were at 0, 90, 180 and 270 degrees rotor azimuth, respectively. 180 degrees controller phase corresponds to tilting the swashplate to starboard when the four rotor blades were at 45, 135, 225, and 315 degrees rotor azimuth, respectively. Notice 360 degrees of input phase to the controller corresponds only to 90 degrees of rotation of the rotor. Also, the data for each of these graphs in Figure 3-3 come from 14 different flight test points. A typical series of tests at each airspeed took 10 to 15 minutes to record.

From Figure 3-3, it is apparent that for certain controller phases, HHC has the ability to make the helicopter vibrate more. For all the airspeeds tested, maximum vibration occurs at 90 degree controller phase and minimum vibration at 300 degree manual controller phase. By using only the lateral excitation of the swashplate, the 4P vertical vibration are reduced from 0.25 g to 0.04 g (at 60 knots). Similarly, the reductions for 4P lateral vibration are from 0.12 g to 0.02g (at 60 knots).

Wood et al. [Ref 3.28] and Straub and Byrns [Ref 3.29] summarize other results from this flight test.

They conclude that the 4P vibrations under the pilot's seat were significantly reduced with the HHC system. The system did not adversely affect blade loads or helicopter performance.

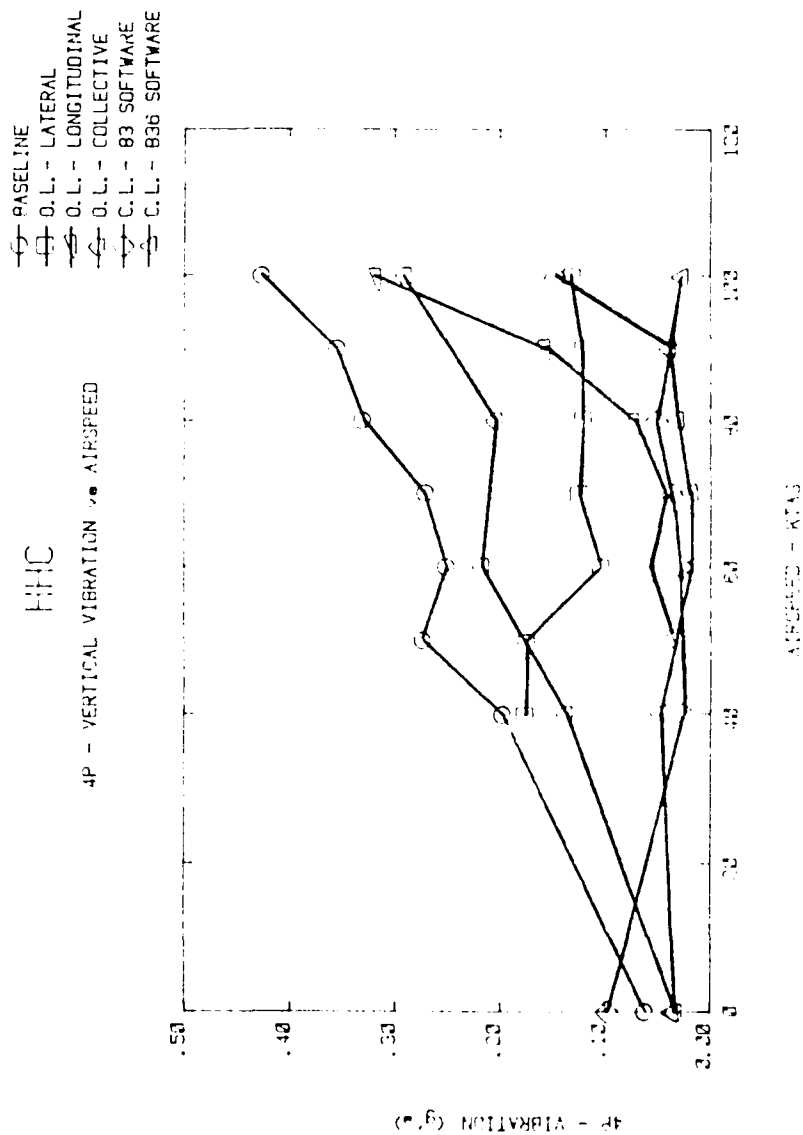


Figure 3-1. The McDonnell Douglas's HHC OH-6A's Scope of Flight Tests. This graph presents the best 4P vibration reduction achieved using HHC. Tested were all three open loop (manual controlled) modes and two closed loop (computer controlled) modes using different controller software. The abbreviations "O.L." mean Open Loop and "C.L." mean Closed Loop [drawn by McDonnell Douglas Helicopter Company, reprinted with permission].

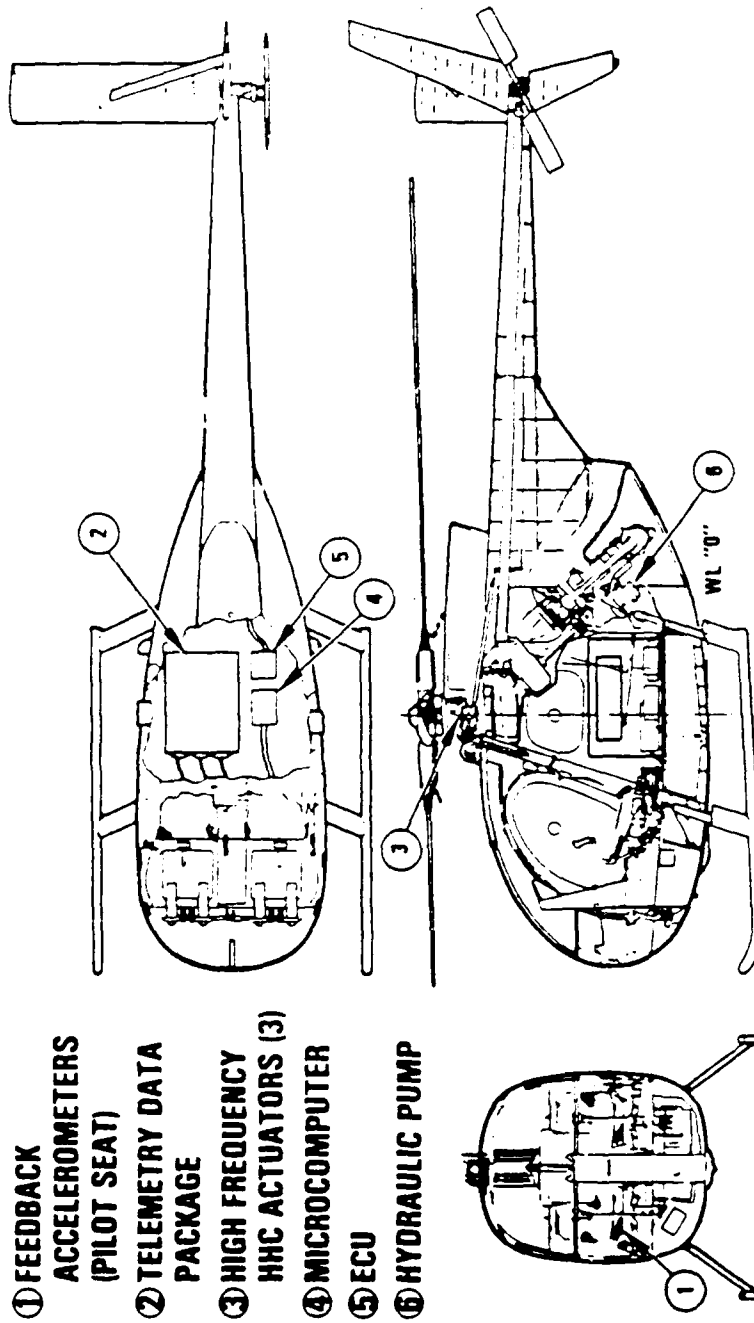


Figure 3-2. Sketch of the HHC system. [from Wood et al. (1985), reprinted with permission of author].

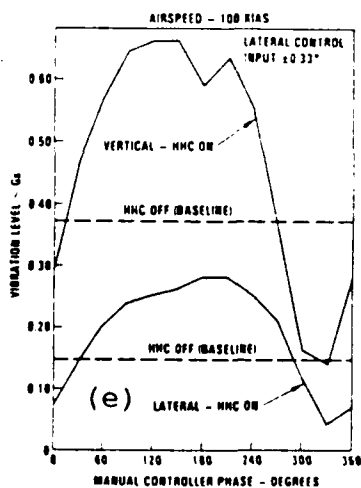
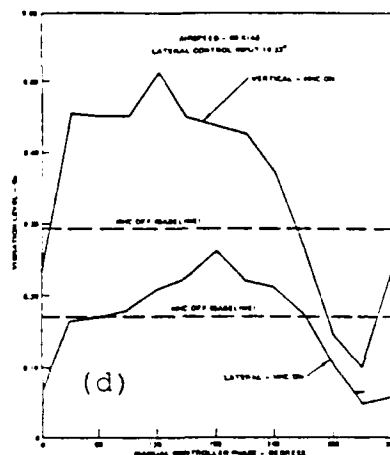
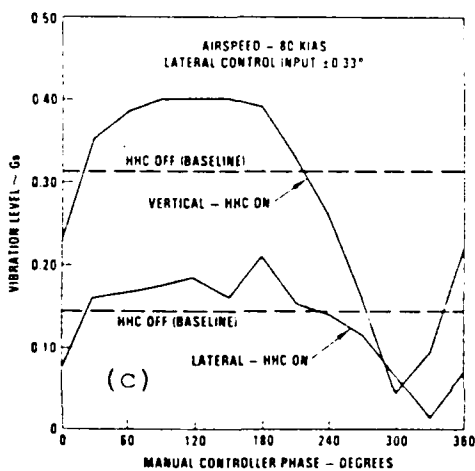
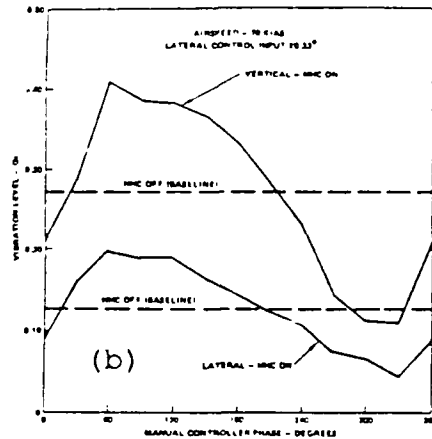
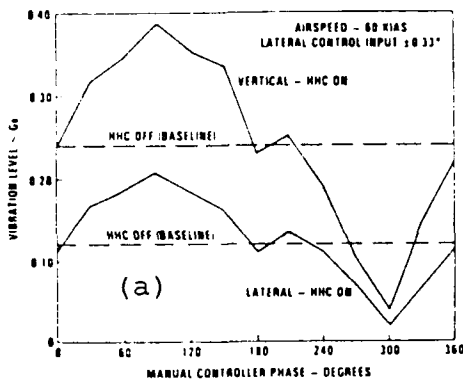


Figure 3-3. 4P Vibration at the Pilot's Seat. Variation of 4P vibration with manual controller's input phase. (a) 60 knots. (b) 70 knots. (c) 80 knots. (d) 90 knots. (e) 100 knots [from Wood et al. (1985), reprinted with permission of author].

IV. TIME DOMAIN ANALYSIS

A. PURPOSE

State-of-the-art analysis of flight test data includes the use of both time and frequency domain methods. This chapter outlines the basics of measuring data in the time domain. The next chapter describes the analysis in the frequency domain. The overview includes some of the common measurements in the time domain. An excellent source for the time domain analysis is Otnes and Enochson [Ref 4.1].

B. DIGITAL SIGNALS

Measurement of any quantity is initially as an analog signal. In an analog signal, the amplitude of the signal can vary continuously with time. At a given instant, the signal can assume any value within a relatively wide range of values. Translation of analog signals to digital signals occurs in a flight test for transmission, storage and subsequent analysis. This analog-to-digital conversion process introduces errors into the data.

Generally, there are three steps to convert an analog signal to a digital signal; namely, sampling, quantizing and encoding. Figure 4-1 illustrates the sampling process. Sampling a continuous analog signal in time

forms a series of values. Consider an analog signal that has a frequency spectrum covering a band from zero to an upper frequency (known as the "Nyquist frequency"). It is possible to transmit all the information by sampling the signal, at regular intervals, at twice the rate of the Nyquist frequency. Sampling converts a continuous signal to digitized signal in time.

On the OH-6A, the data sampling rate was 1230 samples per second or loosely said, 1230 Hertz. This implies that the upper limit in the frequency resolution, or, the Nyquist frequency, is 615 Hertz.

The second step, quantizing, samples the signal in terms of amplitude. Figure 4-2 illustrates this process. Quantizing divides the entire amplitude range into a number of discrete levels, known as "quantum levels." Comparing the amplitude of the analog signal with the quantum levels results in a quantum level that is nearest to the amplitude of the analog signal. That is, the quantum level approximates the actual amplitude. Hence the quantizing process introduces a quantization error. The maximum error is one half of the quantum step size, resulting in THE major source of error in measurement of flight test data.

In the flight test data of OH-6A, the number of quantum levels was 1024. This results in a the maximum error of about 0.05 percent. In practice, the

quantization error is found to be more than this. The limits of the full scale range are rarely set about the correct interval. For example, Figure 4-3 presents five seconds of flight test data for the rotor rpm of the OH-6A. Quantization error is readily apparent. In this case, the full range of acceptable values for rpm were from 14 percent to 206 percent. However, once airborne, the rotor rpm stays within 1 to 2 percent of its normal 100 percent rpm. The quantization error is large in this case because the range of acceptable input values is large, while the fluctuations about an average point is small. This example reflects one of the worst quantization errors for the OH-6A.

The final step, encoding, is the translation of the quantum levels to fewer levels, but using several discrete elements. In other words, translate the 1024 quantum levels to only 2 quantum levels (binary) by using several bits. The OH-6A flight test instrumentation system used a 10 bit binary word, hence 1024 quantum levels can be represented (2 raised to the 10th power).

C. MEASUREMENTS IN THE TIME DOMAIN

Once the data is obtained as a digitized time series, different "measures" may be computed. 'N' represent the number of digitized values and 'x' represent the

digitized amplitudes of a signal. They form a data record. The mean ' x_a ' is then defined as:

$$X_a = \frac{1}{N} \sum_{i=1}^N X_i \quad (4.1)$$

The energy content of the signal in the time domain is given by:

$$\text{ENERGY} = \frac{1}{(N-1)} \sum_{i=1}^N (x_i - x_a)^2 \quad (4.2)$$

This is the well known formula for variance or the first moment of the mean. The vibratory energy of a signal is equal to the variance in the time domain.

The square root of the variance is the standard deviation, while the second moment of the mean yields skewness and the third moment of the mean is referred to as kurtosis. Skewness is a nondimensional number which characterizes the degree of asymmetry of the data around its mean. Kurtosis is also a nondimensional quantity that measures the relative peakedness or flatness of the distribution of the data relative to a normal distribution.

D. ERGODIC AND STATIONARY DATA

A major assumption made in Fourier Analysis is that the measured data is ergodic and stationary.

Data is stationary if the mean and variance are independent of time. In other words, the values for the mean and the variance stay constant for all data segment sizes. For example, Figure 4-4(a) presents a signal with a stationary mean, variance and frequency. Figure 4-4(b) presents a signal with stationary mean but with a non-stationary variance and frequency. Figure 4-4(c) presents a signal with non-stationary mean but stationary variance and frequency.

Ergodicity is the property that requires the short time averages to be equal to averages over the entire process. In order to test whether a signal is stationary and/or ergodic, a long record is examined by partitioning it into a number of sections of equal length. If the mean value and variance obtained from each partitioned section are the same as those calculated from the entire record, the signal is considered as ergodic. Note that in figure 4-4, only part (a) is ergodic.

E. SUMMARY

Quantization error is normally the major source of error introduced by a practical flight test instrumentation system. Also, the Nyquist frequency limits the upper frequency of the input signal. Major assumptions are made that the input data is ergodic and

stationary, although the real flight test data is seldom ergodic and stationary.

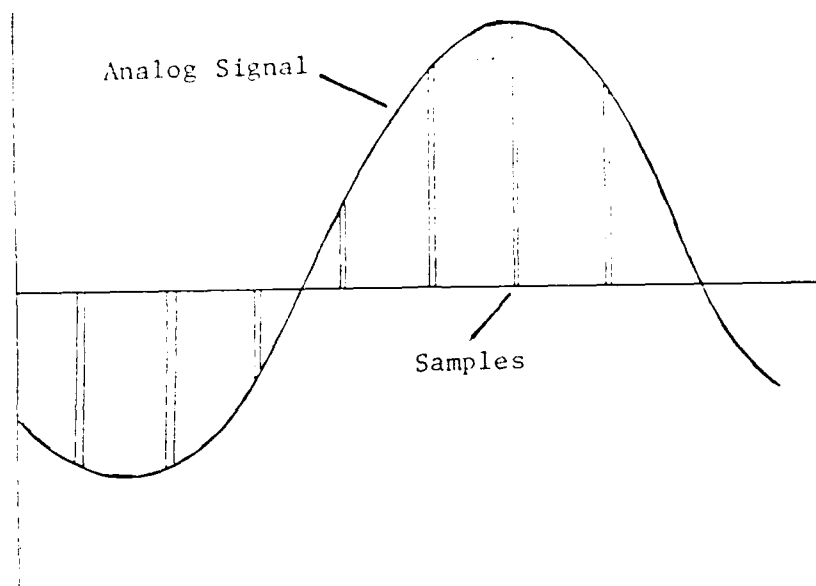


Figure 4-1. Sampling Process.

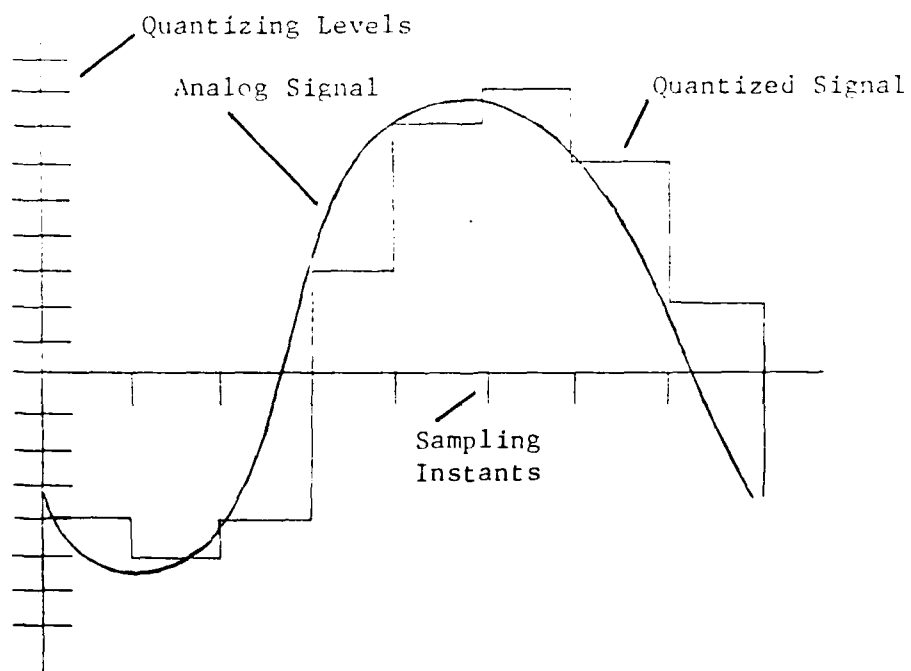


Figure 4-2. Quantizing.

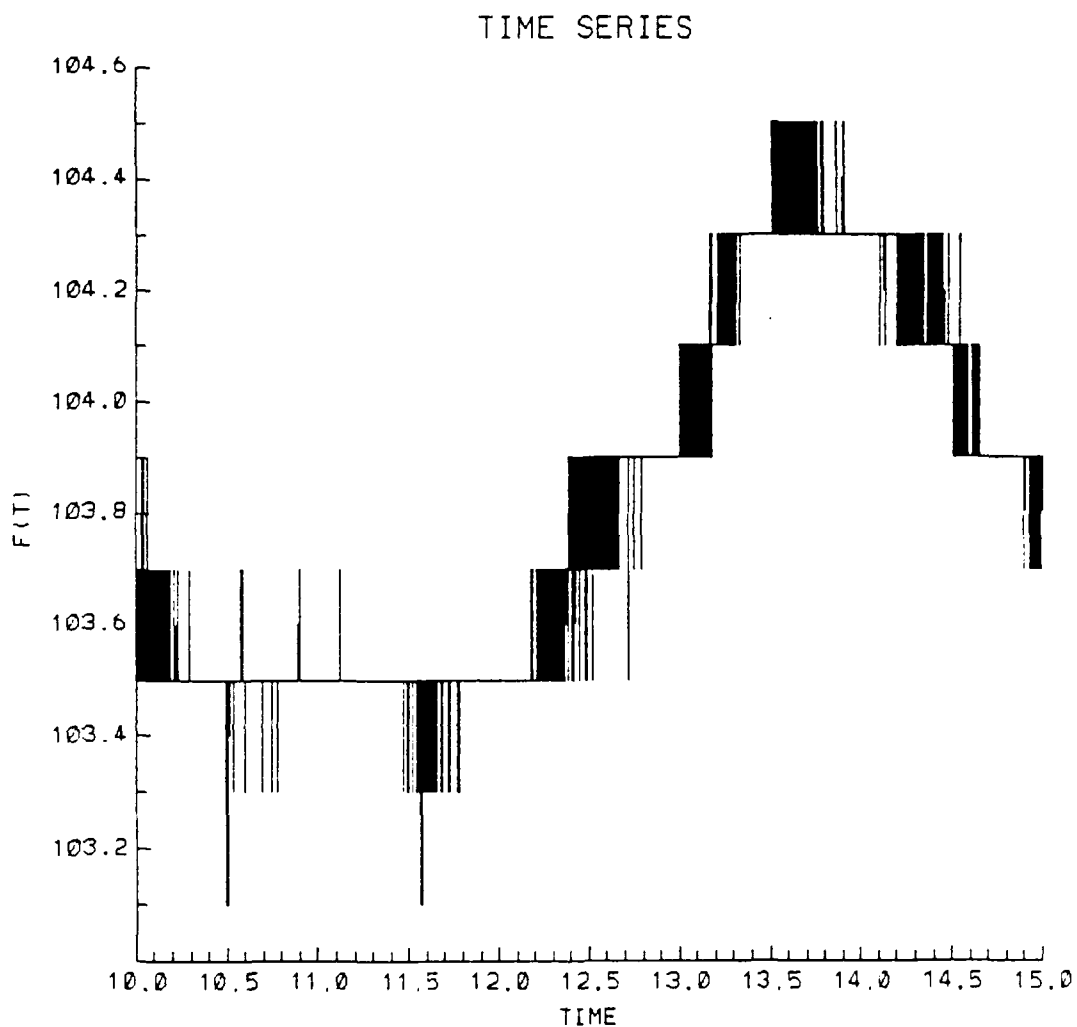


Figure 4-3. Main Rotor Rpm for the OH-6A. Sample taken during smooth steady level flight with HHC system off.

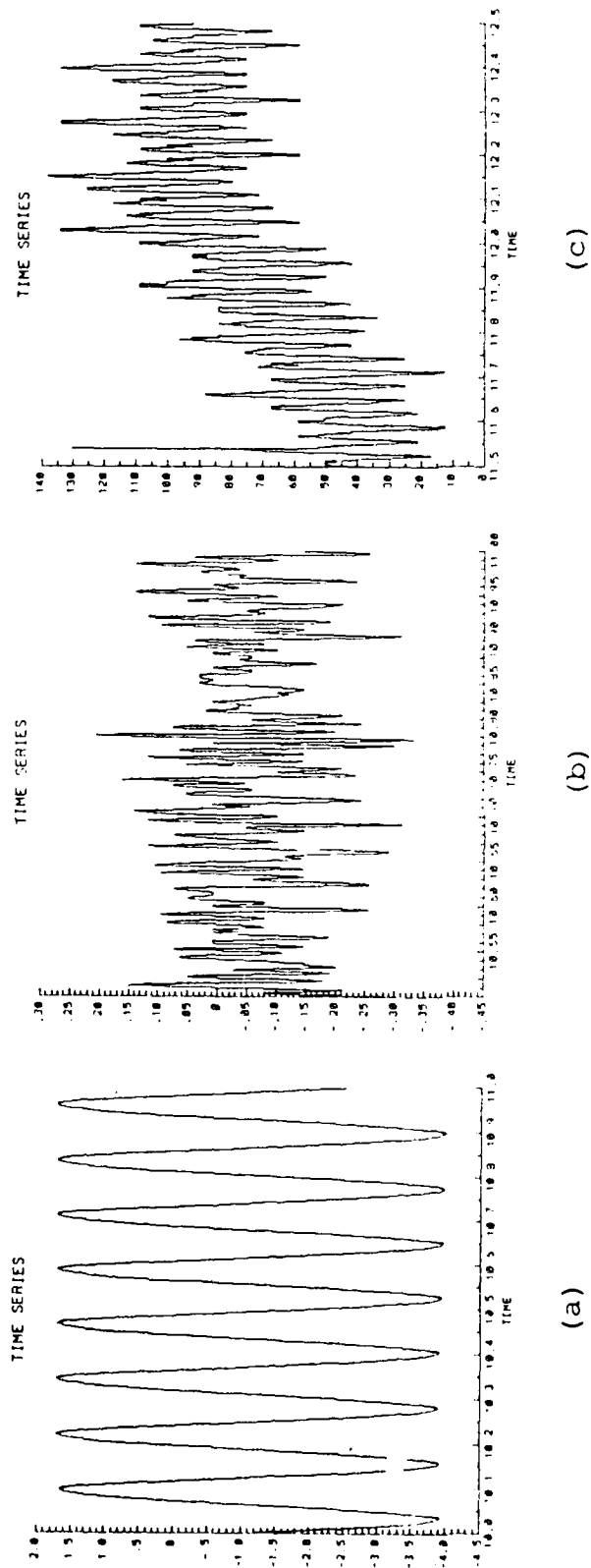


Figure 4-4. Ergodic and Stationary Data. Some examples from the OH-6A. (a) Stationary mean, variance, and frequency for rotor blade feathering angle. (b) Stationary mean but non-stationary variance and frequency for longitudinal acceleration. (c) Non-stationary mean but stationary variance and frequency in longitudinal load link load.

V. ANALYSIS IN THE FREQUENCY DOMAIN

A. PURPOSE

An alternate method to analyze flight test data is in the frequency domain. The aim of this section is to introduce the fundamental ideas of Fourier analysis. Discussion includes limitations of these transforms. A good source for further information may be found in [Ref 5.1 to 5.4].

B. FOURIER TRANSFORMS

Our ear converts sound waves traveling through time into a spectrum of frequencies, a description of the sound as a series of volumes at distinct pitches. Similarly, Fourier analysis breaks down a function in time into harmonic components that have varying frequencies, amplitudes and phases.

Any periodic waveform is equivalent to the sum of a number of sinusoids. Consider a signal which consists of two sinusoids, a high and low frequency sine curve as shown in figure 5-1(a). Looking down the frequency axis gives part (b). This is the time domain view of the waveform, obtained by adding the sinusoids at each moment in time. Looking down the time axis gives part (c), the signal as observed in the frequency domain. The switch

from the time to the frequency domain produces no new information. The same information exists, but the presentation is different.

The Fourier transform converts a time domain function, 'x(t)', into the frequency domain function, 'S(f)'. The complex form of this transform is:

$$S(\omega) = \int_{-\infty}^{+\infty} x(t) e^{-j\omega t} dt \quad (5.1)$$

'S(f)' is known as the Fourier transform of 'x(t)'. It is in general complex, and contains amplitude and phase information for all frequencies which make up 'x(t)'.

Figure 5-1(c) represents the amplitude spectrum of a signal. However, full representation of a signal in the frequency domain requires two numbers at each frequency. For instance, these can be the amplitude and phase. The signal may also be represented as a single complex number or by a sum of weighted sines and cosines at each frequency. A signal in the frequency domain requires two plots for full representation. These plots may either be an amplitude and phase plot versus frequency, a real and complex plot versus frequency or a cosine and sine plot versus frequency. However a signal in the time domain requires only one plot of amplitude versus time for full representation.

A commonly used representation is the "Power Spectral Density" or PSD graph. The vertical axis gives the square of the amplitude and the horizontal axis indicates frequency. For example, an accelerometer provides measured accelerations in the units of "g's". On a PSD, the plot is "g's squared" versus "frequency." Therefore, the units of a PSD are really in terms of energy not power.

C. PARSEVAL'S THEOREM

"Parseval's theorem" states that the total power in a signal is the same, whether computed in the time or the frequency domain. The sum of a PSD from zero to the Nyquist frequency gives the total energy in the frequency domain. As energy is invariant, the energy computed in the time domain (variance) is the same as computed in the frequency domain.

D. PHASE SPECTRUMS

Use of phase spectrums is not as common as the use of PSD. In Figure 5-2, the upper plot gives the PSD of the vertical acceleration under the pilot's right seat. The lower plot is the phase spectrum of the same acceleration. Note that the phase spectrum gives equal weight to reporting the phase of both the low and high amplitude signals. It is difficult to determine the

phase at a particular frequency. Generally, not much attention is given to phase determination in spectral analysis.

A phase is measured or provided relative to a reference quantity. In figure 5-2(b), the phase is shown relative to the start of the data record. A different data record start produces a completely different phase spectrum. A possible solution is to fix the start with respect to some quantity. For example, main rotor azimuth position is a common adopted choice. In figure 5-2(b), the start of the data record is at 0 degree rotor blade azimuth position, and the plot may be called as a relative phase plot.

E. DIFFERENT METHODS FOR PSD's

There are many methods of obtaining the PSD of a signal. Figure 5-3 [Ref 5.4] summarizes many spectral estimators. Part (h) is the true PSD. Observe the large differences between each of the estimates. The visual comparison of spectral estimates can often be misleading. The sharpest of the peaks of a spectral estimate is not an indication of the resolution of a spectral estimate. The classical PSD estimation is the periodogram method, part (i). Other methods require a prior knowledge of the PSD curve to provide a model to the estimator. The periodogram method is superior for HHC applications,

since it requires no model. We will limit our discussion to the periodogram method, although, all of the limitations discussed below apply equally to other methods.

F. LIMITATIONS AND RESTRICTIONS

Digitizing the data leads to some limitations and restrictions. The discrete data points used in obtaining a Fourier transform represent a continuous time signal. If data acquisition time or period is 'T,' the number of data points is 'N,' and the sampling rate 'dr,' then

$$N = T \text{ dr} \quad (5.2)$$

For example, five seconds (T) of data at 1230 data samples per second (dr) was made available in HHC flight test. This data record yields a total of 6150 data points (N).

Many important restrictions also occur because of the finite record length of the data. For practical reasons, flight tests restrict the period, 'T,' to about 5 seconds. Some restrictions are summarized below.

1. Periodic, Stationary and Ergodic Data

The first major restriction on the use of Fourier transform is that the time series must be periodic. Also, the data must also be stationary and ergodic.

These restrictions may be overcome by allowing the period, 'T,' of the signal to approach infinity, which is impossible in flight test.

2. The Fast Fourier Transform

The most common way to obtain the periodogram PSD is the Fast Fourier Transform (FFT). The FFT is an algorithm for obtaining efficiently the fourier transform of a time series. The algorithm operates on an array of N complex data points in the time domain. It produces an array of N/2 complex data points in the frequency domain. An important restriction in using this algorithm is that the number of data points in the time domain must be a power of 2 (for example, 512, 1024, 2048, etc.). Normally the time domain data is real, so that the imaginary part of each input data point will be zero.

The PSD amplitude (energy) is the sum of the squares of the real and imaginary parts of the FFT's complex output. Fourier phase is the arc tangent of the imaginary part divided by the real part.

3. Nyquist Criterion and Aliasing

A limitation exists on the frequency range of the PSD and this imposes an important restriction in practical applications. The frequency range of the Fourier transform is from zero to the Nyquist frequency. The Nyquist frequency is equal to one half the sampling

rate. For the HHC sampling rate of 1230 hertz, the upper limit or Nyquist frequency is 615 hertz.

Note that this Nyquist frequency is independent of the number of samples in the record. The frequency resolution may be increased by increasing the number of samples (by taking longer periods of data). However, this does not increase the maximum frequency in the spectrum. In other words:

$$\Delta f = \frac{1}{T} \quad (5.3)$$

For example, a 5 seconds of flight test data results in resolution of 1/5 Hertz. This implies that the minimum difference between adjacent frequencies is 1/5 Hertz. This is yet another restriction in obtaining an accurate estimate of the PSD.

If sampling is slower than twice the frequency of the input signal, then a false low frequency appears in the PSD. This phenomenon is called as "aliasing." Shannon's Sampling theorem states that a sampled time signal must not contain components at frequencies above half the sampling rate (the Nyquist frequency or "Nyquist criterion"). If the frequency of the input signal is greater than half the sample rate, a spurious signal will result. As an example, for a 615 hertz Nyquist frequency, a true signal containing a component at 700

Hertz would show up on a PSD at 530 Hertz. The problem of aliasing is prevented by adding a low-pass or "antialias" filter before the sampler to limit the input frequency range.

Shannon's sampling theorem does not imply that the sampling rate must be more than twice the highest frequency of interest, but that filtering the high frequency components out must occur before sampling the signal.

4. Leakage and Windowing of Data

Another important problem is due to leakage. This problem is best illustrated by an example. Consider a sine curve as shown in Figure 5-4. In part (a) is the sine curve. In part (b), recorded is an integral number of cycles of this sine curve over a duration, 'T.' As stated earlier, an implicit assumption is the data record containing the sampled block repeats throughout time. In part (c), the assumed signal exactly matches the input. Part (d) presents the PSD obtained in such a case and it contains a single spike as expected.

Now consider Figure 5-5, again the case of a continuous sine curve. The failure to select an integral number of cycles of the sine curve results in the highly distorted waveform shown in part (c). Part (d) presents the PSD in this case. The smearing of energy throughout the frequency domain is called "leakage" and results in

distortion of the PSD. Leakage occurs because of the finite length of time, 'T,' of the data record.

A solution to leakage is to window the data as illustrated in Figure 5-6. Note that windowing the data TAMPERS with the data. Figure 5-6(f) shows that the PSD is closer to the correct single line, but not exactly it. Typical window functions include Parzen, Hanning, Hamming, and Welch. The difference between these functions lie in subtle trade-offs among various figures of merit used to describe the narrowness or peakedness of the PSD. There exists effectively no difference between any of these window functions for practical spectral analysis [Ref 5.1].

6. Accuracy of PSD's

The accuracy of PSD estimates do not increase with the number of sampled data points, 'N.' The variance of the PSD estimate at a selected frequency is always equal to the square of its expected value at that frequency. In other words, the standard deviation is always 100 percent of the value of the PSD estimate.

Let us consider the effect of increasing 'N.' Using a longer duration of data at the same sampling rate leaves the Nyquist critical frequency unchanged, but gives finer frequency resolution (more frequency bins). Alternatively, sampling the same length of data with a finer sampling interval leaves the frequency resolution

unchanged, but the Nyquist frequency range now extends up to a higher frequency. In neither case do the additional samples reduce the variance of estimated PSD at any particular frequency.

There are methods to increase the accuracy of a PSD. One simple method is to compute a PSD estimate with a finer discrete frequency spacing than desired. A smooth estimate is obtained at the mid-frequency by summing the PSD estimates at adjacent discrete frequencies. The variance of the estimated sum will be smaller than the individual estimates. This procedure trades frequency resolution for greater accuracy in the estimate of the amplitude of the PSD.

G. SUMMARY

This chapter summarized some of the many facets of frequency domain analysis. The sampled data is assumed to be stationary, ergodic and periodic. Many important restrictions are due to digitization of data with finite record length. The peak value at a given frequency gives an inaccurate estimate of the PSD. There are many methods to calculate PSD, each giving a different estimate. Also, any estimate may be obtained by "tampering" the data appropriately.

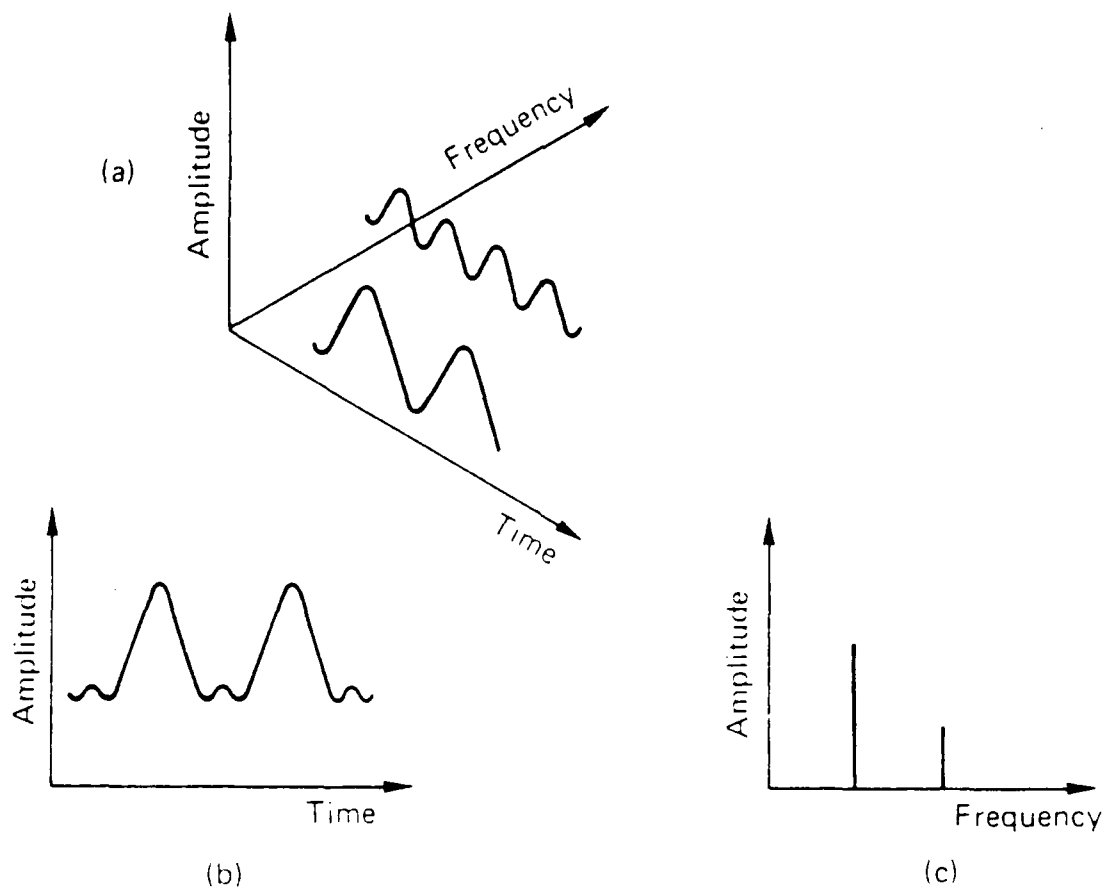


Figure 5-1. The frequency domain. (a) Time and frequency domains represented in three dimensions. (b) Time domain view. (c) Frequency domain view. [from Turner, J. D. (1983) with permission of Springer-Verlag, copyright 1988].

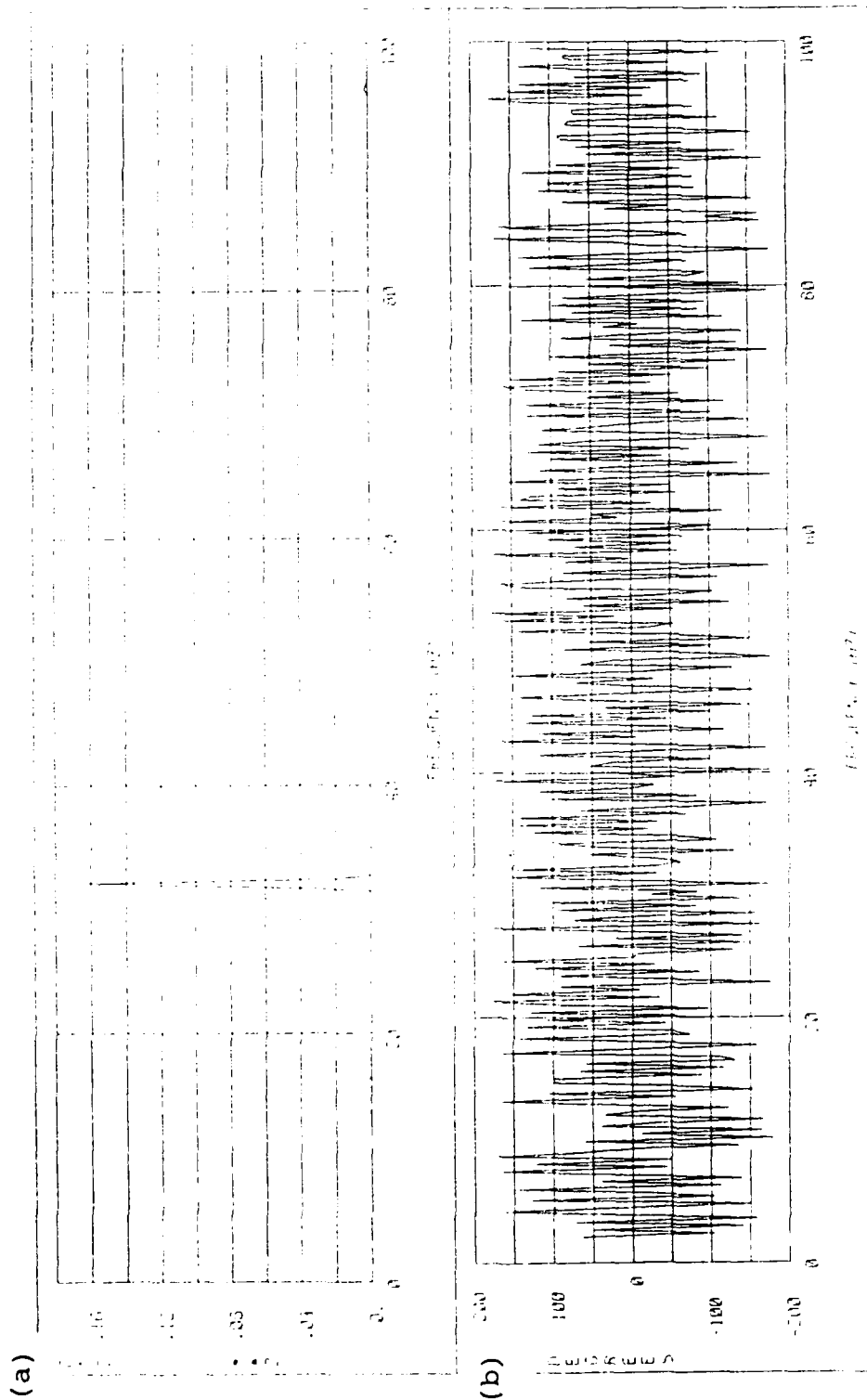


Figure 5-2. Power and Phase Spectrums. (a) Power Density Spectrum. (b) Phase Spectrum. [produced by McDonnell Douglas Helicopter Company, reprinted with permission].

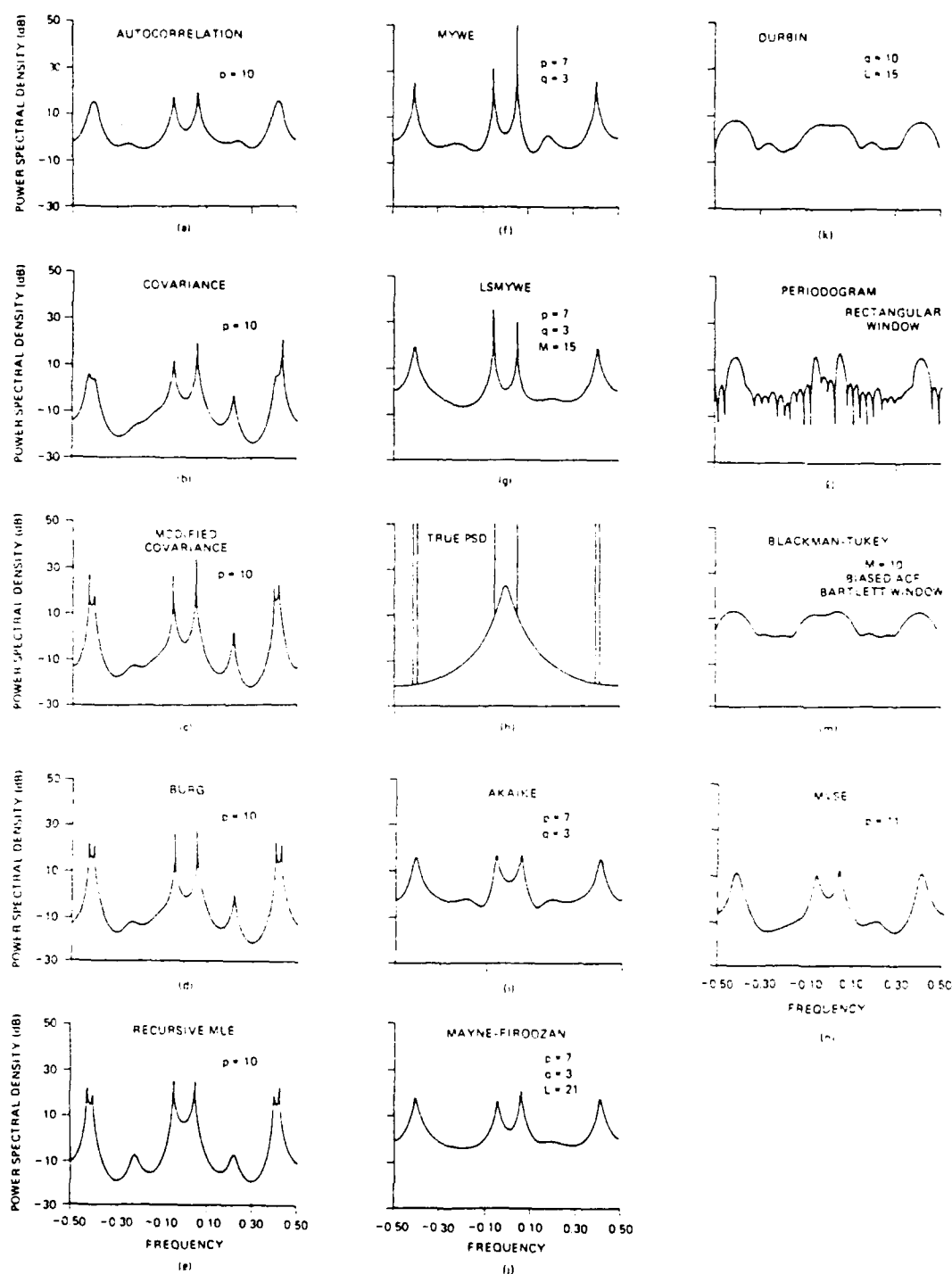


Figure 5-3. Comparison of Power Density Spectrum Estimators. (a) Autocorrelation. (b) Covariance. (c) Modified covariance. (d) Burg. (e) Recursive MLE. (f) MYWE. (g) LSMYWE. (h) True PSD. (i) Akaike. (j) Mayne-Firoozan. (k) Durbin. (l) Periodogram. (m) Blackman-Tukey. (n) MVSE. [from Kay, S. M. (1988) with permission of Prentice-Hall, copyright 1988].

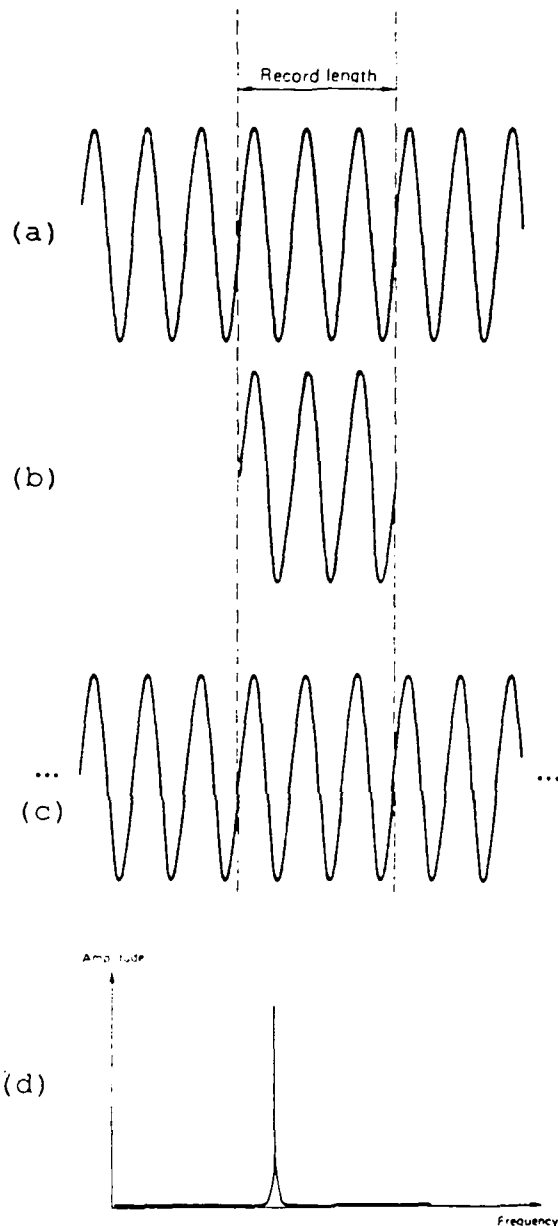


Figure 5-4. Periodic Signal. When the signal is periodic within the truncated time record, the assumed repeats match the input. (a) The signal. (b) Truncated record. (c) Assumed repeats exactly match the input signal. (d) The spectrum resulting from (c). [from Turner, J. D. (1988) with permission of Springer-Verlag, copyright 1988].

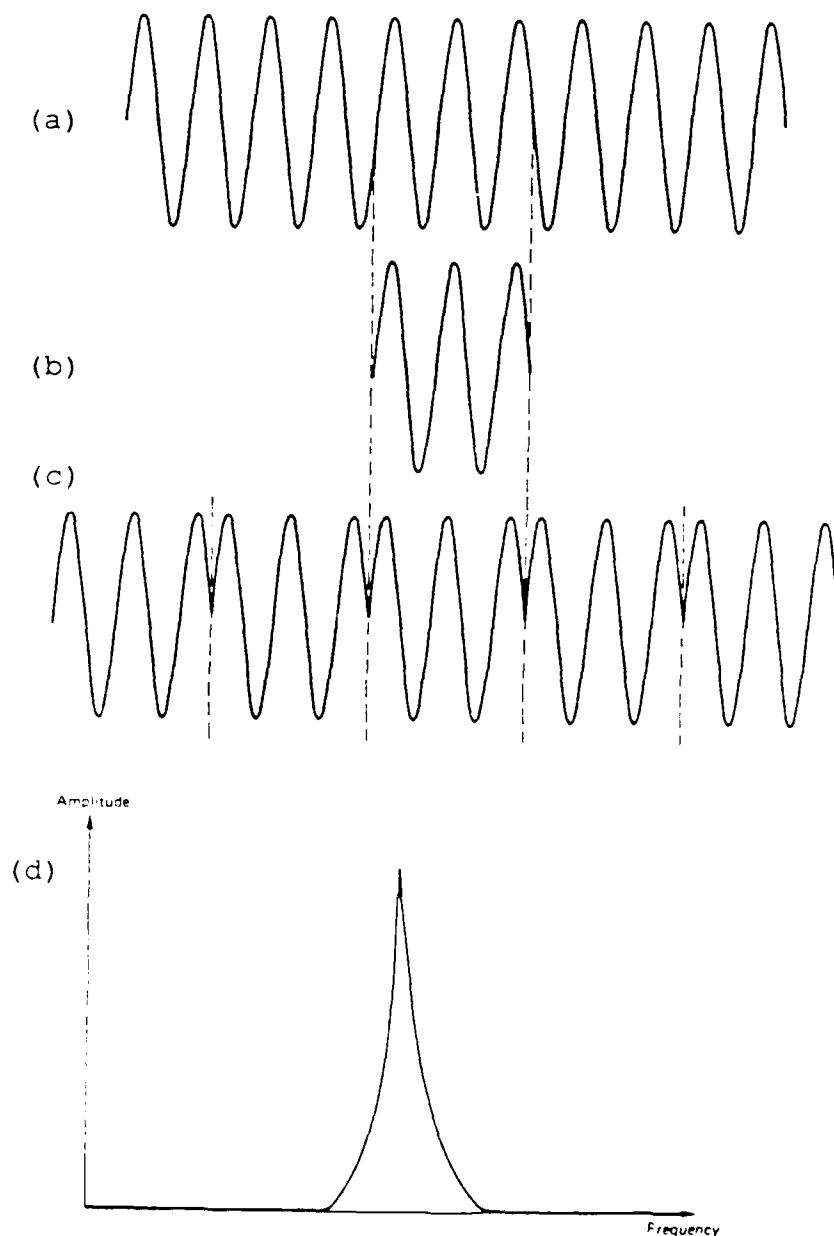


Figure 5-5. Not Periodic Signal. Input signal not periodic within time record, and resulting assumed input is distorted. (a) The signal. (b) Truncated record. (c) Assumed repeats do not match the input signal. (d) Distorted spectrum resulting from (c). [from Turner, J. D. (1988) with permission of Springer-Verlag, copyright 1988].

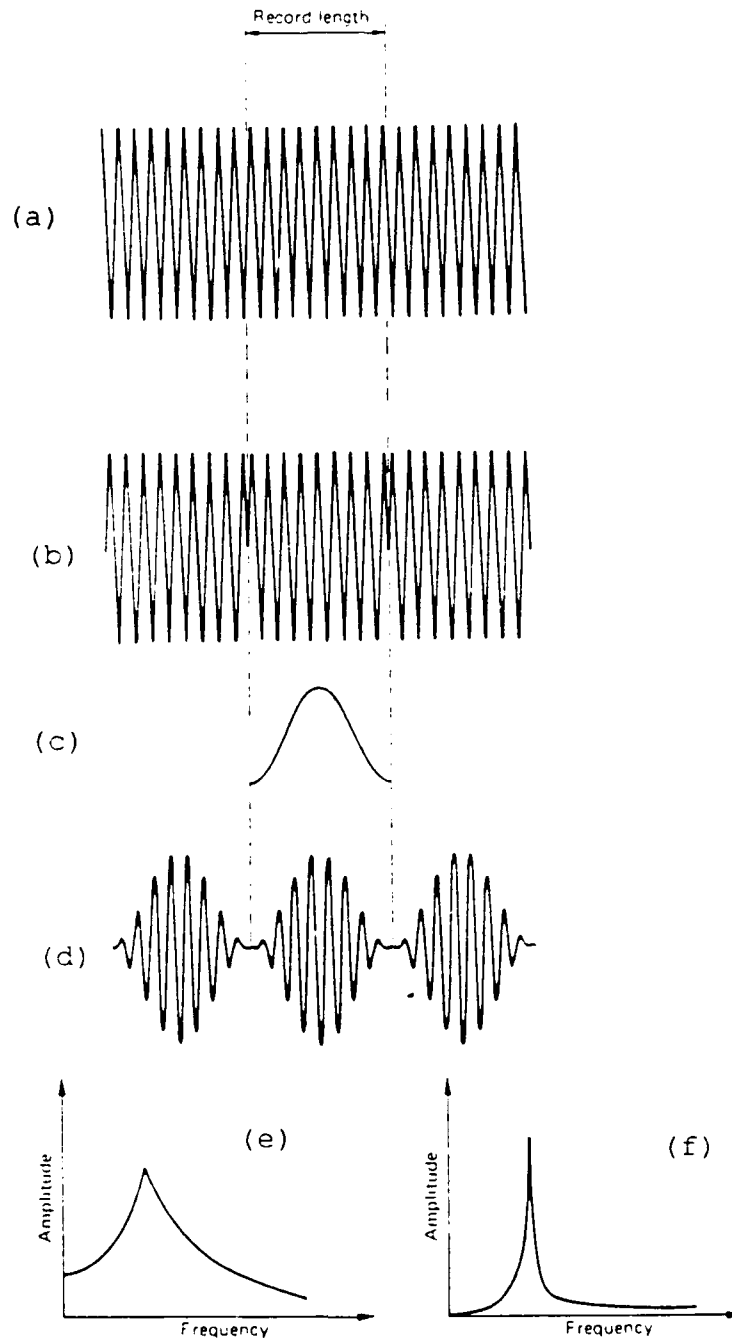


Figure 5-6. Windowing. The effect of windowing a continuous signal. (a) The signal. (b) Assumed repeat. (c) Window function. (d) Assumed repeat, windowed data. (e) Spectra obtained from a sine curve not periodic within the record without the window. (f) Spectra with Hanning window function. [from Turner, J. D. (1988) with permission of Springer-Verlag, copyright 1988].

VI. GEOMETRIC AND TOPOLOGICAL METHODS OF CHAOS

A. PURPOSE AND INTRODUCTION

The previous two chapters discussed the state-of-the-art in the flight test data analysis. The purpose of this chapter is to discuss some aspects of the geometric and topological methods of chaos. Chaos is present only in some nonlinear dynamical systems.

A non-linear dynamical system may be classified as deterministic or non-deterministic. A deterministic system is described by a finite number of equation(s) with known parameters and initial conditions. The response of such a system is predictable. A periodic system is a type of a deterministic system whose motion can be described by harmonic functions.

A deterministic system may be sensitive to small changes in initial conditions. Such a system is defined as chaotic. Chaotic motion may appear random.

A non-deterministic system can be described only in probabilistic terms. Such a system possesses equations those terms vary randomly. In a purely random system, amplitude is independent of frequency. The Fourier power spectrum appears continuous. [Ref 6.1]

Differentiating between chaotic and random responses from an experimental observation is difficult. In

general, the following approaches may lead to evidence of chaos in nonlinear dynamical systems [Ref 6.1].

Make an observation of the time history of the signal.

Compute the Fourier spectrum of signal.

Construct and observe the phase plane and phase space portrait.

Construct the Poincare section of the signal.

Compute Lyapunov Exponents.

Compute Fractal Dimension.

In the following discussions, four examples are selected to illustrate the above approaches. A lucid exposition of chaos is presented in Crutchfield [Ref 6.2].

B. ILLUSTRATIVE EXAMPLES

Four examples, each increasingly more complex in dynamics, will illustrate various aspects of each approach. The first simple example, referred to in this report as the "32 Hertz" example, is a sinusoidal signal given by the following formula:

$$f(t) = 1 + 0.25 \sin(32t) \quad (6.1)$$

Figure 6-1(a) presents a portion of this signal. This example closely models the 4P vertical vibration in a four bladed helicopter.

The next example, referred here as the "Harmons" example, consists of a signal obtained by summing twelve sinusoidals together given by the following formula:

$$f(t) = 1 + \sum_{i=1}^{12} a_i \sin(\omega_i t + \phi_i) \quad (6.2)$$

The sinusoidals are harmonics of each other with the first harmonic at 8 Hertz, the second at 16 Hertz, the third at 24 Hertz, and so on, to the twelfth at 96 Hertz. Table 6-1 gives the amplitude, frequency and phase of each component. Figure 6-1(b) graphs a portion of this signal. This example closely models the output from many of the comprehensive helicopter analysis programs, such as CAMRAD, RACAP, and DYSCO [Ref 2.1, 2.2 and 2.3]. This example may also be viewed as an adaptation of the next example. The amplitudes, phases, and frequencies in Table 1 were computed by transforming the next example into the frequency domain. The amplitudes and phases were then estimated and recorded at the harmonic frequencies.

The third example, referred here as the "Actual" example, consists of flight test data. The data is taken from a vertical accelerometer located under the right pilot's seat. The conditions of flight are level flight at 60 knots and the HHC system is turned off. Figure 6-1(c) plots a portion of this data.

The fourth example, referred here as the "Random" example, consists of random noise. Figure 6-1(d) plots a portion of this signal. The signal consists of random noise generated by a random number generator.

Each of the examples were digitized at the rate of 1230 Hertz and 5 seconds duration of data were generated. Hence, a total of 6150 data points were recorded for each example. This digitizing rate and record length matched with the data obtained from flight test.

C. TIME HISTORY

A first step in identifying chaos is to examine the time history of the signal. A motion with no pattern or periodicity is either chaotic or random. In Figure 6-1(a), the 32 Hertz signal is periodic. In Figure 6-1(b), the Harmons signal is also periodic. However, in Figure 6-1(c), the Actual signal appears not to be periodic. It may be chaotic or random. The signal exhibits no visible regular pattern but contains a strong 32 Hertz (4P) component. In Figure 6-1(d), the Random, the signal appears chaotic or random. One can only determine whether a signal is periodic or not periodic by examining its time history [Ref 6.3].

The subroutine TIMSER of the program CHAOS produced Figure 6-1.

D. FOURIER SPECTRUM

One of the clues to detecting chaos in a dynamic system is the existence of broad band fourier spectrum. The Fourier spectrums are very good for separating a periodic phenomena from chaotic or random phenomena. In Figure 6-2, parts (a) through (d) give the Fourier spectrums for the 32 Hertz, the Harmons, the Actual, and the Random signals, respectively. The Fourier spectrum of the 32 Hertz and the Harmons signals are just spikes, while a broad band spectrum is seen in the Actual and Random signals. For periodic motion, the Fourier spectrum shows a set of narrow spikes or lines. This indicates the signal is a discrete set of harmonic or sinusoidal functions. Near the onset of chaos, however, a continuous distribution of frequencies appear [Ref 6.4]. In Figure 6-2(c), the level of this distribution is more than two orders of magnitude above the horizontal line representing calculation noise. In a fully chaotic regime, the continuous spectrum may dominate the discrete spikes. Although useful in indicating the existence of chaos, the Fourier spectrum reveals nothing about the structure of the phenomena. The Fourier spectrum by itself can not distinguish between chaotic phenomena involving a small number of degrees of freedom and random vibrations.

Note that a horizontal dashed line indicates the calculation noise level. On transforming a signal from the time domain to the frequency domain, there is a calculation noise due to the finite precision of the computations. The calculation noise is equal to the output of the fourier transform above the frequencies of the anti-aliasing filter. The anti-aliasing filter removes all signals above a selected frequency. The output of the Fourier transform above this frequency is due to calculation noise. Figure 6-3 illustrates the determination of calculation noise.

The subroutine PSD of the program CHAOS produced Figure 6-2 and 6-3.

E. THE 2-DIMENSIONAL PHASE PLANE

Information leading to the understanding of nonlinear dynamics may be obtained by examining the 2-dimensional (2-D) phase plane. In the phase plane, the complete state of knowledge about a dynamical system at a given instant collapses to a point. At the next instant the system dynamics change, and the point is displaced. A moving point charts the history of the system. In the phase plane, the coordinate axes may be selected as any two independent quantities which best described the dynamics of the system. In the study of vibrations, a

classical choice is to select amplitude and velocity of motion.

Consider the 32 Hertz example which represents the amplitude response of the motion of a simple pendulum. Differentiating the signal provides the velocity of motion. The amplitude and the velocity of the pendulum varies with time as the pendulum oscillates. Figure 6-4 presents the motion of a pendulum as represented in a classical phase plane. The horizontal axis is the amplitude and the vertical axis represents the velocity. As the pendulum swings back and forth, it trades kinetic energy for potential energy. In sketch at the top of Figure 6-4, the pendulum has maximum potential energy. As the pendulum swings down, the amplitude decreases while the velocity of the mass increases. The maximum velocity of the mass occurs when amplitude is zero. This figure shows a succession of states, and their corresponding representations in the phase plane, as the pendulum swings back and forth.

Connecting the states of the pendulum in the phase plane gives a circle which represents the motion of the pendulum over one complete cycle. This curve representing the motion of the pendulum is called the "trajectory." In Figure 6-4, the pendulum is assumed to be frictionless and will continue to oscillate indefinitely. An important observation for periodic

motion is that the trajectory forms a closed orbit in the phase plane. A "limit cycle" is another name for such closed orbits and the time taken for one orbit is the "period" of the motion.

F. TAKENS'S THEOREM

Before examining the representations of the other examples in the 2-D phase plane, consider another useful technique. The construction of 2-D phase plane requires two variables, namely, the amplitude and the velocity of motion. In typical flight test, however, only one vibration variable is usually measured, either the amplitude from a strain gage or the acceleration from a accelerometer. In both instances, the choice then is either to differentiate the strain gage signal (once, for velocity) or integrate the accelerometer signal (once, for velocity and twice, to obtain amplitude).

However, integrating or differentiating a signal also has the effect of filtering the signal. Differentiation of a signal will amplify the high-frequency noise, and attenuate the low frequency signal. The effect of differentiating is illustrated by the following example. Consider the signal given by equation (6.3)

$$f(t) = \sin(0.1t) + \sin(t) + \sin(10t) \quad (6.3)$$

Differentiating the equation (6.3) gives equation (6.4):

$$f'(t) = 0.1 \cos(0.1t) + \cos(t) + 10 \cos(10t) \quad (6.4)$$

Observe that differentiation attenuates the low frequency or 0.1 Hertz signal by a factor of 10. It leaves the 1 Hertz signal unchanged, but increases the 10 Hertz signal by a factor of 10.

Similarly, integration produces an effect opposite to that of differentiation. It amplifies the low frequency components of a signal while attenuates the high frequency components.

Thus the procedure to construct phase space diagrams is inaccurate when the data is obtained from one experimental observation. The solution came in 1980, when Packard et al. [Ref 6.5] conjectured and later Takens proved [Ref 6.6] a new method where 'fake' observables are obtained from only one observable. A typical experimental observation consists of a time series. A time series is an array of numbers representing the value of the observed quantity at regular intervals of time. Takens' method involves displacing the time value to produce any desired number

of more 'fake' observables. Consider the following example:

Series 1 1.43, 1.40, 1.35, 1.32, 1.28, 1.31, . . .
Series 2 1.40, 1.35, 1.32, 1.28, 1.31, . . .

Let Series 1 be the digitized values of an observable, say for example, the vertical acceleration under the pilot's seat. Then, Series 2 is the 'fake' observable formed by displacing the time series by one sample. This displacement is referred to as "embedding time." In this example, the embedding time was set equal to one sample. By taking the points in Series 1 as the x-coordinate, and the corresponding points in Series 2 as y-coordinate, a trajectory in 2-D phase plane may be drawn. In other words, to form a trajectory, plot successive columns of pairs. For example, the first pair is (1.43, 1.40) and the second pair is (1.40, 1.35). To illustrate an embedding time of 2 samples, consider the two series:

Series 1 1.43, 1.40, 1.35, 1.32, 1.28, 1.31, . . .
Series 3 1.35, 1.32, 1.28, 1.31, . . .

Again, Series 1 is the observable, the same as before. Series 3 is the new 'fake' observable with an embedding time of 2. Use the same method to form a trajectory by

plotting successive columns of pairs. The first pair is (1.43, 1.35), the second is (1.40, 1.32), and so on. This method of forming 'fake' observables and plotting is called the "pseudo phase plane" method [Ref 6.6].

Mathematically, this process may be described as:

$$(x(t), x(t - E)) \text{ or } (x(t), x(t + E)) \quad (6.5)$$

where:

$x(t)$ is the measured variable

E is the embedding time

t is the sampling time

An important parameter, then, is the embedding time and it depends to a large extent on the system dynamics. Useful hints in the selection of this parameter is discussed later.

Takens shows that a closed trajectory in a classical phase plane will also be closed in pseudo phase plane. Similarly, trajectories that show certain structure and shape in the classical phase plane show similar characteristics in pseudo phase plane. Chaotic trajectories in one look chaotic in the other. The principal advantage of Takens method is that a single observable is adequate to construct the pseudo phase portrait that can capture the system dynamics, and

eliminate the need for differentiation or integration of the observed signal. Furthermore, Takens proved that any representative quantity such as amplitude, velocity, acceleration, etc. may be plotted in the pseudo phase plane to study the behavior of a given nonlinear dynamic system.

G. 2-D PHASE PLANE AGAIN

Now consider the four examples described earlier and apply the pseudo phase plane method. To illustrate the effects of embedding time, three different choices of embedding times are used. The horizontal axis is the observable and the vertical axis is the first 'fake' observable. Figures 6-5(a), (b) and (c) depicts the 32 Hertz example for embedding times of 1, 10 and 19 samples, respectively. Figure 6-5(b) looks similar to Figure 6-4, the classical phase plane.

Figures 6-6(a), (b) and (c) represents the Harmons signal. A periodic signal is known to yield a closed orbit in the phase plane. Further, the orbit seems to cross over itself at several points.

Figures 6-7(a), (b) and (c) shows the Actual signal. The trajectory forms orbits which never repeat or close. The accelerometer data writes on top of itself to form a tangle of trajectories. The 2-D phase plane portrait

appears inadequate to discern all of the relevant information.

Figures 6-8(a), (b) and (c) represents the Random signal. Regardless of the embedding times, the trajectories are seen to fill the phase plane completely.

The subroutine PPLANE of the program CHAOS produced Figures 6-5 to 6-8.

H. EMBEDDING TIME

The issue regarding an appropriate choice for embedding time is addressed here. A too small embedding time, 'E', yields a phase portrait that is stretched out along the line $x = y$. A too large embedding time, in the case of a signal with a predominant frequency, yields a phase portrait stretched out along the line $x = -y$. One should compare several embedding times before settling on any particular choice of embedding time. This choice appears to be about one-quarter of the period of the most predominant frequency of the observable. In the preceding examples, 10 samples for embedding time is selected (sampling rate of 1230 Hertz, predominant frequency of 32 Hertz).

I. ENERGY IN THE PHASE PLANE

The phase plane constitutes a geometric method that provides a direct visual indication of the vibratory

energy in a signal. The greater the distance between the trajectory and the origin of the phase plane, the greater the magnitude of vibrations. With appropriate scaling, the area enclosed by the trajectories in the phase plane is a measure of the energy in the signal. This measure of energy is the same as the variance in the time domain or the area under the Power Spectral Density plot in the frequency domain.

J. 3-DIMENSIONAL PHASE SPACE

There are two ways of constructing a 3-dimensional (3-D) phase space. The first method is an extension of the pseudo phase space method, which is illustrated by the following example:

Series 1	1.43, 1.40, 1.35, 1.32, 1.28, 1.31, . . .
Series 2	1.35, 1.32, 1.28, 1.31, . . .
Series 3	1.28, 1.31, . . .

Series 1 is the observable, while Series 2 is a 'fake' observable formed by displacing the time series by two samples. The embedding time is, in this example, equal to two samples. Series 3 is a fake observable by displacing the second series by two samples. The data points in the three series yield the coordinates along 3 axes. To form a trajectory in 3-D phase space plot

successive columns of triples. In this example, the first triple is (1.43, 1.35, 1.28). Takens' method may be extended for any number of dimensions of pseudo phase space.

Mathematically, this process may be represented as:

$$\begin{aligned} & (x(t), x(t-E), x(t-2E), \dots, x(t-(m-1)E)) \quad \text{or} \\ & (x(t), x(t+E), x(t+2E), \dots, x(t+(m-1)E)) \end{aligned} \tag{6.6}$$

where 'm' is the number of embedding dimensions.

Figures 6-9, parts (a) through (d) presents the four examples. The subroutine PSPACE of the program CHAOS was used to produce this graph. The 32 Hertz signal in 3-D phase space is similar to that in the 2-D phase plane. The Harmons signal trajectories now form orbits which do not cross as in the 2-D phase plane. This example shows that in general, the effect of a higher dimensional pseudo phase space is to untangle the trajectories. The trajectories of the Actual signal form a small loop like shape. This is known as an "attractor." The trajectories are attracted to a small bounded space whose volume is small in comparison to the volume of the entire phase space. Although, the exact location of the a trajectory is unpredictable, it remains within the attractor. The Random signal is seen to fill up the

entire phase space. Further, for the 32 Hertz and Harmons signal, the orbits depicted are also attractors whose volume is very small.

An attractor is what the behavior of a bounded dissipative system settles down to, or is attracted to. A system may have several attractors. For example, consider an old fashioned grandfather pendulum clock. The clock pendulum has two attractors. Small displacements of the pendulum from its initial rest position will result in a return to rest position. This rest position is a "point attractor." However, with large displacements the clock begins to tick as the pendulum executes a stable oscillation or a "limit cycle" which is the other attractor.

In the case of a pendulum clock example, different initial conditions asymptotically approach to different attractors. The set of initial conditions or points in phase space that evolve to an attractor is its "basin of attraction." Small displacements form one basin of attraction while large displacements form another basin in case of the pendulum clock [Ref 6.7].

K. POINCARÉ SECTION

Before discussing a second way of constructing a 3-D phase space, consider the concept of a Poincaré section (PS). One method to construct a PS is by positioning a

2-dimensional surface in a 3-D phase space and observing the points where the trajectory pierces this surface. The PS takes a slice through the attractor, revealing the internal structure at this location. For given attractor, an infinite number of PS are possible, since an infinite number of locations and orientations on the attractor are available. An important question in constructing a PS is its location on the attractor.

In Figure 6-9(a), a 2-D plane is constructed for the 32 Hertz signal in 3-D phase space. This 2-D surface is an example of a PS. Figure 6-10, parts (a) through (d) are PS of the previous figure, all at the same location as in Figure 6-9(a). The subroutine PCARE2 of the program CHAOS generated the graphs in Figure 6-10. Observe that a periodic signal yields only one point on the PS and a signal with many harmonic components produces a finite number of points in a PS. The Actual signal produces intersections that are bounded to a small area while the Random signal intersections fill the entire PS plane.

This figure also illustrates another point. The points on the PS are the intersection of the trajectories with the plane, going in the same direction. The choice of the direction of the trajectories is yet another option available to the investigator in constructing the PS.

A well defined bounded attractor on a PS is a distinct indication of the presence of chaos. The structure of the attractor reveals the characteristics of system's nonlinear dynamics [Ref 6.1].

L. TOROIDAL PHASE SPACE

Now consider another method of constructing a 3-D phase space. To distinguish this approach from the pseudo phase space method, this method is referred to as the "Toroidal Phase Space" or "Torus" method. As the first step of construction, consider Figure 6-11(a) which shows the 32 Hertz signal with an embedding time of 10 samples. The time is recognized as the third axis, instead of the third 'fake' observable used in 3-D pseudo phase space. The trajectory is seen to wrap around the surface of a horizontal cylinder. Each wrap takes the same interval of time, namely, $1/32$ second. This time interval is the "Period" of the trajectory. Figure 6-11(a) presents a small duration of the 32 Hertz signal.

In Figure 6-11(b), the time axis is bent around to form a closed cylinder, or a torus. One revolution around the torus plots the entire 5 seconds of the 32 Hertz signal. A second closed circle inside the trajectories is an axis line and it represents the point of no vibration. The labeling of azimuth position about

the torus is similar to the labeling of helicopter rotor blade azimuth position.

Speeding up the rate of plotting the trajectories results in figure 6-11(c). One trip around the torus now takes exactly $1/32$ second. This rate of plotting results in the trajectories retracing themselves. In this case, the trajectories revisit the exact same space, called an attractor.

Figure 6-11 introduces a new parameter - the rate at which to plot around the torus. This parameter is not available in 3-D pseudo-phase-space. Classically, the plotting rate is fixed at a constant rate. A new concept, introduced here, is to synchronize the plotting rate with that of the forcing function, in this case the helicopter rotor. When the rate of plotting is synchronized with the rotor, the resulting trajectories are in the "Rotor time domain" while plotting the trajectories at a constant rate results in the "Clock time domain."

Figure 6-12 depicts the four examples. The plotting rate in parts (a), (b) and (d) is $1/32$ second for one revolution around the torus, or 32 Hertz. In part (c), the plotting rate is in the rotor time domain and the plotting rate is exactly four times around the torus for each rotor revolution. The embedding time is selected as 10 samples in all the cases. The 32 Hertz signal results

in a single line attractor. The Harmons signal appearance is similar to its appearance in 3-D phase space. The Actual signal yields an attractor. The Random signal appears to fill the torus.

The subroutine TORUS in program CHAOS was developed for the analysis described and it produced Figure 6-12.

M. POINCARÉ SECTIONS AGAIN

A plane is shown in the Figure 6-12(a), the 32 Hertz example in toroidal phase space. This 2-D surface is another example of a Poincare section (PS). The orientation of the 2-D plane is now fixed to pass through the vertical axis of the torus. A PS now corresponds to strobing the data at a specific azimuth angle and plotting the points where the trajectory pierces this section. The azimuth angle at which to take the PS is a parameter that must be selected.

Figure 6-13, parts (a) through (d) presents the PS of the previous figure taken at an azimuth angle of 270 degrees.

The subroutine PCARE of the program CHAOS was developed to obtain the Poincare sections.

N. VAN DER POL PLANE

Several PS taken at different azimuth angles of the torus reveal the internal structure of an attractor.

Rather than constructing an infinite number of PS, the "Van der Pol" plane captures the internal structure in a single plane. Figure 6-14 presents the Van der Pol construction [Ref 6.8]. This process is equivalent to untwisting the trajectories on the 2-D phase plane at a prescribed rate. Mathematically, the Van der Pol plane is computed by the following transformation:

$$U = X \cos(\omega t) - Y \sin(\omega t) \quad (6.7)$$

$$V = X \sin(\omega t) + Y \cos(\omega t)$$

where:

'X' and 'Y' are the coordinates of a trajectory in the 2-D phase plane.

'U' and 'V' are the coordinates of a trajectory in the Van der Pol plane.

'w' is the rate of untwisting.

The rate of untwisting is similar in nature to the plotting rate around the torus. The untwisting rate may either be at a constant rate or at a rate synchronized with that of the rotor.

The Van der Pol plane method works only for signals with a single predominant frequency. Three of the examples have a strong 32 Hertz component.

Figure 6-15 presents the four examples plotted in the Van der Pol plane. Subroutine VDP of the program CHAOS was developed to produce this transformation.

O. HIGHER DIMENSIONAL POINCARÉ SECTIONS

Takens shows that there is no limitation on the number of fake observables available from a given time history. To generate a 3-D Poincaré section (PS) from a 4-D hyperspace, consider the following series of data:

Series 1	1.43, 1.40, 1.35, 1.32, 1.28, 1.31, . . .
Series 2	1.40, 1.35, 1.32, 1.28, 1.31, . . .
Series 3	1.35, 1.32, 1.28, 1.31, . . .
Series 4	1.32, 1.28, 1.31, . . .

Again, the first series is the observable, while the second, the third, and the fourth series are fake observables formed by displacing the time series by an embedding time of one sample. The data in the four series provide the four coordinates in the 4-D hyperspace. These are referred to as "time delay coordinates." A column represents a point in 4-D hyperspace. To generate a PS, select a coordinate axis (say, series 3) and a coordinate (say, 1.28). Then Series 3 is scanned to yield all the points that equal 1.28 (interpolating Series 3 as required). A PS is then,

a plot in 3-D space of the respective triples of the points for Series 3 equal to 1.28. One such triple is (1.35, 1.32, 1.31). Thus, additional parameters for investigation are the choice of coordinate axis and the desired value for the PS.

Figure 6-16 shows the 3-D PS for the 32 Hertz, Harmons, Actual and Random signals, respectively. The results are similar to the earlier PS. Subroutine PCARE3 of program CHAOS was developed for this higher dimensional PS.

P. LYAPUNOV EXPONENTS

The geometric and topological methods discussed thus far are mainly qualitative in nature. One of the quantitative tests available is to compute the "Lyapunov Exponents" of the system. A Lyapunov exponent measures the exponential attraction or separation, over long periods of time, of two adjacent trajectories in phase space with different initial conditions. The Lyapunov exponent may be defined as:

$$d(t) = d 2^{Lt} \quad (6.8)$$

or

$$L = \log_2 \left(\frac{d(t)}{d} \right) \quad (6.9)$$

where:

'd' is the initial distance between the two trajectories.

'd(t)' is the distance between them at a later time.

'L' is the Lyapunov exponent.

Note that the logarithm is in base 2, and hence 'L' is in units of bits/sec.

A positive exponent means the later distance, 'd(t)', will be larger than the initial distance, 'd'. A zero exponent indicates that there is no change and a negative exponent indicates that 'd(t)' is smaller than 'd'.

Figure 6-17 illustrates these concepts.

Alternatively, the exponent gives a measure of the rate of information lost by the signal over an extended periods of time in terms of bits of information per second. Further, a positive exponent is yet another indication of inherent unpredictability and resulting chaotic behavior in the system.

Algorithms are available to calculate these exponents from the measurement of a single observable by constructing a pseudo phase space. The method used here is due to Wolf, et al. [Ref 6.9]. Other methods, but not used here, are due to Eckermann, et al. [Ref 6.10] and Tongue and Smith [Ref 6.11], among others.

The individual exponent calculations vary widely depending upon the point in the data record from where the initial distance, 'd', is measured. Figure 6-18, produced by subroutine LAP of the program CHAOS, illustrates how the exponent calculation varies with the initial point. The example used here is the Actual signal. A new exponent was estimated at intervals of every 50 data samples. Figure 6-18 plots over 300 estimates (50 samples x 300 estimates = 6000 total data points). Figure 6-19 shows the evolution of the average Lyapunov exponent from these estimates. The asymptotic value of 0.5 is obtained for the averaged exponent.

The averaged Lyapunov exponents for the four examples calculated by Wolf's method are given below:

32 Hertz signal	- 0.03 bits/sec
Harmons signal	- 0.05 bits/sec
Actual signal	0.3 to 1.7 bits/sec
Random signal	+ 0.3 bits/sec

The Lyapunov exponent calculation varied considerably for the Actual signal. Small changes in input parameters result in large changes in the final averaged exponent.

Periodic attractors, such as the 32 Hertz and Harmons examples, have only negative or zero exponents. This indicates that their motion is predictable. Furthermore,

changes in input parameters had little effect on the final exponent estimate.

An equal number of trajectories diverge and converge in a random process. The Random signal should have an averaged exponent near zero, even though a random process is unpredictable. The small positive exponent seen here may be a result of the limited data file (6150 points) used in the calculation. Changes in the input parameters had little effect on the exponent estimate.

Finally, 1-D systems have only a single Lyapunov exponent, while 2-D systems have two Lyapunov exponents, and so on.

Q. STRANGE ATTRACTORS

Consider the case of a 3-D system with one positive Lyapunov exponent and the rest being zero or negative. The system is also considered as being dissipative. A dissipative system is any system, such as a helicopter, which loses energy with time due to friction and other nonconservative forces. These systems stay in motion by receiving energy from an outside source. In the case of a helicopter, this energy is obtained from the rotor.

Study Figure 6-20 closely. The multidimensional attractors describing dissipative systems become effectively one-dimensional. In dissipative systems, the attractors have bounded volumes that shrink with time.

Although the volumes always shrink, the distance between neighboring trajectories may shrink or expand at different rates in different directions. The Lyapunov exponents describe this rate of shrinking or stretching. The direction of expansion defines a one-dimensional line that contains the attractor. The attractor shrinks in some directions and grows in others. This exponential growth is a local feature because the physical system is bounded. Hence, two trajectories on a chaotic attractor cannot diverge exponentially forever. Consequently the phase space in the attractor folds over onto itself. So, although the trajectories follow increasingly different paths, they eventually must pass close to one another again. Then the attractor, while thin, becomes complex in nature. The process of stretching and folding repeats itself, creating folds within folds. Attractors with this structure are called as "strange attractors." Figure 6-20 sketches the formation of a strange attractor.

In 3-D phase space, a strange attractor appears like a collection of infinite number of sheets or parallel surfaces. The separation of the surfaces is by distances that approach the infinitesimal. The appearance of a strange attractor in a Poincare section is a CERTAIN sign of chaos. When examined on a smaller scale, a strange attractor has a self similar structure. In other words,

magnifying any small part of the Poincare section reveals even more sheet like layers. In order to characterize such Poincare patterns, the term "fractal" is used [Ref 6.12].

However, finding strange attractors in actual experimental data is extremely difficult. In all but the simplest systems, the stretching and folding of phase space occurs in many directions. This interference makes observation of a strange attractor difficult in an experimental signal [Ref 6.13 and 6.14].

R. FRACTAL DIMENSION

Another quantitative measure of chaos is to compute a "fractal dimension," if it exists. The fractal dimension gives a the lower bound on the number of essential variables needed to model a systems dynamics. For example, if the fractal dimension is ,say, 6.5 for some system, then the minimum number of first-order differential equations required to simulate the dynamics of this system is 7. Furthermore, non-integer values for fractal dimension indicate the existence of a strange attractor, Berge [Ref 6.15].

There are at least six different ways to classify the nature of fractal dimension. The dimension discussed here is known as "correlation dimension". For further discussion on the different types of dimension, see for

example, J. D. Farmer, et al. [Ref 6.16]. Other relevant works are Malraison, et al. [Ref 6.17] and Froehling, et al. [Ref 6.18]. The correlation fractal dimension, 'd', is defined by the following equation:

$$C(r) = r^d \quad (6.10)$$

where:

'C(r)' is the probability of the attractor within a circle, sphere or hypersphere of radius 'r'.

'r' is the radius of a circle, sphere or hypersphere.

'd' is the fractal dimension.

Take the natural logarithm of both sides of equation 6.10 to solve for 'd':

$$d = \lim_{r \rightarrow 0} \left(\frac{\ln C(r)}{\ln r} \right) \quad (6.11)$$

Following Grassberger and Procaccia [Ref 6.19], a procedure to compute the correlation dimension is described. Consider Figures 6-21, the 32 Hertz signal in the 2-D phase plane. Remember this signal was digitized. Start with a point on the attractor and calculate the number of points inside a circle of radius 'r'. Calculate the probability 'C(r)' by dividing this number of points by the total number of points that make up the

attractor. Repeat this procedure for several points along the attractor. Then compute 'C(r)' for several values of 'r'. The slope of the log (C(r)) versus log (r) curve gives the correlation dimension 'd'. The validity of this power law is limited to values of 'r' reasonably small compared to the size of the attractor. In the 32 Hertz example, the dependence is linear and hence 'd' is equal to 1.

To obtain the fractal dimension of the attractor, the procedure has to be applied in 2-D, 3-D, 4-D, etc. pseudo phase space. The asymptotic value of the correlation dimension is the fractal dimension of the attractor.

This procedure is given by:

$$C(r) = \lim_{N \rightarrow \infty} \frac{1}{N^2} \sum_{i,j=1}^N H(r - \|x_i - x_j\|) \quad (6.12)$$

where:

'H' is the Heavside step function.

' $\|x - x\|$ ' is the Euclidian distance between the points.

and 'N' is the total number of points.

Figure 6-22 summaries the results for the four examples. The fractal dimension, 'd', for the 32 Hertz signal remains at 1 regardless of the dimension of the phase space. In contrast, the fractal dimension of the

Random signal roughly remains equal to the dimension of the phase space. The Random signal can be considered to be the superposition of an infinite number of independent oscillators. Their trajectories will densely cover any higher dimensional phase space.

As long as the fractal dimension is roughly equal to the dimension of the phase space used for the calculation, the attractor lies in a higher dimensional phase space. On the other hand, once the fractal dimension is independent of the dimension of the phase space used for the calculation and is non-integer, the signal is characterized as chaotic and accompanied by a strange attractor [Ref 6.15] & [Ref 6.19].

The subroutine COD of the program CHAOS was developed to compute the fractal dimension discussed here and produced Figure 6-21 and the results of Figure 6-22.

S. SUMMARY

In this chapter, geometric and topological methods of Chaos are described. Determination of the presence of Chaos from the analysis of a times series alone is difficult. No single approach provides a conclusive evidence of chaos. They all must be used together, each providing evidence to suggest the presence of Chaos.

Table 6.1

Coefficients Used for Harmons Example (Equation 6.2)

i	a_i	w_i	θ_i
1	0.014	8.0	345
2	0.014	16.0	255
3	0.009	24.0	076
4	0.228	32.0	296
5	0.025	40.0	033
6	0.017	48.0	014
7	0.025	56.0	034
8	0.044	64.0	225
9	0.013	72.0	352
10	0.011	80.0	195
11	0.012	88.0	187
12	0.020	96.0	106

Note: a_i is in units of "g's"

w_i is in units of hertz

and θ_i is in units of degrees.

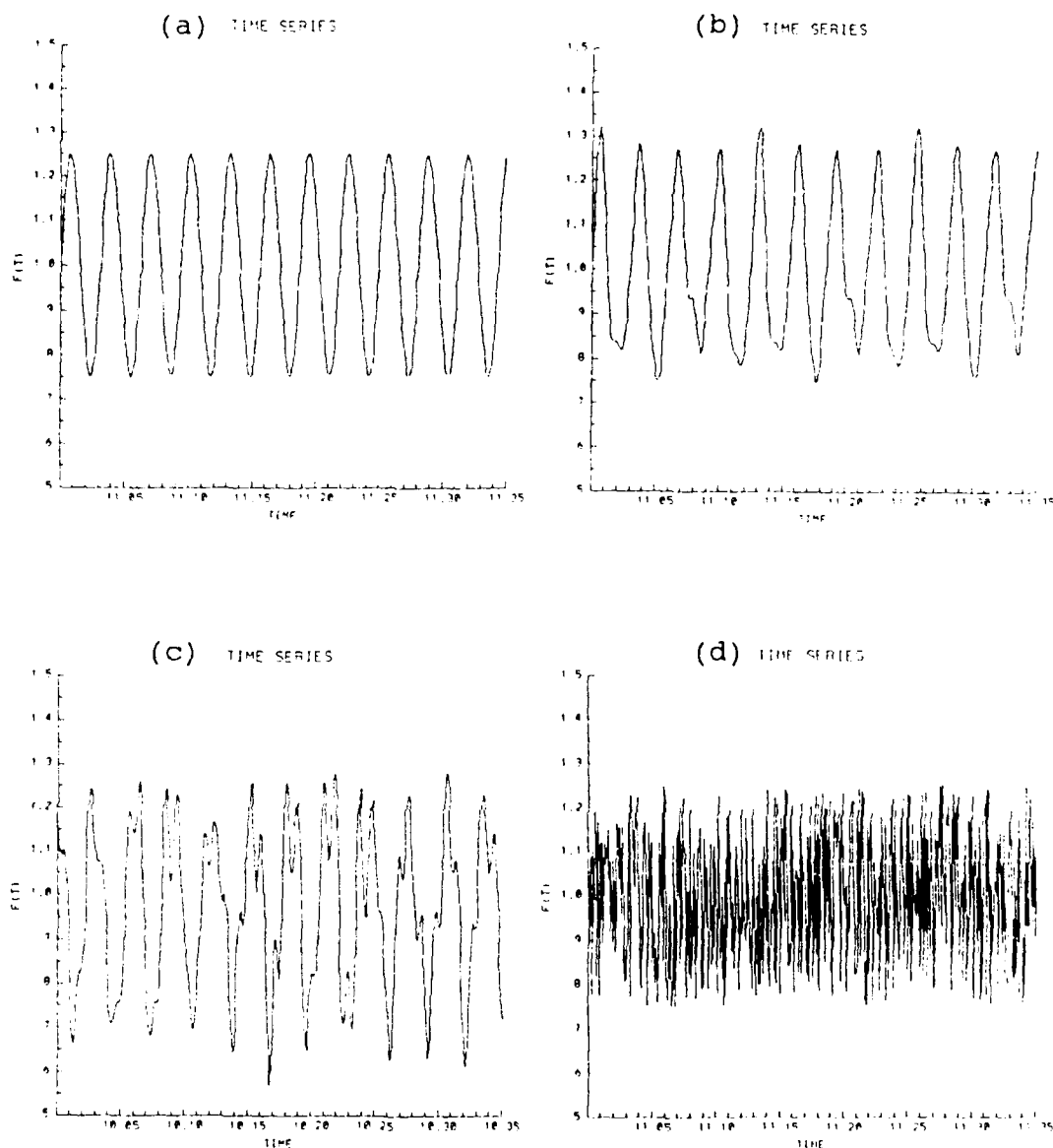


Figure 6-1. Time Histories. The time histories of the four examples used throughout this chapter. (a) 32 hertz. (b) Harmonics. (c) Actual. (d) Random.

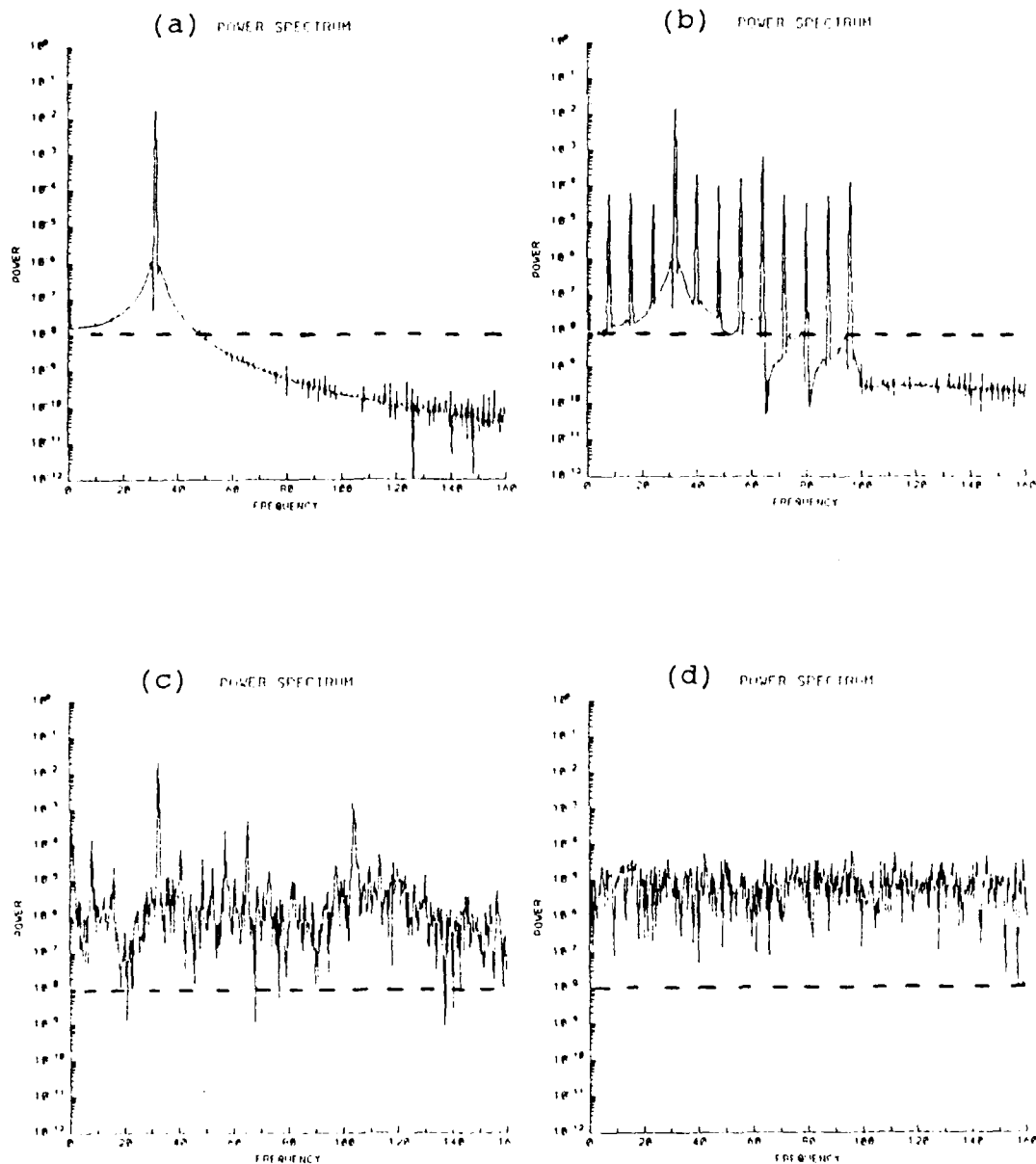


Figure 6-2. Fourier Power Spectrums. (a) 32 hertz. (b) Harmonics. (c) Actual. (d) Random. Horizontal dashed line indicates instrument and calculation noise. Units of part (c) is in "g's" squared. Transformation used 4096 points and a Hamming window.

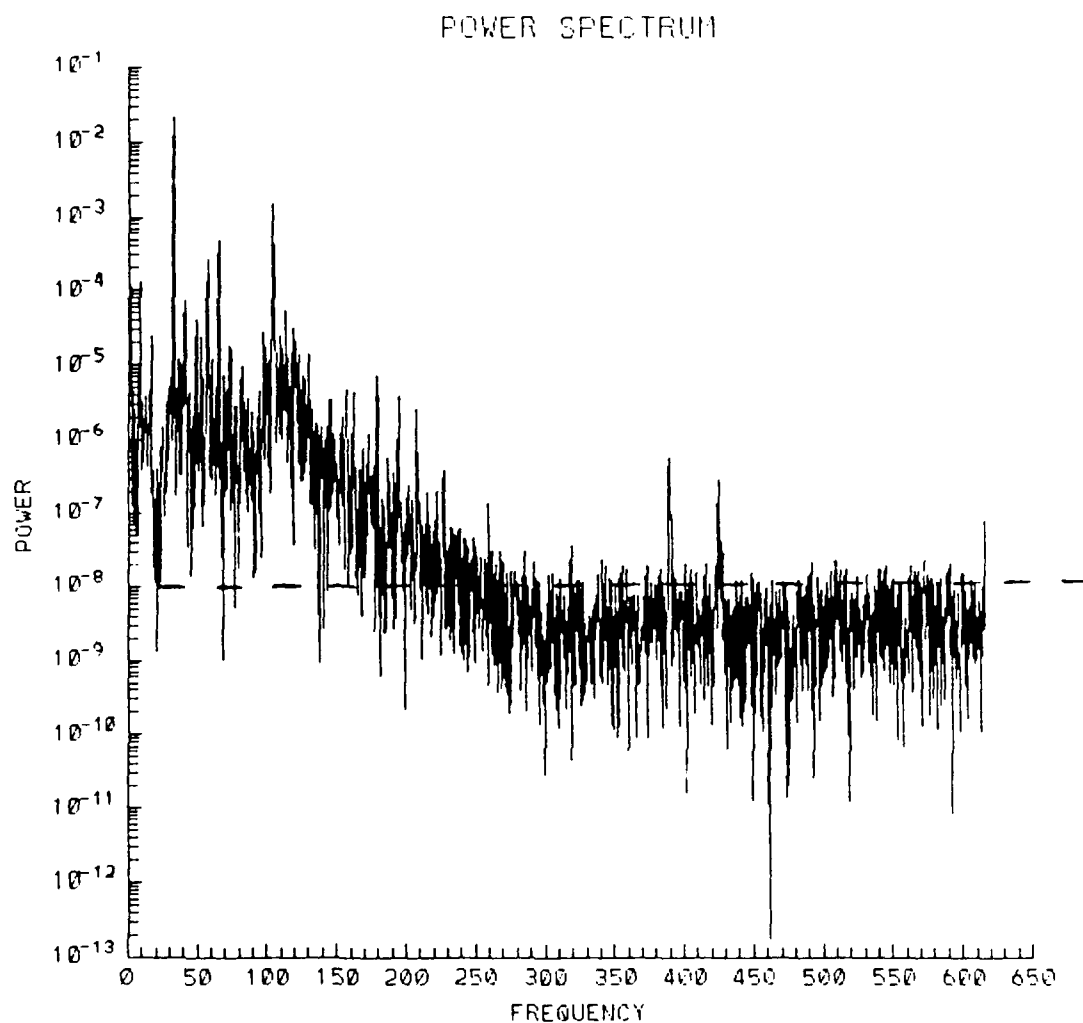


Figure 6-3. Determination of Calculation Noise.
Fourier spectrum for Actual example. The anti-aliasing filter removed all signals above the frequency of 250 hertz. Calculation noise is equal to the output of the fourier transform above 250 hertz.

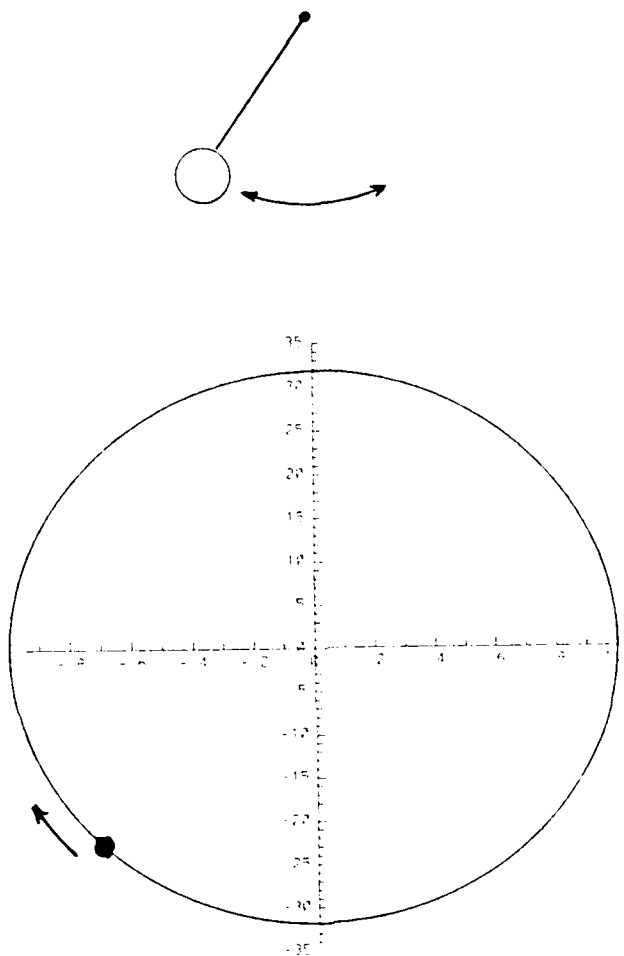


Figure 6-4. 2-Dimensional Phase Plane Portrait of a Pendulum. The horizontal axis plots amplitude and the vertical axis plots velocity of the pendulum's swinging. One point on this plane contains all the information about the state of the pendulum at any instant of time. Connecting the points yields a smooth circle which represents trajectory of the pendulum. This pendulum is frictionless.

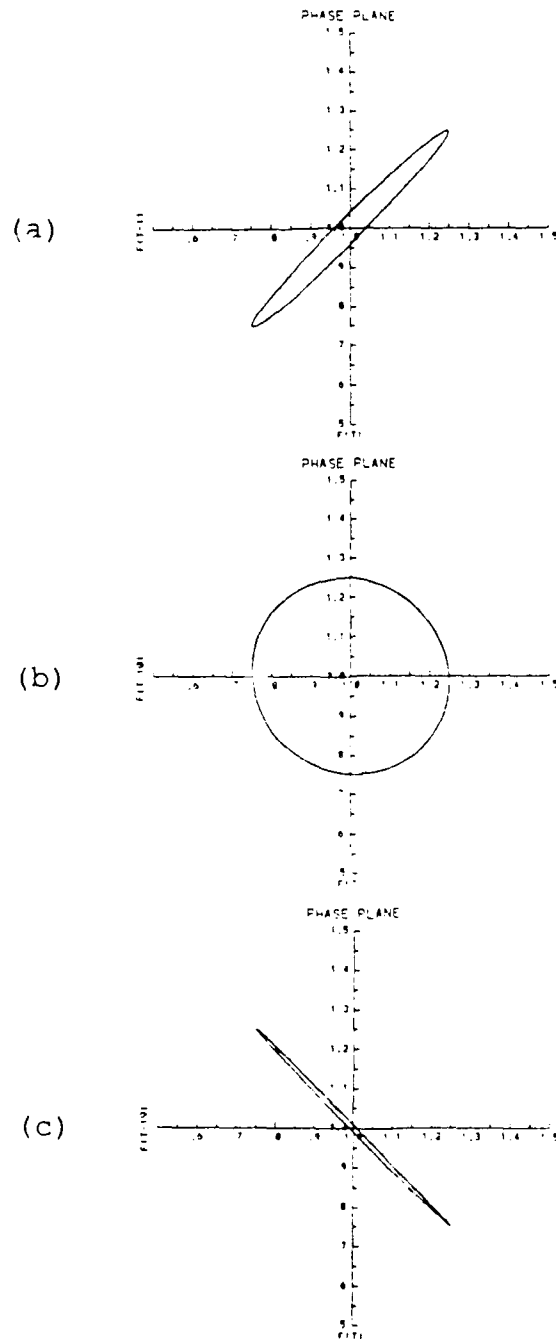


Figure 6-5. Pseudo-phase-plane representation of 32 hertz example. Presented for three different choices of embedding time. (a) 1 sample. (b) 10 samples. (c) 19 samples. Part (b) looks just like figure 6-4.

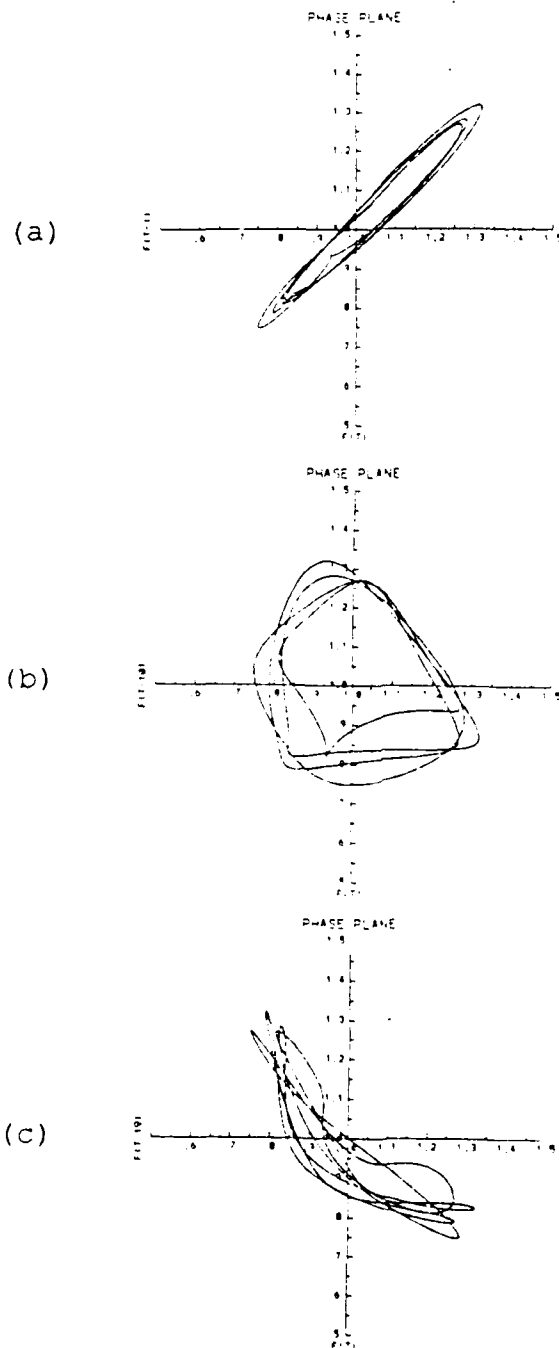


Figure 6-6. Pseudo-phase-plane representation of Harmons example. Presented for three different choices of embedding time. (a) 1 sample. (b) 10 samples. (c) 19 samples.

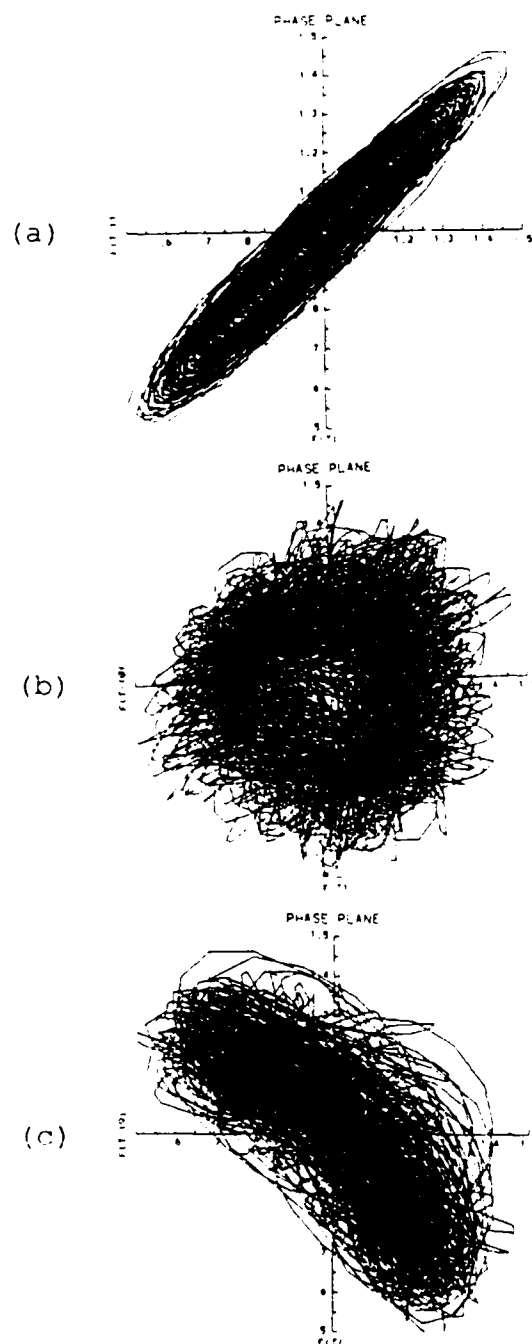


Figure 6-7. Pseudo-phase-plane representation of Actual example. Presented for three different choices of embedding time. (a) 1 sample. (b) 10 samples. (c) 19 samples.

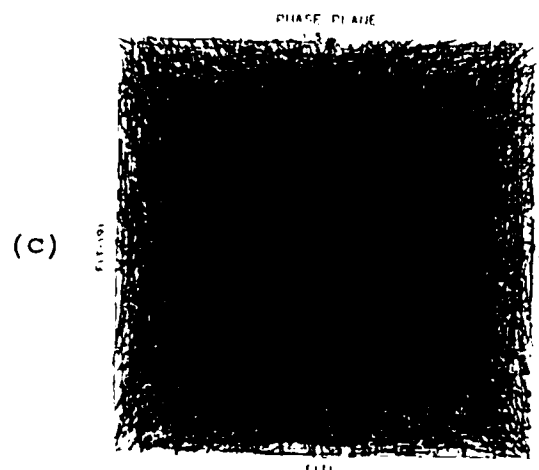
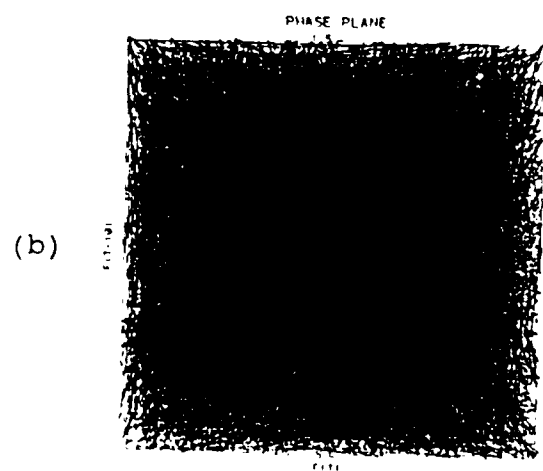
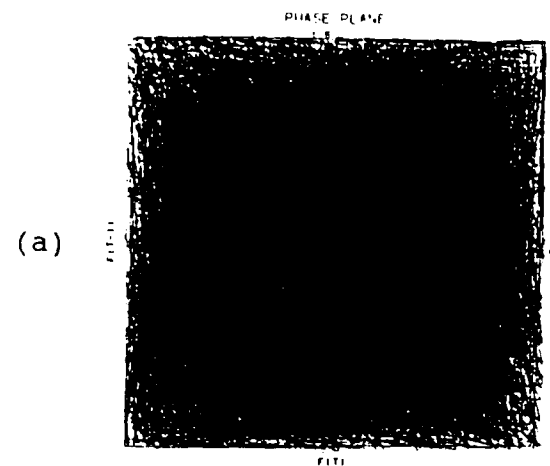


Figure 6-8. Pseudo-phase-plane representation of Random example. Presented for three different choices of embedding time. (a) 1 sample. (b) 10 samples. (c) 19 samples.

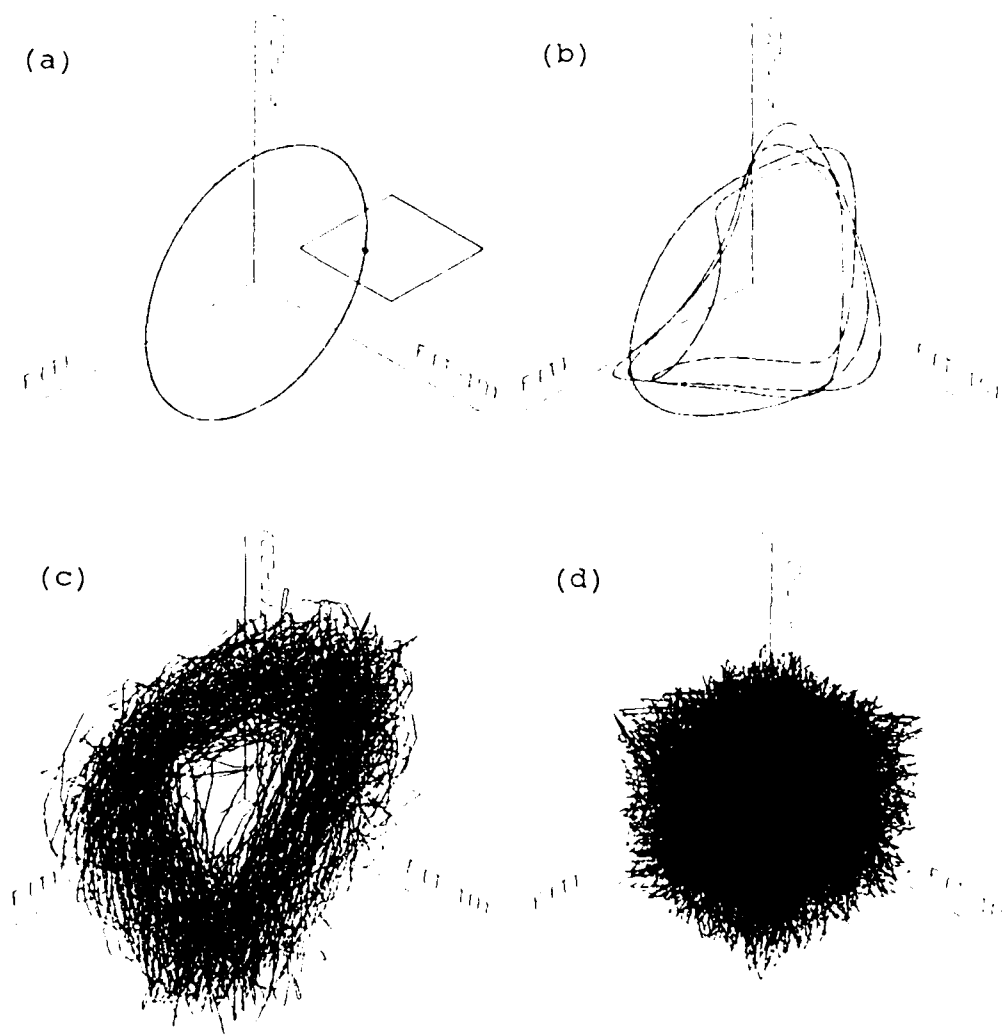


Figure 6-9. 3-Dimensional Phase Space. (a) 32 hertz. (b) Harmonics. (c) Actual. (d) Random. Embedding time is 10 and 20 samples for axis labeled $F(T-10)$ and $F(T-20)$ respectively. The construction of a Poincare section is illustrated in part (a). The section consists of those points where the trajectory pierces the plane in the same sense (direction).

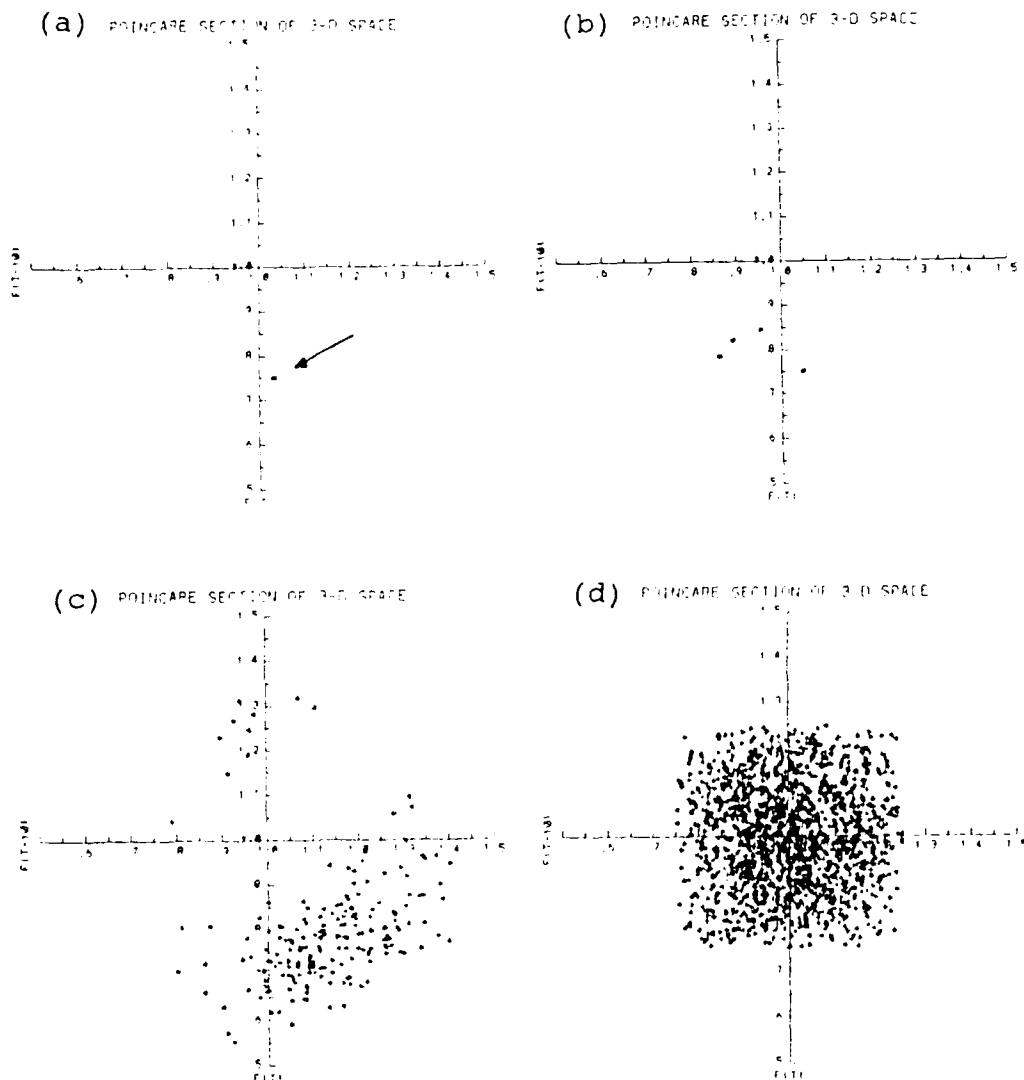


Figure 6-10. Poincare Sections of 3-D Phase Space. Poincare sections of the examples presented in Figure 6-8. (a) 32 hertz. (b) Harmonics. (c) Actual. (d) Random. Section taken at $F(T-20)$ equal to 1.0. Plotted are only intersections of trajectories traveling upward.

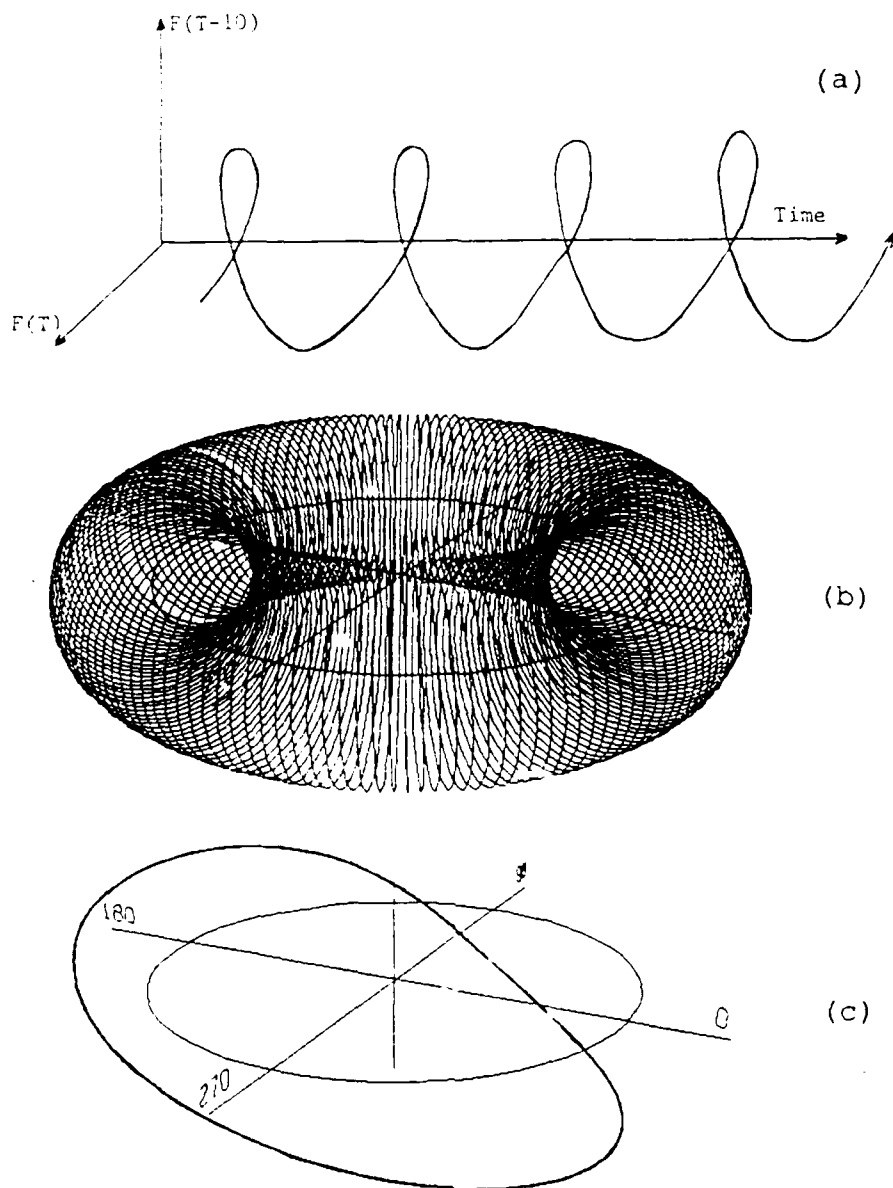


Figure 6-11. Construction of Toroidal Phase Space.
 (a) The time series representation of the 32 hertz example. The trajectory wraps around an apparent cylinder. The cylinder is not a feature, but just a step in the graphical construction. Part (a) plots only a portion of the five seconds of data. (b) Connecting the ends of the cylinder forms toroidal phase space. The entire data record presented here. (c) Speeding up the rate of plotting gives an attractor. The trajectories retrace themselves, over and over.

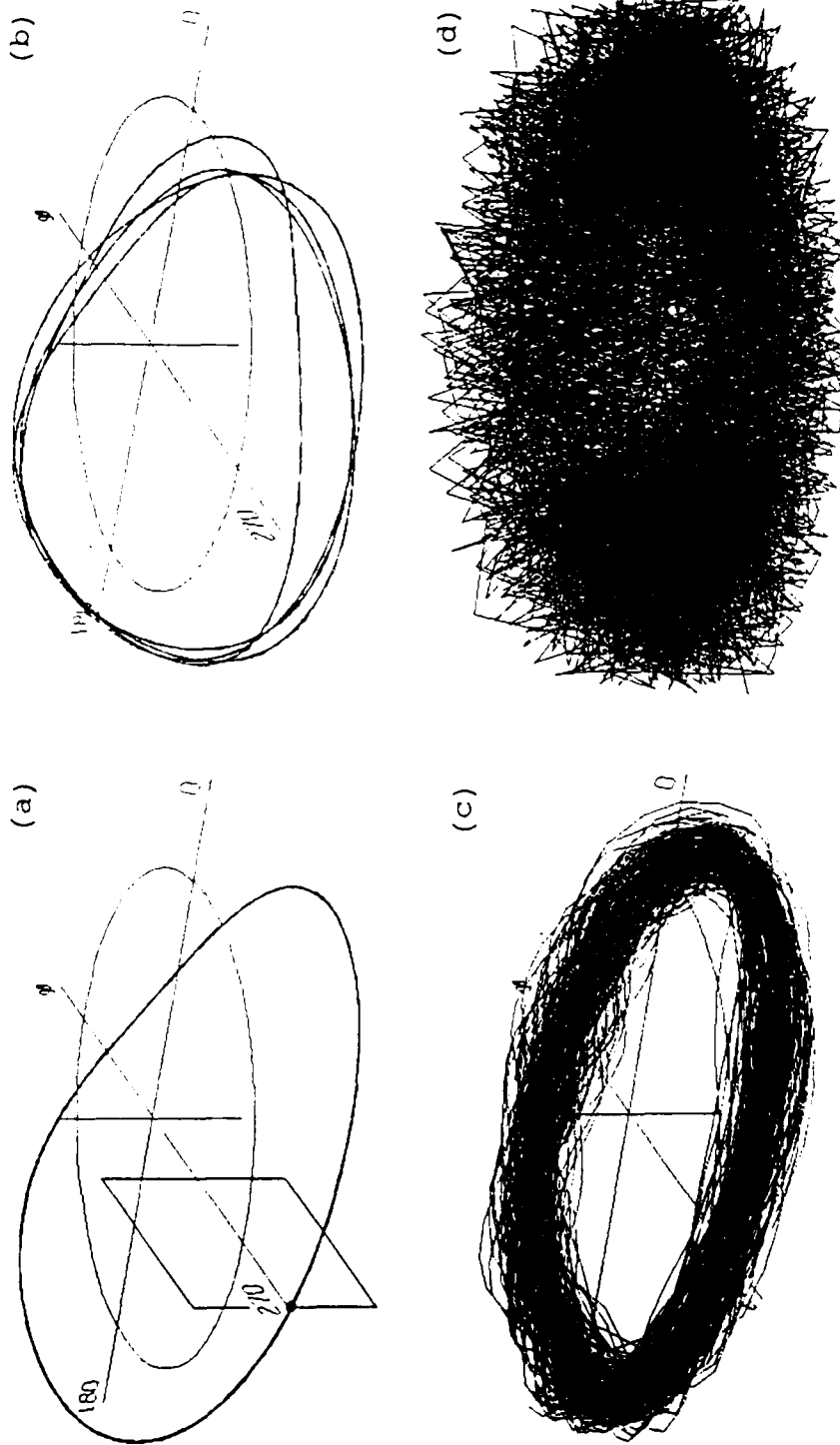


Figure 6-12. Toroidal Phase Space. (a) 32 hertz. (b) Harmonics. (c) Actual. (d) Random. Rate of plotting around the torus is 32 hertz for parts (a), (b) and (d). In part (c), the rate is synchronized at four times around the torus for each rotor revolution. Embedding time is 10 samples.

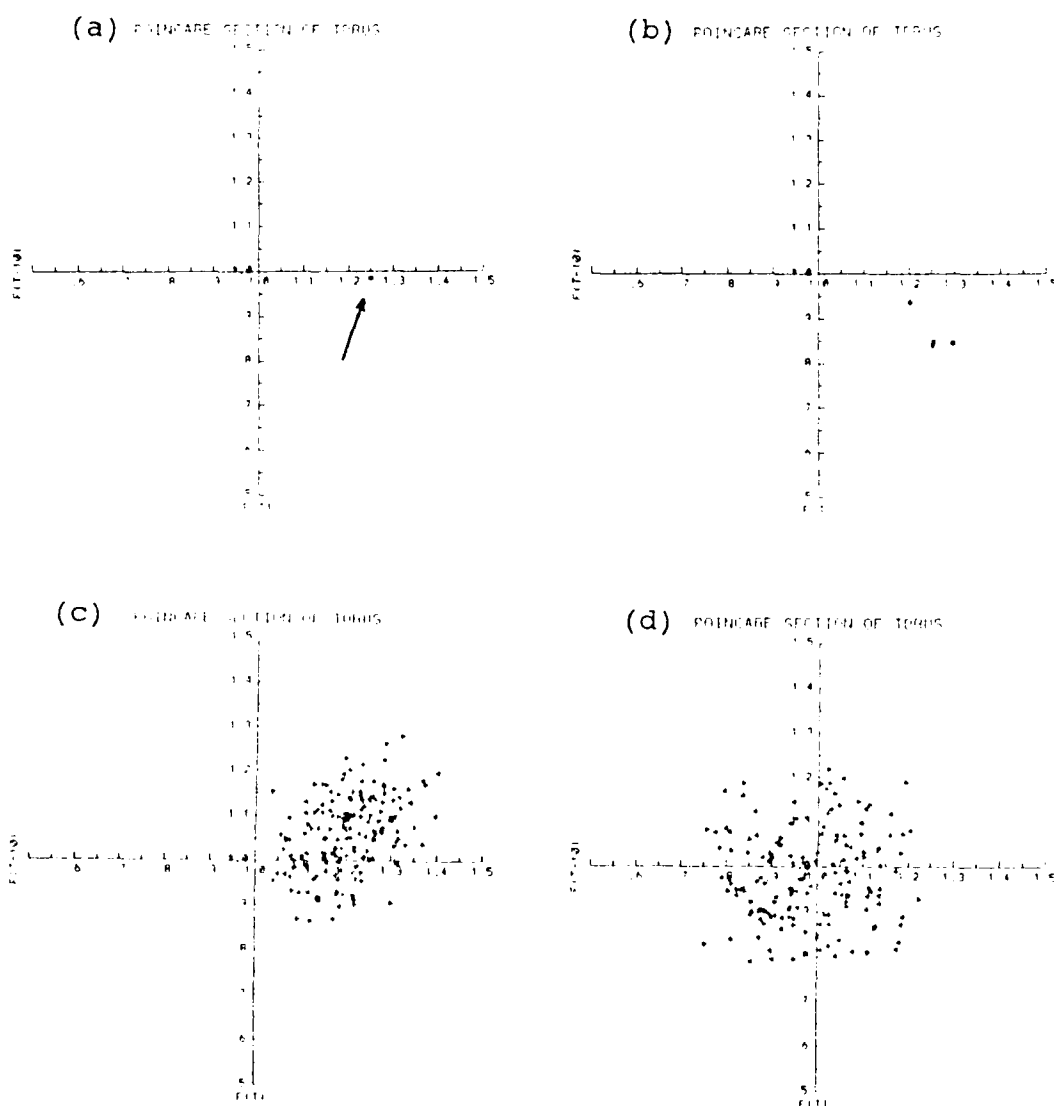


Figure 6-13. Poincaré sections of Figure 6-12. All sections are at an azimuth angle of 270 degrees. Embedding time is 10 samples. (a) 32 hertz. (b) Harmonics. (c) Actual. (d) Random.

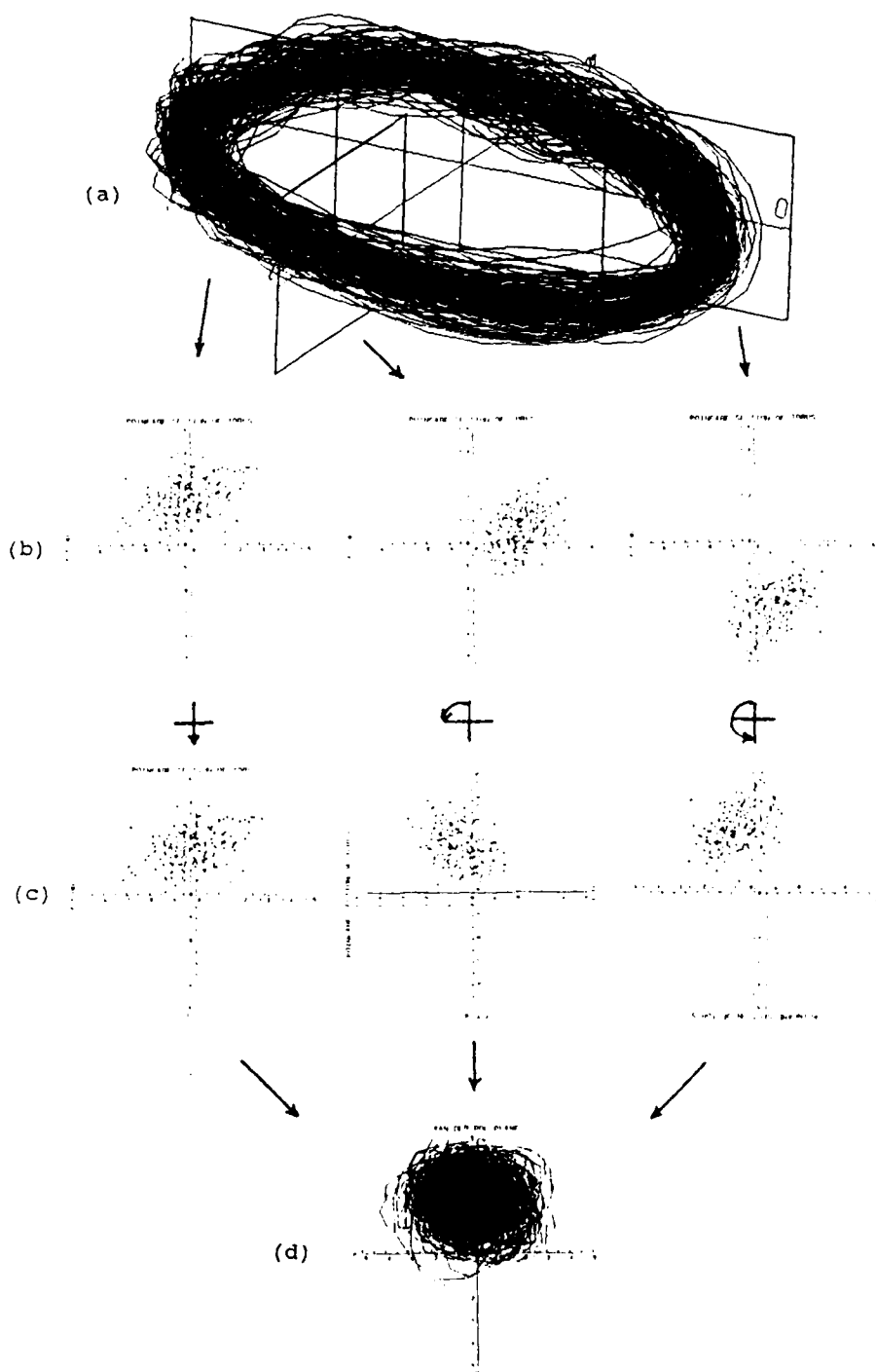


Figure 6-14. Construction of the Van der Pol plane.
 (a) The Actual signal plotted in toroidal phase space with plotting rate synchronized with the rotor. (b) Poincare sections taken at 180, 270 and 0 degrees azimuth. (c) Poincare sections rotated; the 180 degree azimuth section is not rotated, the 270 degree azimuth section rotated 90 degrees, the 0 degrees azimuth section rotated 180 degrees. (d) Sections combined to form Van der Pol plane.

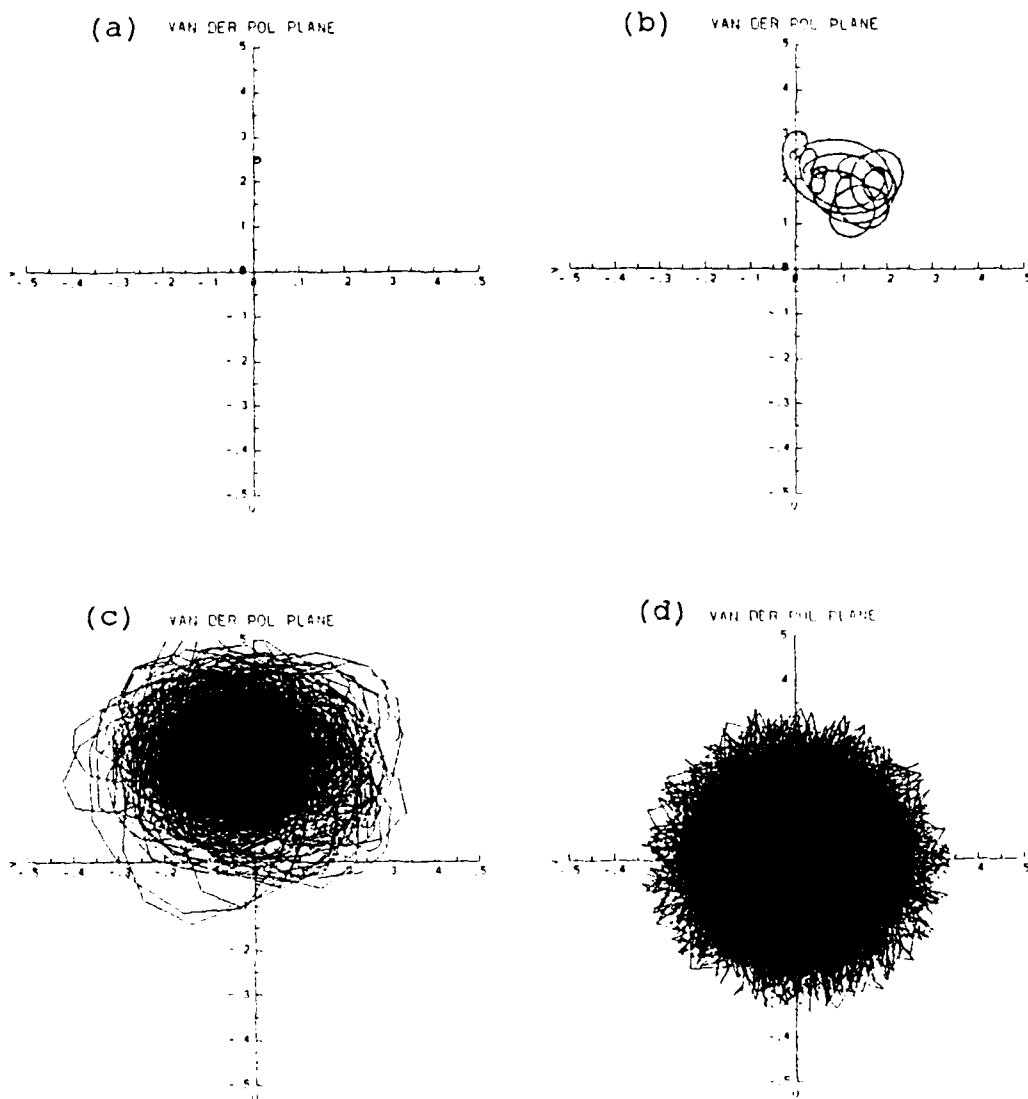


Figure 6-15. The Van der Pol Plane. (a) 32 hertz. (b) Harmonics. (c) Actual. (d) Random. Rate of untwisting is 32 hertz for parts (a), (b) and (d). Synchronized with rotor for part (c). Embedding time is 10 samples.

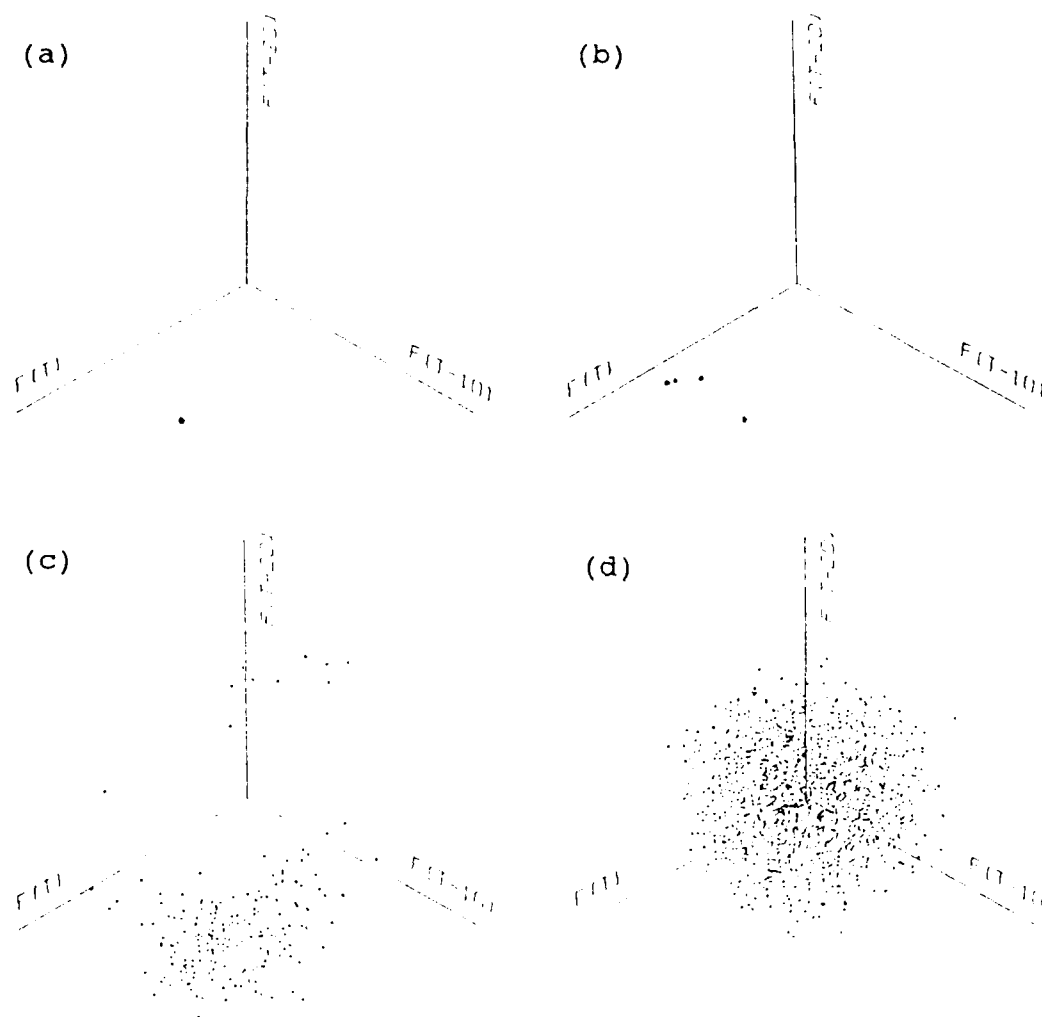
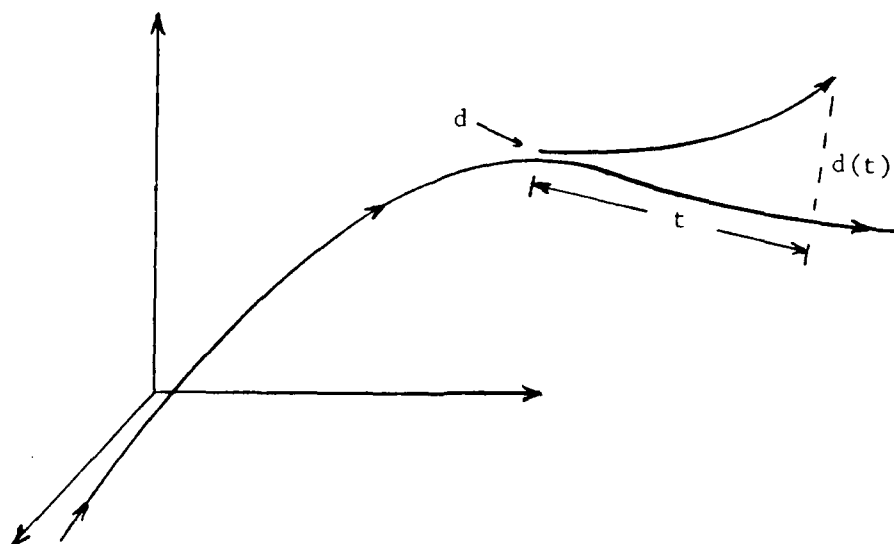


Figure 6-16. 3-D Poincare Sections of 4-D Hyperspace. The section is formed by strobing the fourth data array, $F(T-30)$, at a value of 1.0. Embedding time is 10 and 20 samples. (a) 32 hertz. (b) Harmonics. (c) Actual. (d) Random.



$$d(t) = d 2^{Lt}$$

Figure 6-17. Lyapunov Exponents. Sketch of the change in distance between two nearby orbits used to define the largest Lyapunov exponent.

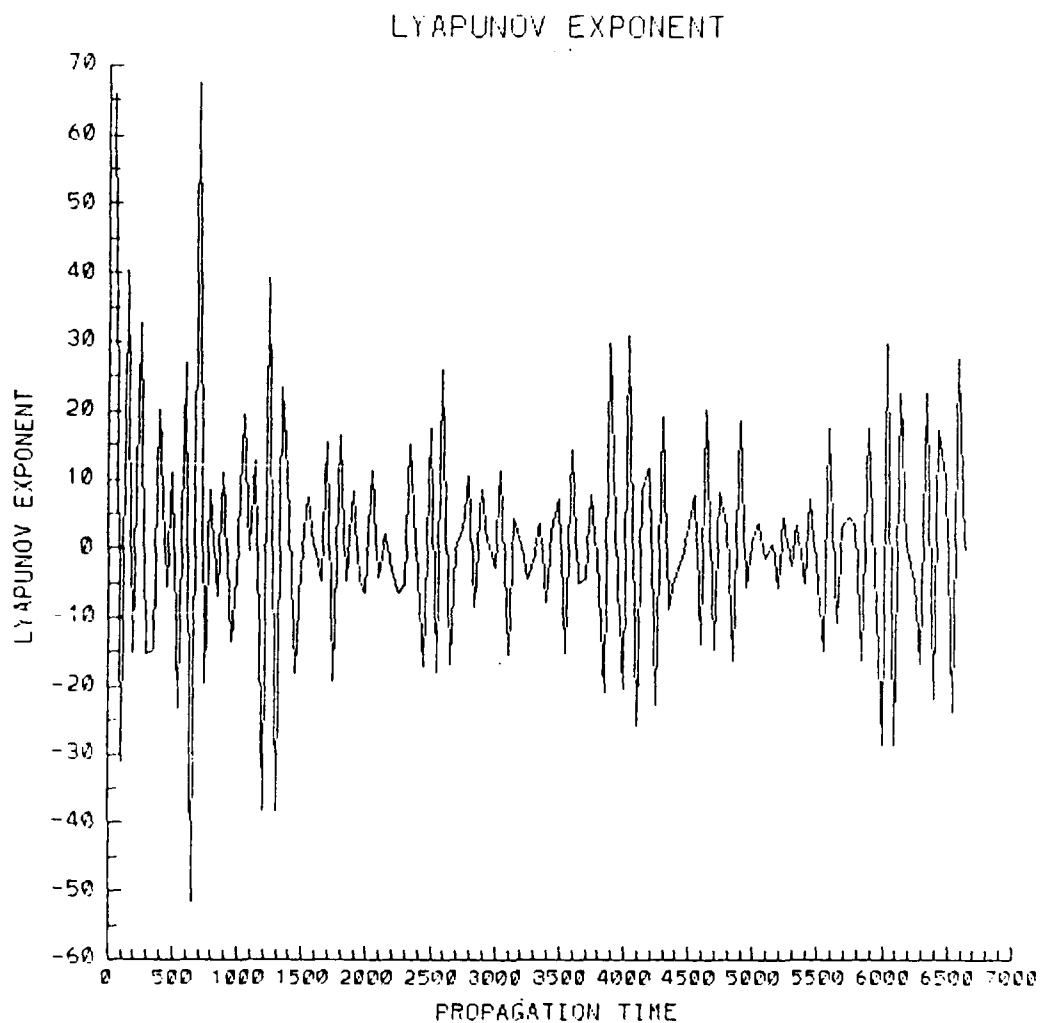


Figure 6-18. Instantaneous Lyapunov exponent for the Actual Signal. The horizontal axis, Propagation Time, refers to the position in the data record of the initial point. Conditions were level flight, 60 knots and HHC off.

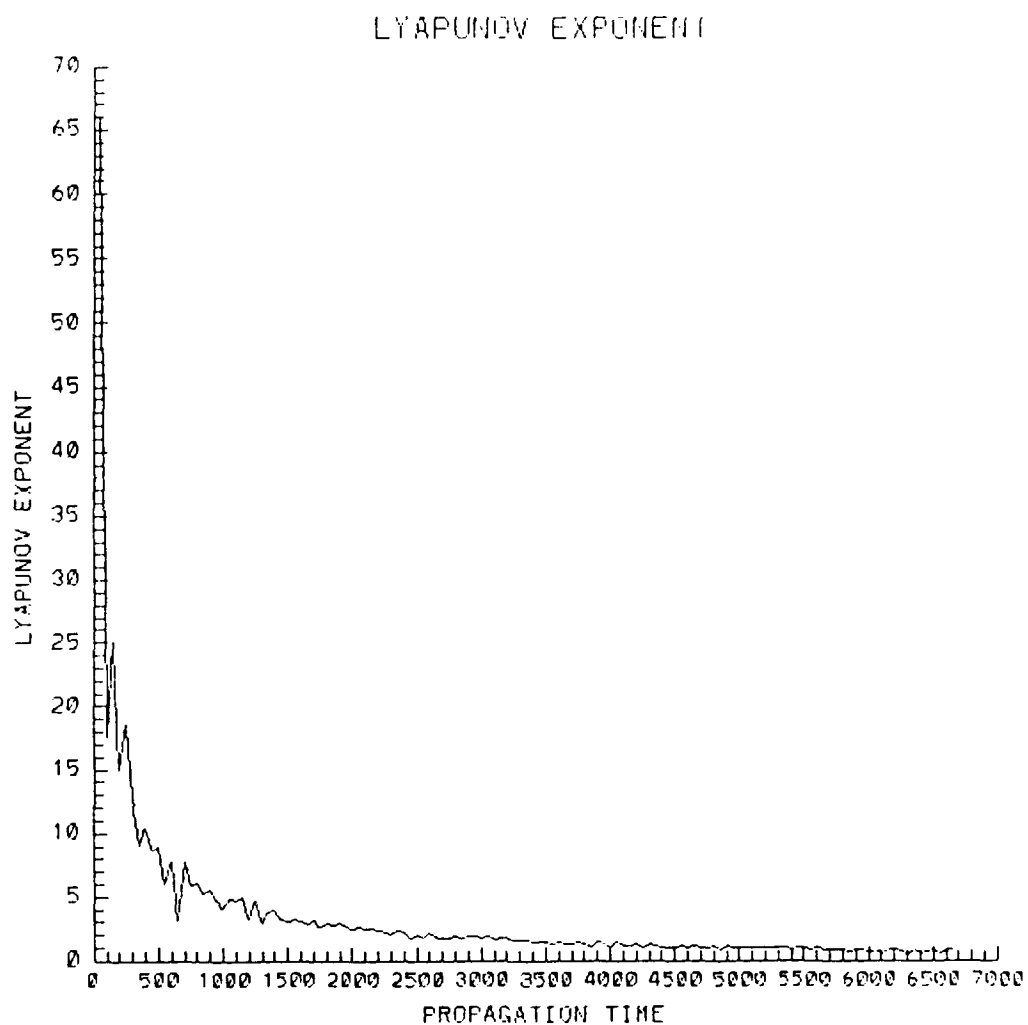


Figure 6-19. Average Lyapunov exponent for figure 6-18. Plot shows running average of instantaneous Lyapunov exponent.

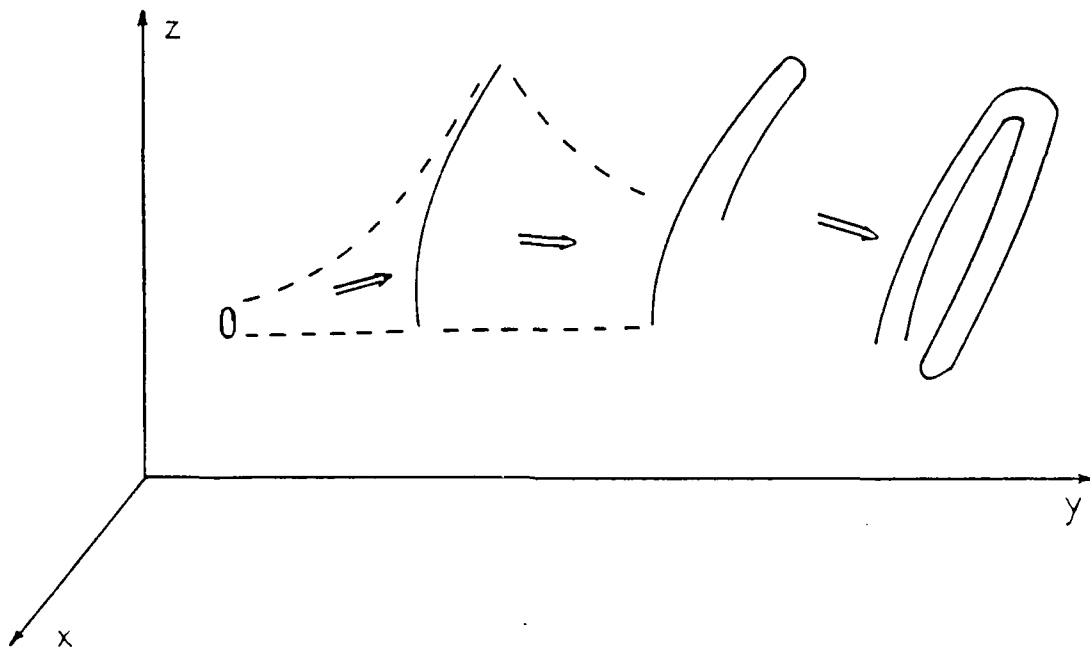


Figure 6-20. Formation of a Strange Attractor. Start with a disk which represents trajectories very close to each other. The trajectories are traveling in the 'y' direction. They diverge chaotically in the 'z' direction, but converge in the 'x' direction. The 2-D disk collapses to a 1-D line. Since the system is bounded, the trajectories can not diverge exponentially forever in the 'y' direction. They fold over. This folding process continues resulting in the formation of an strange attractor as shown on the right.

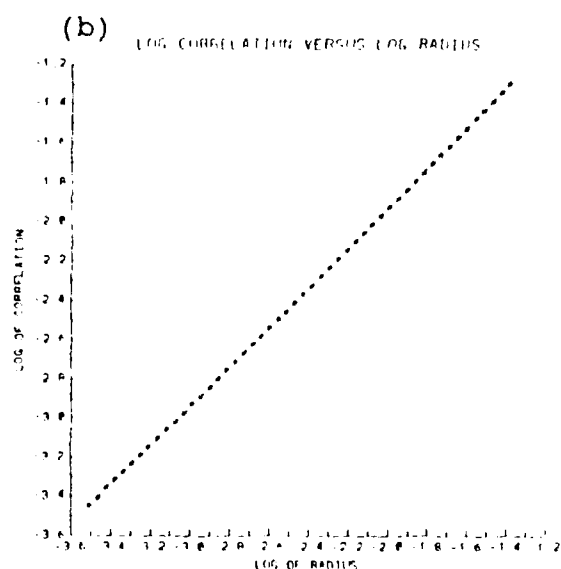
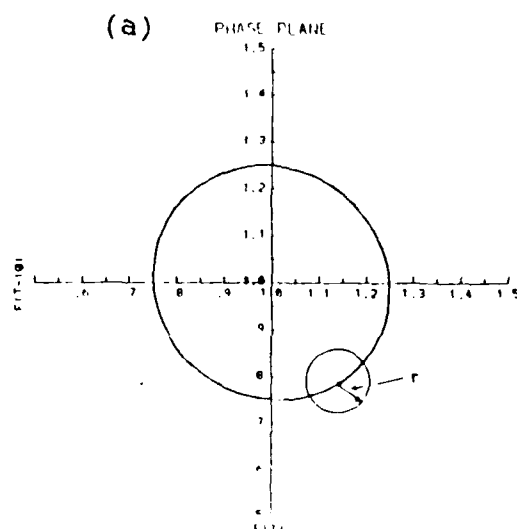


Figure 6-21. Computation of Fractal (Correlation) Dimension. 32 hertz signal used as an example. (a) Draw a circle of radius ' r ', centered about an arbitrary point on the attractor. Remember the signal was digitized. Determine number of digitized points inside the circle. Call this number "correlation." (b) Repeat for many radius and for many arbitrary points. Plot log correlation versus log radius. Slope is fractal dimension. In this case, 1.

Dependence of Fractal Dimension on Phase Space Dimension

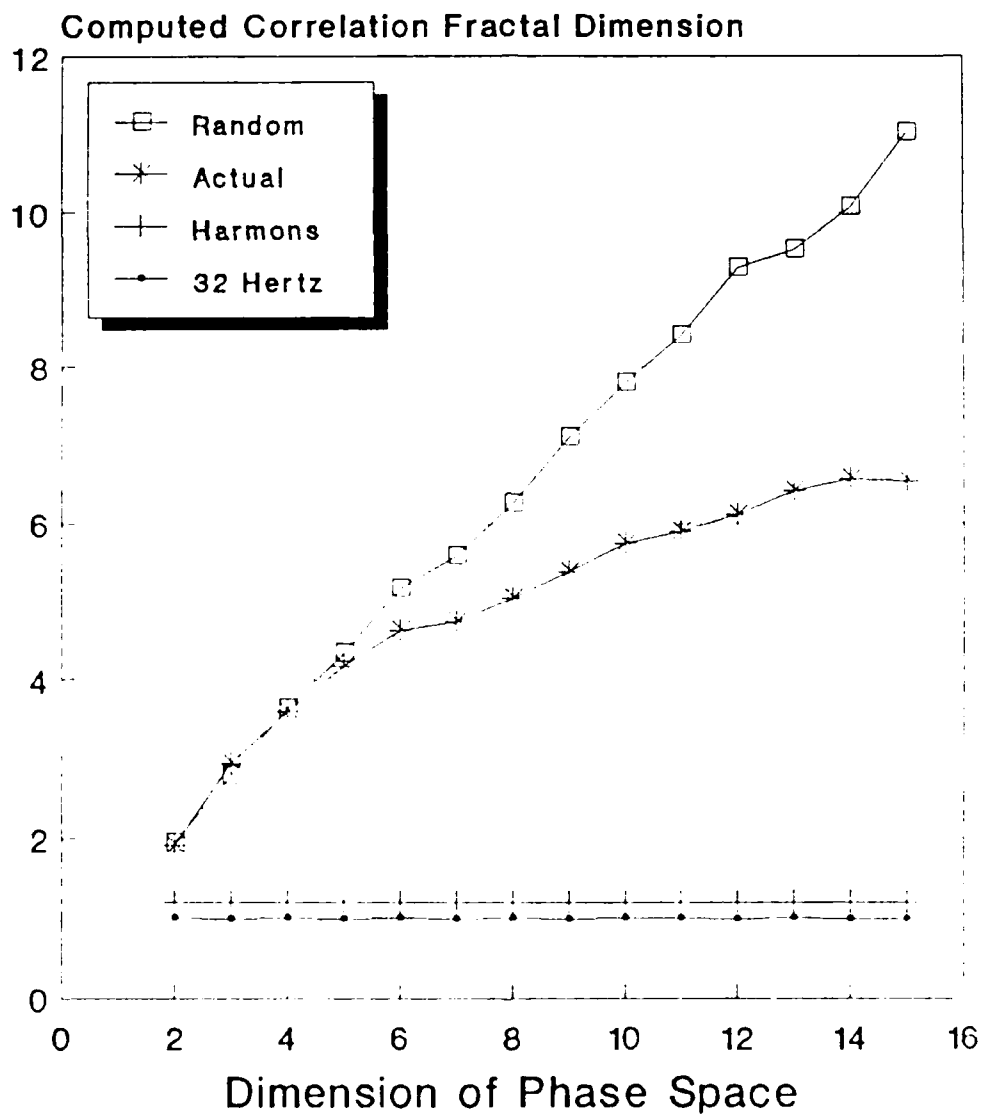


Figure 6-22. Fractal Dimension. Plot of fractal dimension versus dimension of phase space. Results for the 32 hertz, Harmons, Actual, and Random sample presented.

VII. NATURE OF THE HHC CONTROLLER TRANSFER MATRIX

A. PURPOSE

This chapter shows how the transfer matrix in the HHC control law is either linear and repeatable or non-linear and non-repeatable depending on how vibrations are defined.

B. TRANSFER MATRIX

The HHC control law from the third chapter is repeated here:

$$z = z_0 + Tu \quad (3.1)$$

All closed loop controlled HHC wind tunnel and flight tests to date have used this control law. The question unanswered by present research is whether the transfer matrix, 'T', is either linear or nonlinear. Also, whether it is either repeatable or non-repeatable.

'T' is repeatable if the values for all 36 elements of the matrix remain the same each time they are measured under similar flight conditions. It is non-repeatable if the 36 elements of the matrix change significantly each time an estimate is made for the matrix, even though test flight conditions, such as airspeed, do not change.

If 'T' is repeatable, then the question remains whether it may be treated as linear or non-linear. 'T' is linear if small changes in test conditions result in small changes in the values of its elements. For example, if 'T' is linear, the values of 'T' measured at 70 knots should lie between the values of 'T' measured at 60 and 80 knots.

The 'z' and 'z₀' vectors have six elements each. These elements represent the cosine and sine components of lateral, vertical and longitudinal accelerations at a single frequency and are in units of "g's". These vectors represent vibrations at a specific location on the helicopter. For the OH-6A, the frequency was at 32 hertz and the location was underneath the pilot's seat.

The 36 elements of the 'T' matrix relate swashplate excitation to the resulting helicopter vibration. Each element in the 'T' matrix is in units of the 'z' vector divided by units of the 'u' vector. In the case of the OH-6A, the units for the 'T' matrix were "g's/inches".

C. SIGNIFICANCE OF POINCARÉ SECTION AND VAN DER POL PLANE

A qualitative relationship exists between the 'z' vectors and trajectories drawn in toroidal phase space. To visualize this, vertical vibrations are considered. The trajectory of vertical vibration is drawn in toroidal

phase space with the plotting rate at the 'z' vector frequency, namely 32 hertz. The single attractor obtained represents two vertical vibration elements of the 'z' vectors. Taking a Poincare section (PS), or forming a Van der Pol (VDP) plane from this attractor reveals details of the relationship. With appropriate scaling, the horizontal location of the attractor in either the PS or VDP plane gives the cosine part of the vertical vibration. The vertical location of the attractor, again with appropriate scaling, is identified as the sine part of vertical vibration. Further, in both the PS and the VDP plane, amplitude of vibration is the distance from the origin to the location of the attractor. Phase is given by the angular measure from an arbitrary axis.

Three PS or VDP planes, one each for lateral, vertical and longitudinal vibration respectively, describes the 'z' vectors fully. With HHC off, the PS or VDP plane represents the 'z₀' vector, or the baseline response. With HHC on, the PS or VDP plane represents the 'z' vector, or the new system response.

The HHC control law assumes a linear static transfer relationship (matrix 'T') between the commanded swashplate movement (vector 'u') and the fuselage vibrations (vectors 'z'). If the 'z' vectors are linear and repeatable then the 'T' matrix is linear and

repeatable owing to this linear relationship in the control law. If the 'z' vectors are non-linear and non-repeatable, then the 'T' matrix is non-linear and non-repeatable. For given test data and flight conditions, the nature of the 'T' matrix can be deduced from the nature of 'z' and 'z₀' vectors.

D. COMPARISON OF TWO METHODS OF PLOTTING

Consider the effects of two methods of plotting about the torus. The plotting rate may either be at a constant rate or at a rate synchronized with that of the rotor of the helicopter. Figure 7-1 illustrates these two methods of plotting using a vertical acceleration signal from under the pilot's seat at an airspeed of 60 knots and with the HHC system off. Plotting about the torus is at a fixed frequency of 32.36 Hertz in part (a). This method is referred to as plotting in the "clock time domain."

Plotting is synchronized with the main rotor in part (b). In part (b), the trajectory goes exactly 4 times around the torus for each revolution of the helicopter rotor. The second method is referred to as plotting in the "rotor time domain" and the plotting rate in this case is 4P.

Figure 7-2 presents the PS of Figure 7-1 at 270 degrees azimuth. The location of this PS is shown in

Figure 7-1(b). The novel method of presentation shown in Figure 7-2 is believed to be new. The number '0' marks the first half seconds duration of trajectories which intersect the PS. The number '1' marks the next half seconds duration of intersections, the number '2' the next half seconds duration, and so on - through to the number '9'. Plotting at a fixed 32.36 Hertz rate, part (a), causes the trajectories to first intersect the PS near the positive x axis. They then move toward the negative y axis and then pass by the negative x axis and end finally near the positive y axis. Plotting at a 4P rate, part (b), causes all of the trajectories to intersect the PS near the positive x axis. Observe that the trajectories form a well defined attractor when plotting in the "rotor time domain."

In order to interpret the data in Figures 7-1 and 7-2 refer to the Figure 4-3. This figure presents the main rotor rpm for the same flight test point. The rotational rate of the main rotor varies by an average of 1 to 2 %. This slight variation in rotor rotational rate accounts for the difference in the two presentations. (Note: The main rotor azimuth pipper was used to synchronize the plots to the rotor time domain. Main rotor rpm was not used due to large amounts of quantization errors in that signal.)

Figure 7-3 and 7-4 present the lateral and longitudinal vibrations under the pilot's seat using both methods of plotting. They look similar to Figures 7-1 and 7-2.

E. IMPLICATIONS

Defining the 'z' vectors in the rotor time domain results in a vector whose elements (sine and cosine components) remain unchanged at one condition of flight. The 'T' matrix, then, is predictable and steady. In contrast defining the 'z' vectors at a fixed frequency (clock time domain) yields unpredictably in elements that change with time. The 'T' matrix, then, is unpredictable, even though conditions of flight do not change.

Figures 7-1 through 7-4 highlight the importance of defining the HHC control law, equation (3.1), in the rotor time domain. From a practical standpoint, constant rotor rpm should be carefully maintained. More importantly, the HHC actuators MUST move in synchronization with the main rotor. The HHC computer must have accurate information on main rotor azimuth position through a reliable pipper system.

F. CONCLUSION

The next two chapters will show that the 'T' matrix changes in a predictable and linear fashion as both HHC controller inputs and helicopter airspeed changes. The HHC control law transfer matrix is both linear and repeatable if the vibrations, 'z', are defined in the rotor time domain. This matrix is non-linear and non-repeatable if vibrations are defined in the clock time domain.

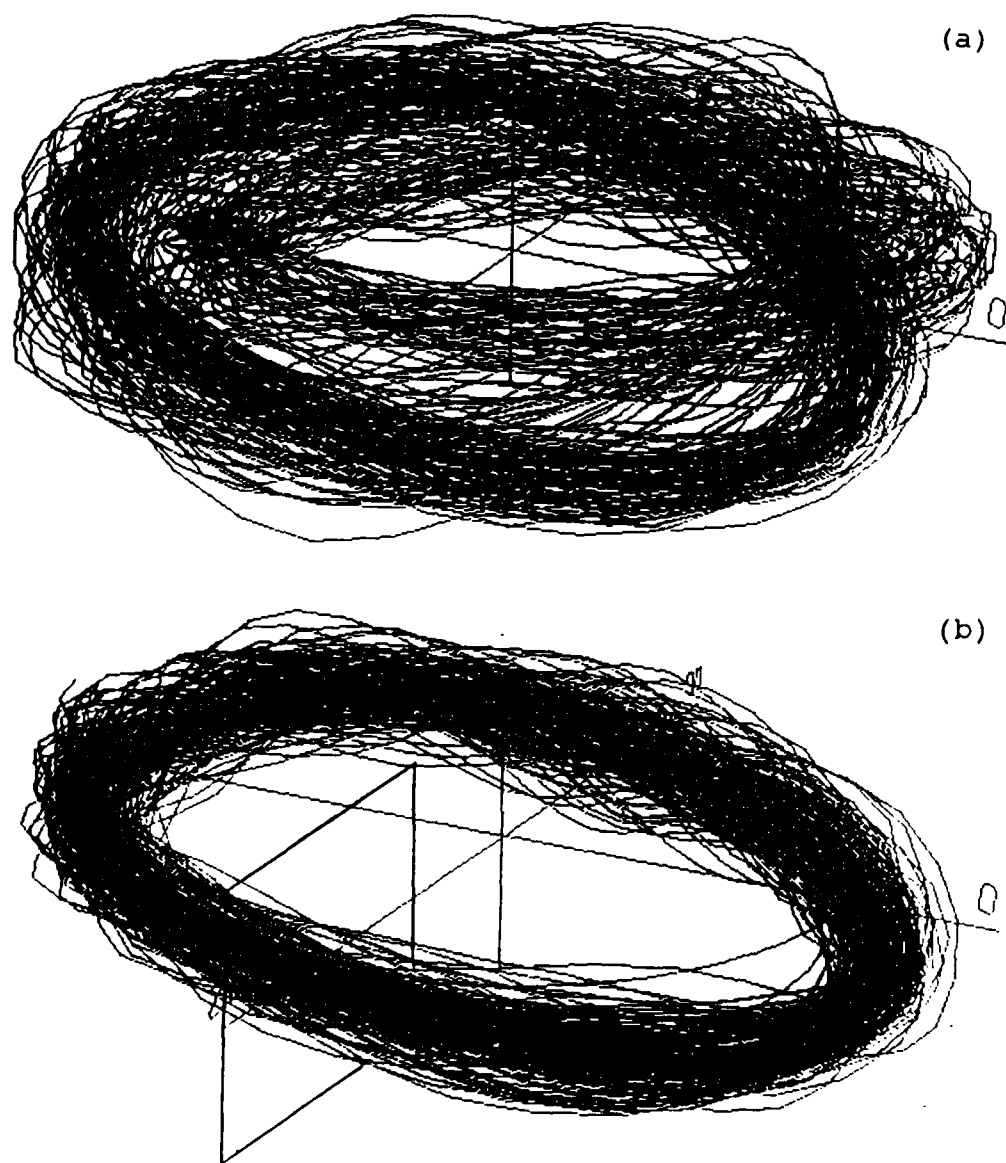


Figure 7-1. Two Methods of Plotting a Signal in Toroidal Phase Space. (a) Rate of plotting held fixed at 32.36 hertz. (b) Rate of plotting held at the 4P frequency, as the rotor's rotational rate varies the plotting rate varies. This is referred to as plotting in the rotor time domain. Presented is vertical acceleration under the pilot's seat at 60 knots airspeed with the HHC system off.

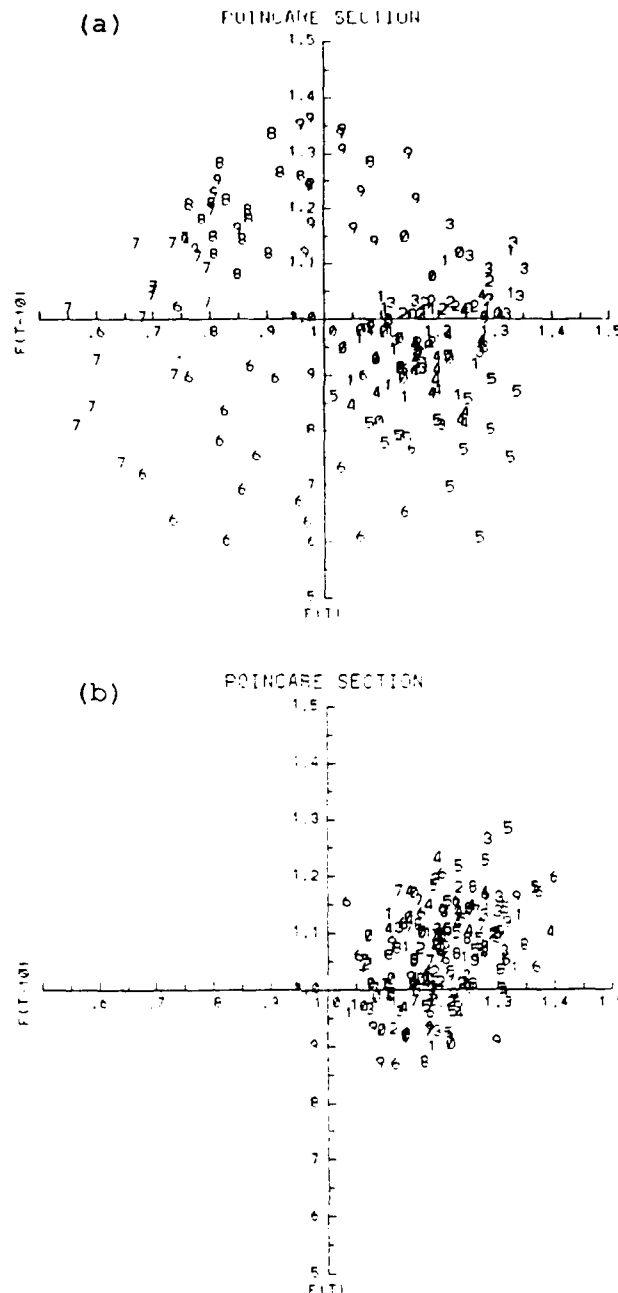


Figure 7-2. Poincare sections of figure 7-1. Numbers indicate when the intersection of trajectories intersection with the Poincare plane occurred. 'Zeros' indicate intersection in the first half second, 'Ones' indicate in the second half second, and so on, with 'Nines' indicating the last half second. Presented is vertical acceleration under the pilot's seat at 60 knots airspeed with the HHC system off. Embedding time is 10 samples and section is taken at 270 degrees azimuth. (a) 32.36 hertz plotting rate. (b) 4P frequency plotting rate.

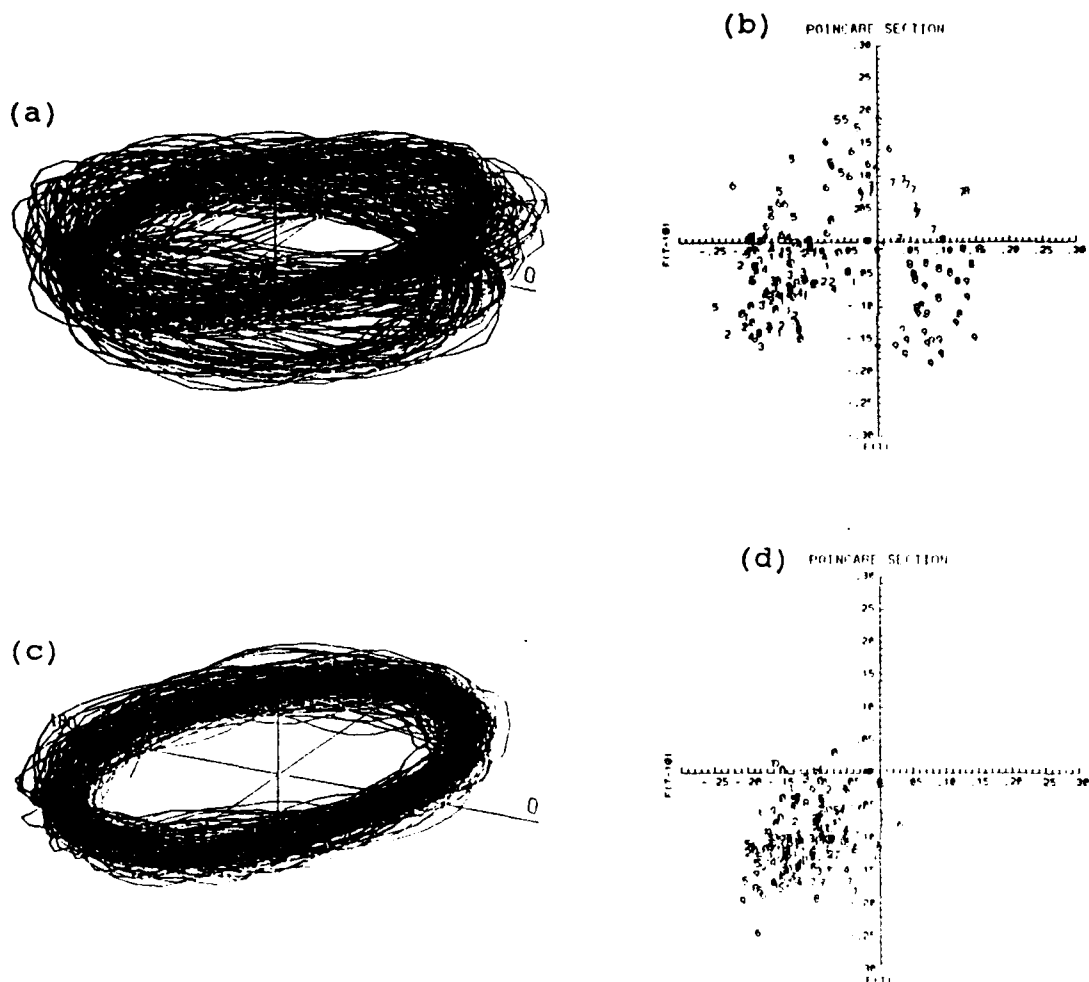


Figure 7-3. Lateral Acceleration. Presented is lateral acceleration under the pilot's seat at 60 knots airspeed with the HHC system off. Embedding time is 10 samples and Poincare section is taken at 270 degrees azimuth.

- (a) Torus at 32.36 hertz plotting rate.
- (b) Poincare section of (a).
- (c) Torus at 4P frequency plotting rate.
- (d) Poincare section of (c).

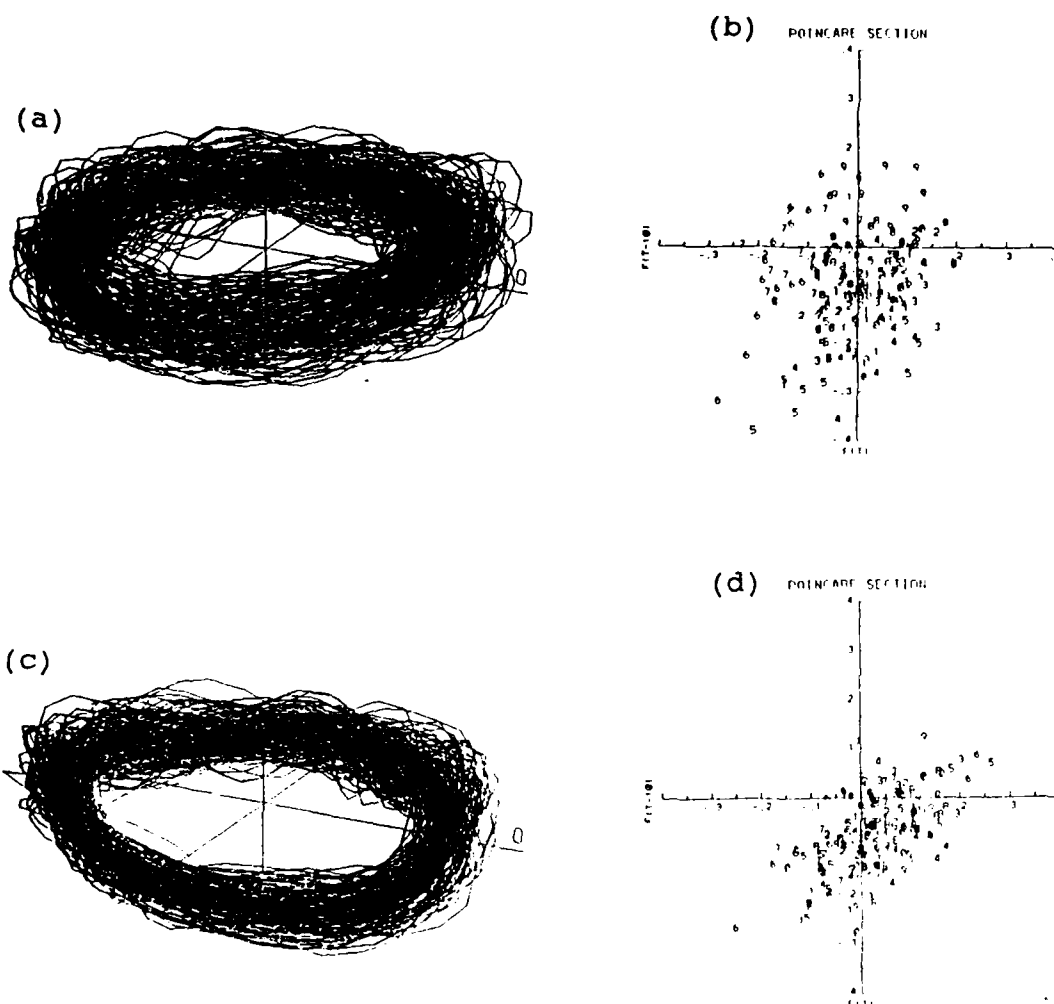


Figure 7-4. Longitudinal Acceleration. Presented is longitudinal acceleration under the pilot's seat at 60 knots airspeed with the HHC system off. Embedding time is 10 samples and Poincare section is taken at 270 degrees azimuth.

- (a) Torus at 32.36 hertz plotting rate.
- (b) Poincare section of (a).
- (c) Torus at 4P frequency plotting rate.
- (d) Poincare section of (c).

VIII. LIMITS OF HHC PERFORMANCE

A. PURPOSE

Chapter 10 demonstrates a limit exists to HHC vibration reduction. This is attributed to the presence of chaos. A new technique, explained in this chapter, allows easy determination of this limit. The method described here does not require the aircraft to be equipped with HHC.

B. EFFECTS OF HHC

HHC attempts to reduce a measured variable, usually, the vibrations under the pilot's seat. Figure 8-1 illustrates the effect of 0.33 degree lateral excitation of the swashplate on the 4P vertical and lateral vibrations under the pilot's seat. Presented are 14 flight test points for manual controller phases of 0 to 360 degrees, in 30 degree increments. The aircraft is in steady level flight at 60 knots. This figure shows the effect of HHC on amplitude of response vibration only. The horizontal axis shows manual controller phase. This is the phase of swashplate excitation relative to rotor blade azimuth position. A zero degree controller phase means that the swashplate tilts to the port (left) when the four rotor blades are at 0, 90, 180

and 270 degrees rotor azimuth respectively. A 180 degree controller phase means the swashplate tilts to the starboard (right) when the four rotor blades are at 45, 135, 225 and 315 degree rotor azimuth respectively. Further, 360 degrees of manual controller phase relates only to 90 degrees of rotor azimuth. Tilting of the swashplate occurs 4 times for each rotor revolution. This relationship was determined by comparing main rotor azimuth pipper information with HHC actuator position information.

Figure 8-2 presents the Poincare sections (PS) of the same vertical vibration data in Figure 8-1, but plotted in toroidal phase space. The plotting rate is at 4P; and, the PS's are at 180 degrees azimuth.

Figure 8-3 presents the Van der Pol (VDP) plane for the vertical vibrations. The rate of untwisting is also set at 4P. Helicopter fuselage vibrations contain a single predominant frequency, hence the VDP method works.

The effect of HHC is to move the attractor, in both the PS and VDP plane, WITHOUT changing its size. The attractor is bounded to a small volume of the phase space. Although predictability of the trajectories within the attractor is not possible, the overall attractor location is fixed for each controller phase.

As the manual controller phase changes, the attractor shifts its position in the plane.

Minimum vibration is seen to occur at 300 degree manual controller phase. The attractor location is roughly centered about the origin. The distance of the attractor from the origin of the plot is an indication of the amplitude of vibration. The closer to the origin, less is the vibration.

Maximum vibration is observed at 90 degrees manual controller phase. The attractor is at the greatest distance from the origin, indicating greater vibration.

C. PHASE DETERMINATION

One of the principal advantages of the PS and VDP plane presentations is that they display amplitude and phase of the response simultaneously. The distance from the origin gives the amplitude while the clock position about the origin indicates the response phase.

The attractor appears to move linearly with changes in manual controller phase in both the PS and the VDP plane. In both representations, HHC acts as a vector which moves the attractor from its baseline position. This vector is referred here as the "HHC vector." Recall that both the PS and VDP plane are constructed in pseudo phase space. The orientation of the HHC vector for each manual controller phase in the PS or VDP plane

is revealed by inspection. Observing the attractor position at several manual controller phases fixes a coordinate axis for the HHC vector. Presented in both Figures 8-2 and 8-3 is a "HHC coordinate axis" for this particular aircraft. It shows the direction in which the baseline vibration attractor will move as HHC is applied at various controller phase angles.

Once established, the HHC coordinate axis does not change for different flight conditions, such as airspeed or sideslip. However, changes in embedding time will change the orientation of the HHC coordinate axis. Generally during all the flight tests, only one choice of embedding time is used in the construction of the pseudo phase space. Also the HHC coordinate axis may change for the other two swashplate excitation modes, namely collective and longitudinal. Flight test data for these two modes were not available. Finally, note that only two HHC manual controller phase data samples are needed to fix the HHC coordinate axis for a given aircraft for one mode of swashplate excitation.

Given the HHC coordinate axis and one baseline vibration sample, best phase for HHC may be read directly from the PS or VDP plane. This is a significant feature of these methods. Only one baseline data sample at each test condition gives the phase for best HHC vibration reduction.

D. LINEAR MOVEMENT OF THE ATTRACTOR AND THE TRANSFER MATRIX

The attractor appears to move linearly with changes in manual controller phase. For example, the position of the attractor position at 30 degree controller phase can be interpolated from the attractors at 0 and 60 degrees controller phase respectively. This implies that the HHC vector movement is linear.

This linear attractor movement means that the transfer matrix, 'T', changes little with HHC swashplate inputs. Hence, the transfer matrix appears to be predictable and repeatable for this aircraft.

E. LIMIT OF HHC PERFORMANCE

Consider Figures 8-4 and 8-5, which are the VDP representations of lateral and vertical vibration at the pilot's seat. Figure 8-6 presents the flight test points considered. Both Figures 8-4 and 8-5 present baseline response in the left column and HHC-On response in the right column. The first row is vertical vibration and the second row is lateral vibration. The longitudinal vibration is not available because of improper signal conditioning of that signal during the flight test.

Figure 8-4 compares baseline with Open Loop HHC. Note that with HHC-On, the attractors are not exactly at

the origin of the phase plane. This implies that the vibration was not reduced to a minimum. The HHC moves the attractor in the VDP plane without changing its size.

A comparison of baseline with Closed Loop HHC is given in Figure 8-5. Figure 8-6 shows that this is the best reduction achieved with HHC in the entire flight test program. The best HHC performance is with simultaneous longitudinal, lateral and collective swashplate excitation in an optimal combination. The attractor is roughly centered at the origin of the phase plane showing that the HHC system reduced the vibration to the minimum possible. The size of the attractor remains unchanged as compared to the baseline case.

The size of the attractors may be viewed as a limit of HHC vibration reduction. The size appears to be independent of improved controllers, actuators, computers, etc. and therefore, vibration level may not be reduced any further. In order to determine the best HHC performance, only one sample of baseline (HHC off) data of the measured variable is needed. In other words, maximum vibration reduction obtainable from a given HHC system may be known before turning on that system or even installing it. This knowledge allows a significant reduction in the time required to determine controller characteristics and HHC performance levels.

This further avoids wasted resources in trying to accomplish vibration reduction beyond the limit indicated in baseline flight testing. Remember that with appropriate scaling, the area enclosed by the trajectories is a measure of the vibratory energy in a signal.

Furthermore, since both the PS and VDP plane show amplitude and phase of a vibration at a single frequency, these methods can monitor the performance of a HHC system during flight test. Unlike Fourier analysis, these methods can be implemented real time since all that is required is the observable and a time delayed 'fake' observable.

F. SUMMARY

The Poincare section and Van der Pol plane methods will reduce flight test requirements by showing limits of HHC performance. They also allow rapid determination of best phase for HHC controller and rapid determination of maximum vibration reduction achievable for a given aircraft.

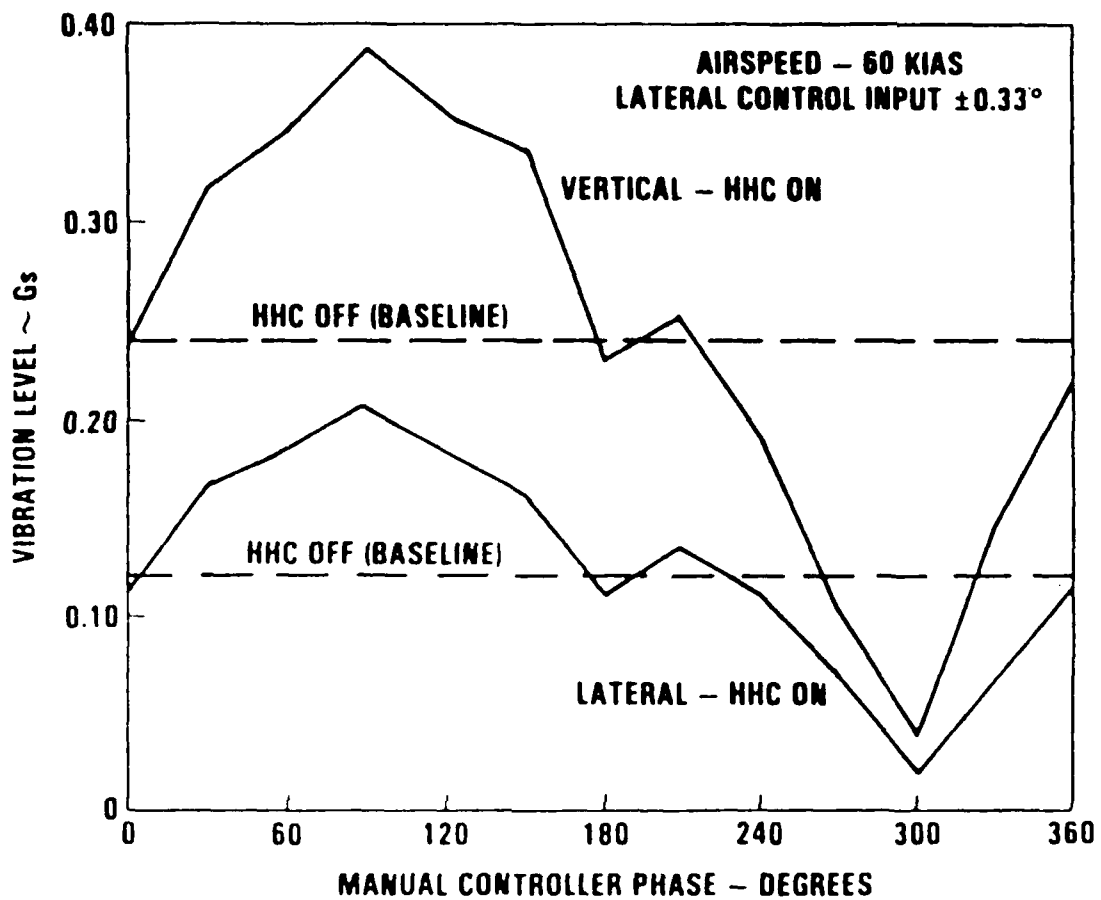


Figure 8-1. Variation of HHC Performance with Controller Input Phase. Conditions are level flight at 60 knots with 0.33 degrees of lateral 4P excitation of the swashplate. [from Wood et al. (1985), reprinted with permission of author].

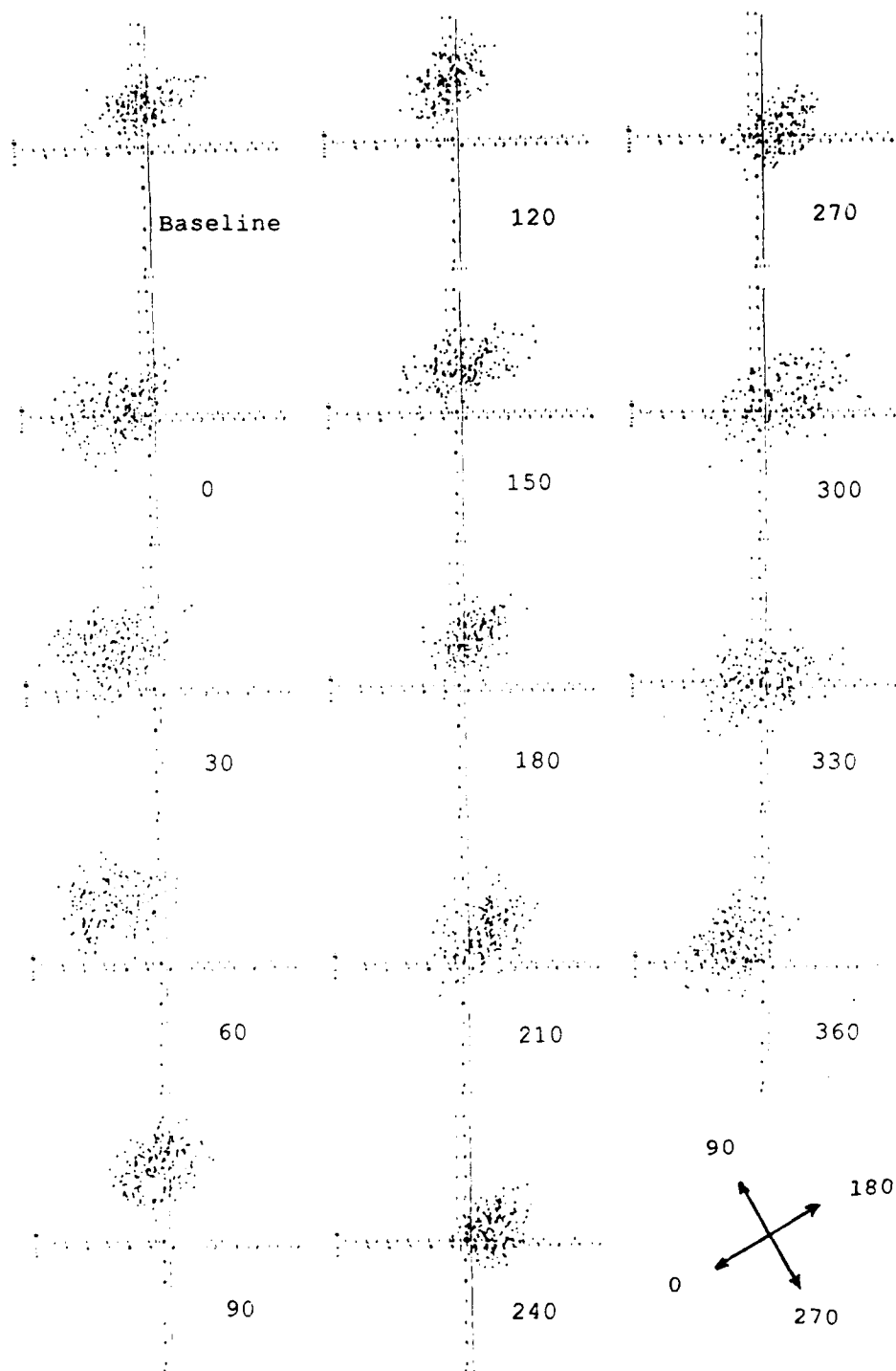


Figure 8-2. Poincare Sections for Phase Sweep of Lateral Mode. Poincare section of toroidal phase space with section taken at 180 degree azimuth and rate of plotting is at 4P. Conditions are level flight at 60 knots with 0.33 degrees of lateral 4P excitation of swashplate. The manual controller phase is indicated on each section. Embedding time is 10 samples.

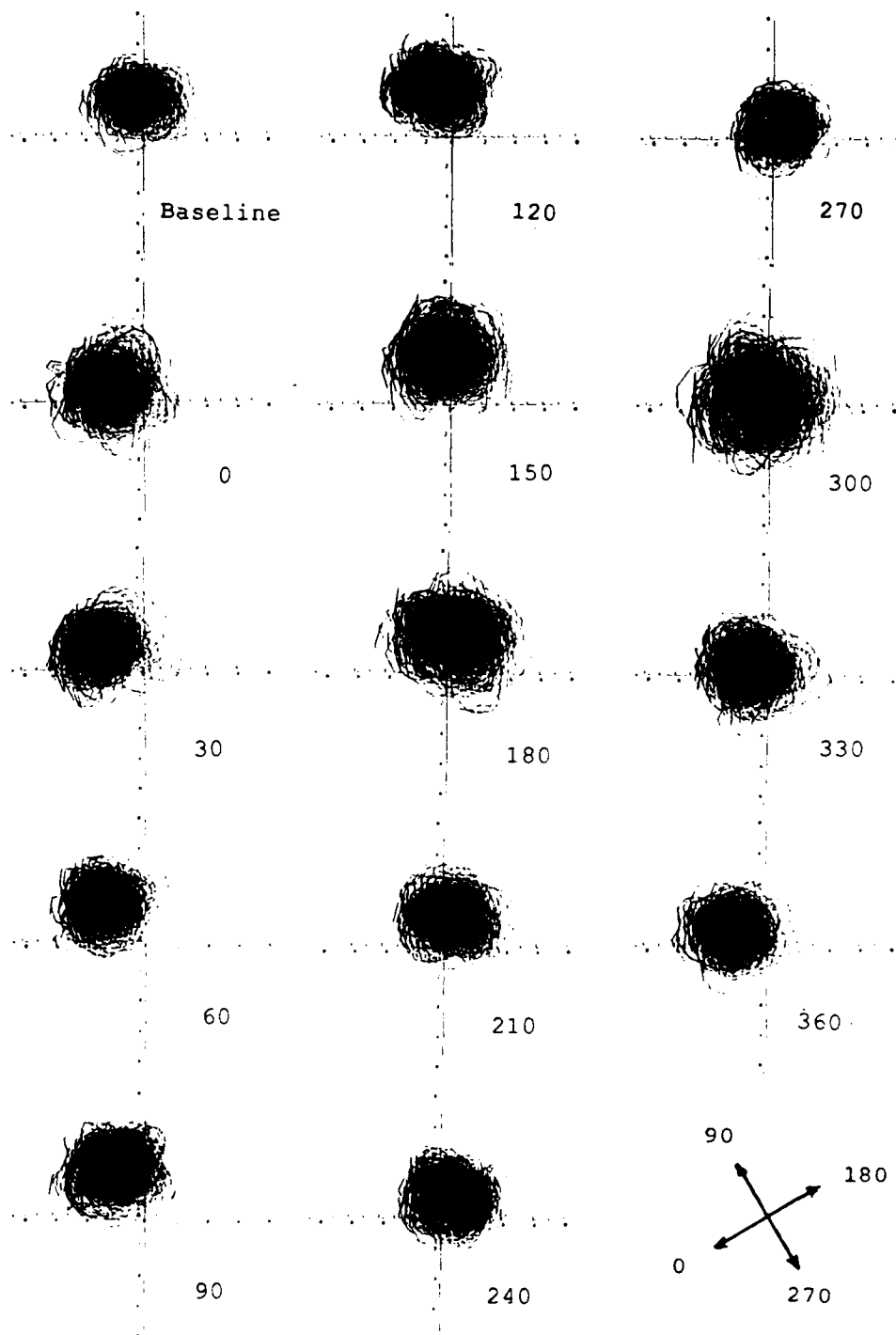


Figure 8-3. Van der Pol Planes for Phase Sweep of Lateral Mode. Conditions are level flight at 60 knots with 0.33 degrees of lateral 4P excitation of swashplate. The manual controller phase is indicated on each plane. Rate of untwisting is 4P for the Van der Pol plane. Embedding time is 10 samples.

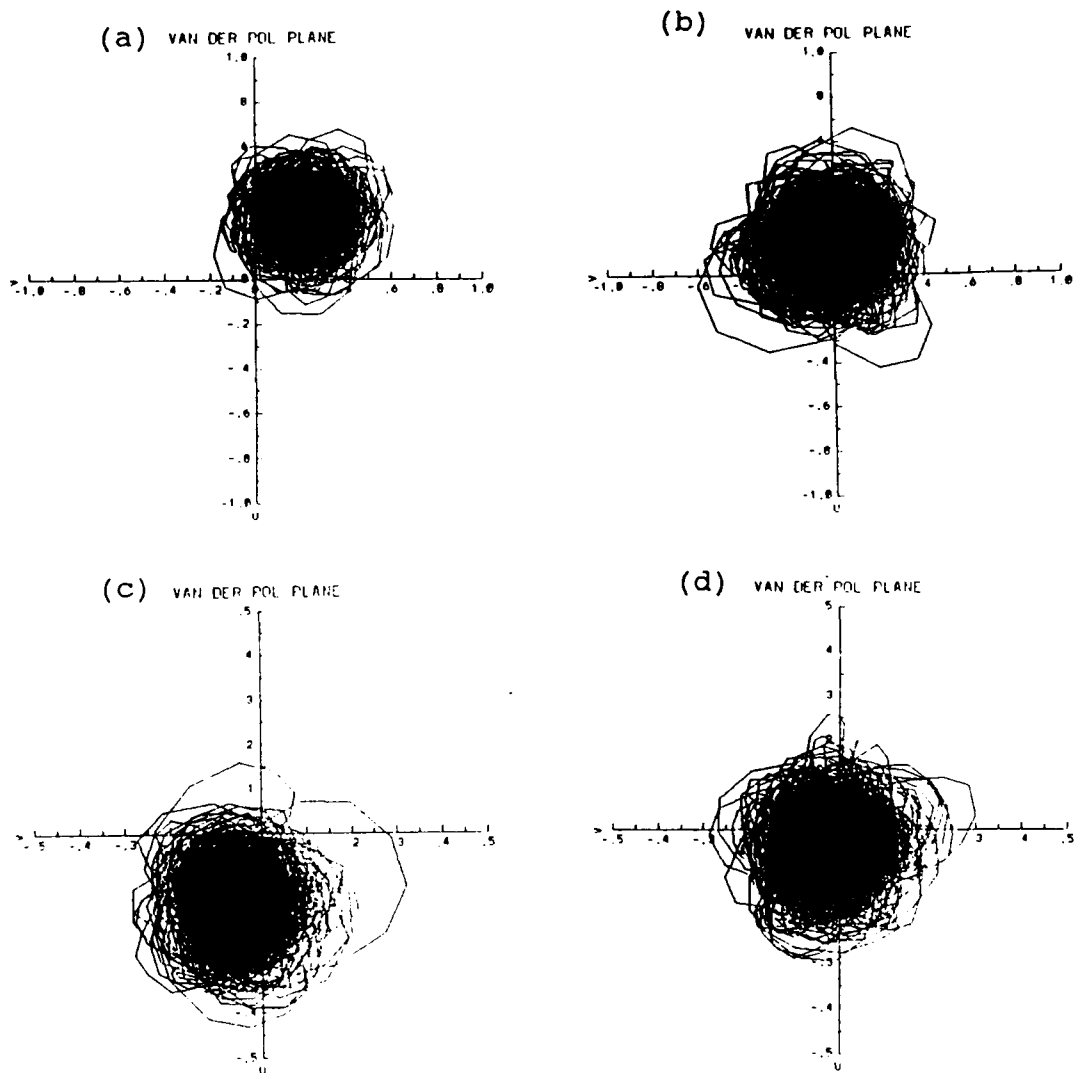


Figure 8-4. Comparison of Van der Pol planes with Open Loop Control of HHC. Conditions are level flight at 100 knots. For HHC On the conditions are 0.33 degrees of lateral 4P excitation of swashplate at 270 degrees of controller phase. Rate of untwisting is 4P for all Van der Pol planes. Embedding time is 10 samples.

- (a) Vertical acceleration with HHC off.
- (b) Vertical acceleration with HHC on.
- (c) Lateral acceleration with HHC off.
- (d) Lateral acceleration with HHC on.

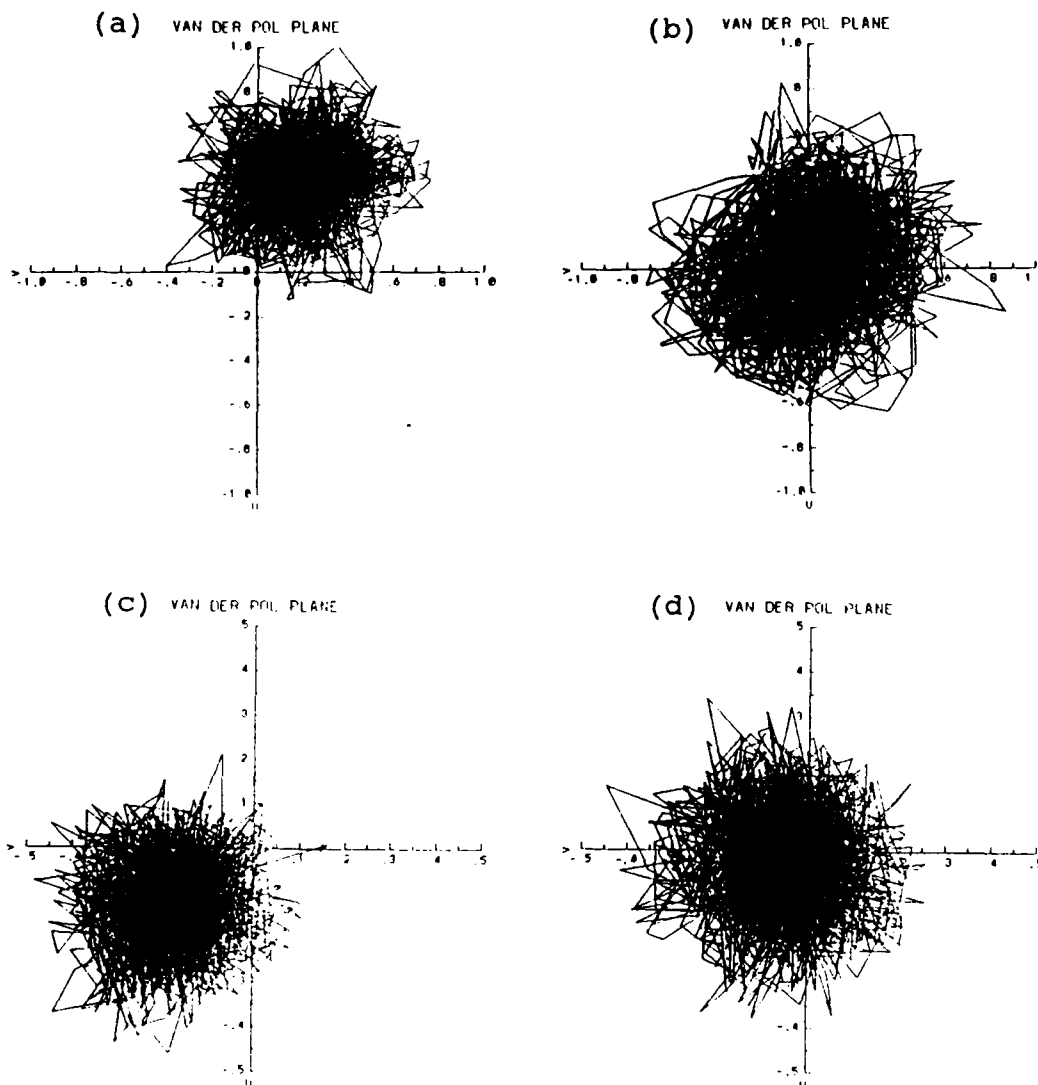


Figure 8-5. Comparison of Van der Pol planes with Closed Loop Control of HHC. Conditions are level flight at 100 knots. Rate of untwisting is $4P$ for all Van der Pol planes. Embedding time is 10 samples.

- (a) Vertical acceleration with HHC off.
- (b) Vertical acceleration with HHC on.
- (c) Lateral acceleration with HHC off.
- (d) Lateral acceleration with HHC on.

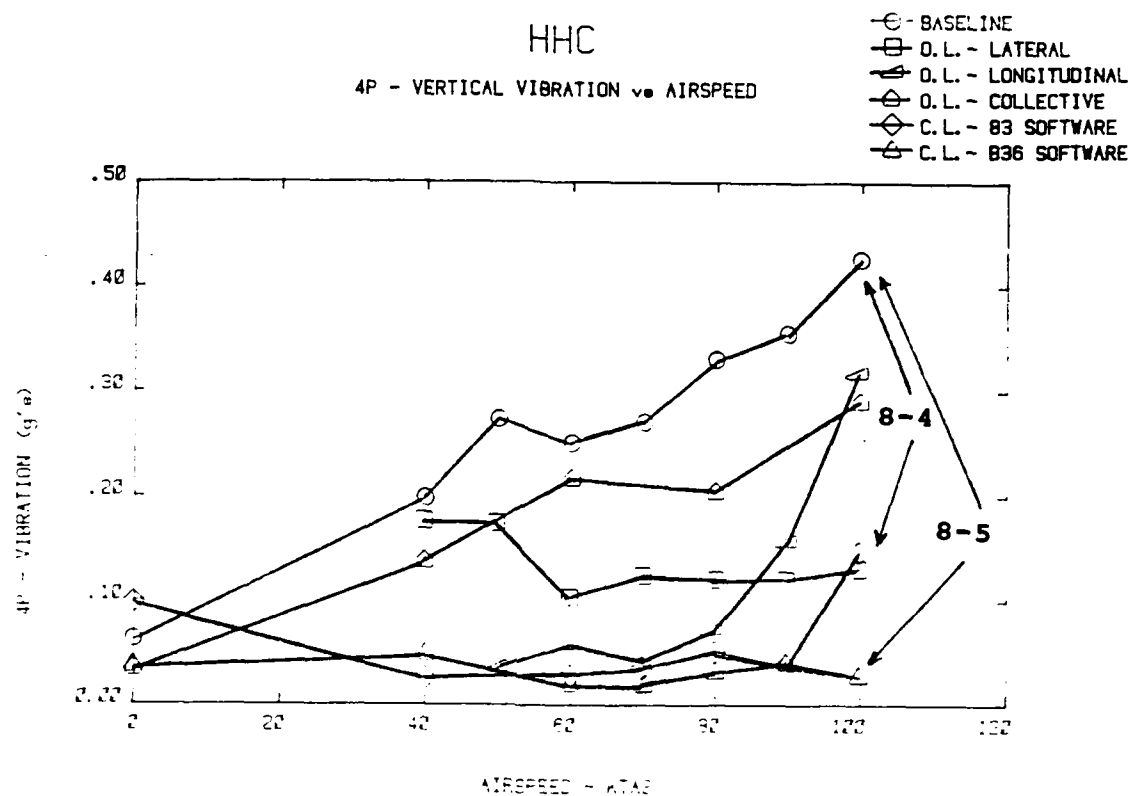


Figure 8-6. Flight Test Points compared in Figures 8-4 and 8-5. In Figure 8-4 comparison was with lateral mode at 100 knots versus baseline at 100 knots. In Figure 8-5 comparison was with closed loop B36 software with baseline at 100 knots [drawn by McDonnell Douglas Helicopter Company, reprinted with permission].

IX. HHC CONTROLLERS

A. PURPOSE

A new technique to determine the minimum HHC controller requirement for any helicopter from a few minutes duration of flight test data is described. For the OH-6A, a scheduled gain controller is shown adequate for steady level flight. This new method does not need the HHC system installed on the aircraft.

B. REVIEW ON TYPES OF CONTROL SYSTEM

The characteristics of the 'T' matrix and its changes with flight conditions determine the minimum control system needed for a HHC system. If the 'T' matrix is repeatable and does not change with flight conditions, then a fixed gain control system is seen to be adequate. A fixed gain control system uses only one set of values for the elements of the 'T' matrix for all flight conditions. This system represents an open loop system where identification of the 'T' matrix is done off line. This is a very simple control system.

If the 'T' matrix is repeatable and linear, but changes with flight conditions, then a scheduled gain control system is adequate. In a scheduled gain control system, the 'T' matrix changes as some measured variable

such as airspeed, changes. This system results in a closed loop with identification of the 'T' matrix being done off line. The requirement for sensors to measure the input variables like airspeed, sideslip, etc. make this system more complex than the fixed gain system.

If the 'T' matrix is either non-repeatable or non-linear, then an adaptive gain control system is required. This system is closed loop and uses on line identification of the 'T' matrix. The resulting control system is the most complicated system, and sometimes being unstable, it can easily increase vibrations instead of decreasing them.

C. DETERMINATION OF MINIMUM CONTROLLER FROM FLIGHT TEST

The previous two chapters demonstrated that the transfer matrix, 'T', is repeatable when measured under similar flight conditions. Also, the matrix changes little with changes in swashplate excitation.

Figures 9-1 and 9-2 present acceleration data measured underneath the pilot's seat. The left column in each figure represents vertical acceleration, while the right column gives lateral acceleration. These figures show baseline (HHC off) data from 60 to 100 knots at 10 knot increments. Figure 9-1 presents the PS of the vibration data, plotted in toroidal phase space. The plotting rate is selected as 4P and, the PS are at 180

degrees azimuth. Figure 9-2 presents the VDP plane for these same vibrations. The rate of untwisting for the VDP plane is also set at 4P.

Both of these presentations display amplitude and phase simultaneously. Observe that as airspeed changes from 60 knots (top row of both figures) to 100 knots (bottom row of both figures), the amplitude and phase of the response changes predictably and linearly.

A scheduled gain controller with only two or three transfer matrices can accommodate the changes shown in the response. Conversely, for changes of airspeed limited to 20 knots, a fixed gain controller seems adequate.

This technique was not evaluated on maneuvering flight data, as this data was not available. Also longitudinal vibration data was not analyzed, as signal conditioning problems gave bad data.

D. FUTURE APPLICATION OF CHAOS METHODS ON HHC

The present method yields rapid determination of proper HHC controller type for other helicopters. The recommendation is to use the PS or VDP plane methods in real time during a few minutes of maneuvering flight. The controller type can be selected by observing the movement of the attractor of a measured variable, such as vertical, lateral, and longitudinal vibration. This

method, as can be seen, does not need the HHC system to be installed in the aircraft.

E. SUMMARY

A method is described which allows rapid determination of proper controller type for any helicopter. For the OH-6A, a scheduled gain controller for HHC appears to be adequate for steady level flight.

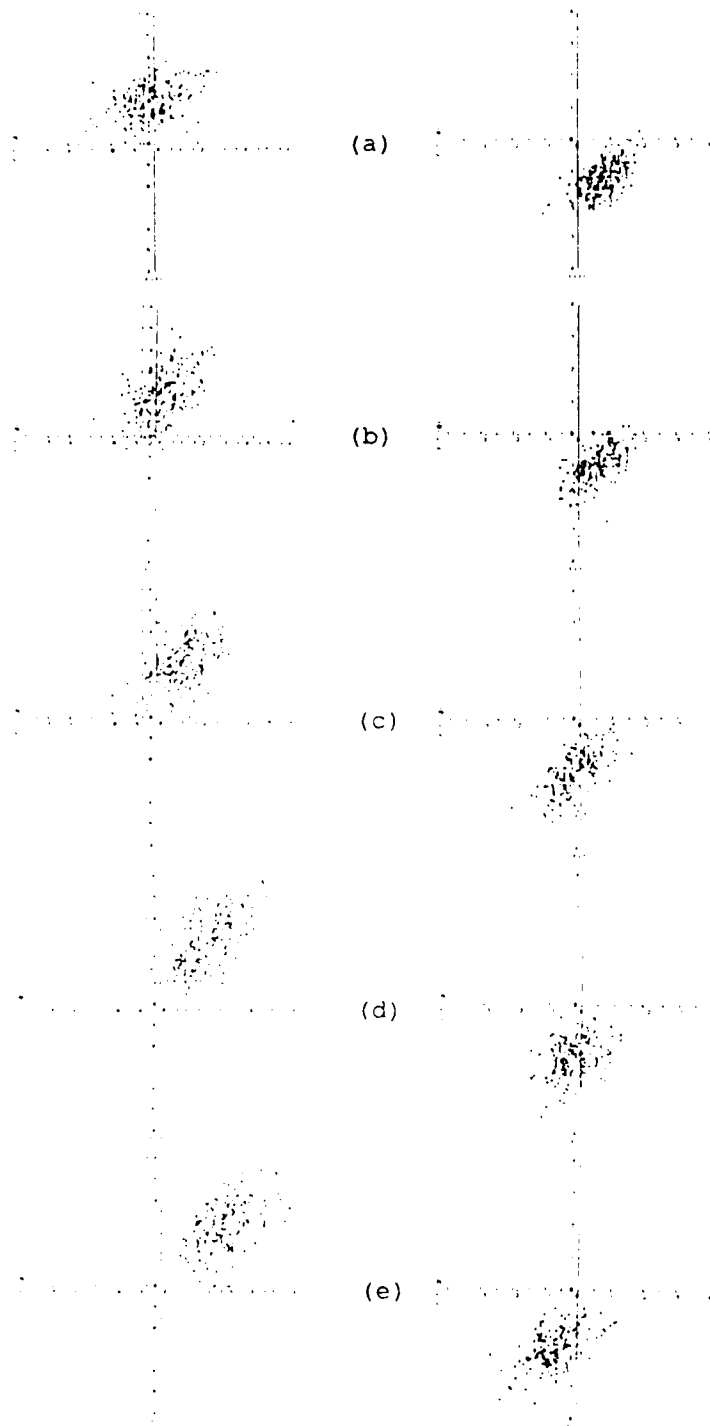


Figure 9-1. Poincare Sections of Pilot Seat Acceleration Versus Airspeed. Conditions are level flight with HHC off. Rate of plotting around the toroidal phase space is 4P and the sections are at 180 degree azimuth. Left column is vertical acceleration and right column is lateral acceleration. (a) 60 knots. (b) 70 knots. (c) 80 knots. (d) 90 knots. (e) 100 knots.

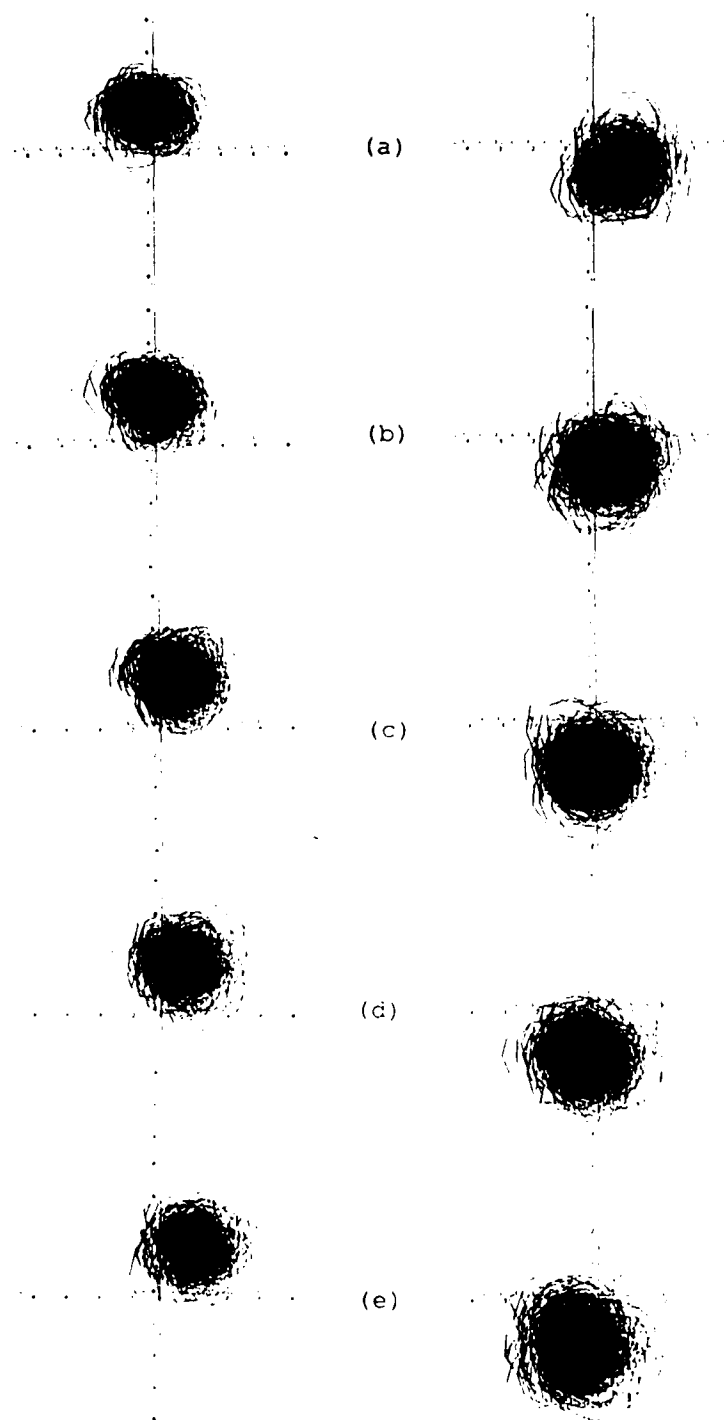


Figure 9-2. Van der Pol plane representations of Pilot Seat Acceleration Versus Airspeed. Conditions are level flight with HHC off. Rate of untwisting the plane is 4P. Left column is vertical acceleration and right column is lateral acceleration. (a) 60 knots. (b) 70 knots. (c) 80 knots. (d) 90 knots. (e) 100 knots.

X. THE HUNT FOR CHAOTIC HELICOPTER VIBRATIONS

A. PURPOSE

This chapter is devoted to the in-depth study of flight test measurements obtained from the OH-6A helicopter using the dynamical concepts described in Chapter 6. Classical methods of analysis are also employed. The purpose of this investigation is to explore helicopter vibrations for chaos. Historically, helicopter vibrations are assumed to be periodic. Understanding the nature of helicopter vibrations may lead to better methods of vibration reduction and better design of vibration controllers.

Also, the classification of helicopter vibrations has important repercussions in helicopter simulations. The numerical simulation programs like CAMRAD and RACAP assume that helicopter vibrations are periodic.

Finally, the effects of HHC on chaotic response, if any, are also addressed.

B. PRELIMINARIES

1. Conditions of Flight

For the present investigation, the conditions of flight are at 60 knots airspeed with the HHC system turned off. This condition is the most benign of the

available data. Higher airspeeds lead to greater vibrations. The assumption is that if chaos exists at 60 knots, then, it certainly exists at higher airspeeds. The OH-6A helicopter is a smooth flying helicopter even without HHC. So, the presences of chaos in the response of this helicopter implies chaotic response in other helicopters which are not as smooth.

During the 5 seconds of test data recording, the aircraft was reported to be in steady, level flight with the controls held fixed and the air smooth.

2. Data Presented

The analysis presents the time history, the Fourier spectrum, the attractor in toroidal phase space, and a Poincare section of the attractor taken at 270 degrees azimuth. The plotting about the torus is synchronized with the rotor and is at 1P. That is, the rotor time domain is employed. The embedding time is 10 samples for the construction of pseudo phase space. A dashed horizontal line on the Fourier spectrum indicates calculation noise associated with the Fourier transform.

3. Analysis of Data

The first analysis step is to examine the time histories for quantization error. An example of a signal with large quantization error is shown in Figure 4-3. A large quantization error leads to misleading results in

the chaos methods. The appearance of chaos in such signals may be attributed to the quantization error.

Examination of the Fourier spectrum is the second step. The appearance of a broad spectrum of frequencies, at least one order of magnitude above calculation noise, is an indication of the presence of chaos. On the other hand, if the Fourier spectrum shows the signal as periodic, then there are no chaotic vibrations.

The third step is the examination of the signal in toroidal phase space. Trajectories spread out over a Poincare section is another indication of presence of chaos.

4. Measurements Presented

Forty nine measurements were available for the analysis. Appendix B lists these measurements. Although all the measurements were examined, only a representative sample are presented here.

C. AIRCRAFT FLIGHT TEST MEASUREMENTS

1. Blade Feathering

The aerodynamic angle of attack that a rotor blade experiences is a result of a combination of the blade feathering, blade flapping and rotor azimuth position, among other parameters. Figure 10-1 presents a sample of blade feathering data as measured by a potentiometer. This signal also includes components of

blade flapping because of cross coupling. In other words, the potentiometer not only moved with blade feathering, but also moved a small amount with the blade flapping.

The blade feathering motion is essentially periodic. The largest component in the response is the 1P or about 8 hertz. The position of the swashplate controls the blade feathering. The pilot positions the swashplate through the control stick. Any changes in control position would cause shifts in the attractor in toroidal phase space. In this sample, the controls were held steady by the pilot for the 5 second measurement.

Notice that monitoring blade feathering in toroidal phase space allows for checking for steady flight controls; an important parameter for deciding if the data is good. Normally, the time histories for longitudinal and lateral cyclic stick position and collective stick position are monitored to decide if the data is good.

2. Blade Flapping

Figure 10-2 presents the blade flapping data measured by a potentiometer. Cross coupling with blade feathering is present in this data. A small amount of quantizing error is apparent by viewing the time history (Note that quantization error may sometimes not be apparent in the reduced plots presented in this

dissertation). In this figure, about 60 quantum levels encompass the peak to peak measurement out of the 1024 quantum levels available. However, blade flapping appears periodic. The largest frequency component is the 1P.

3. Blade Flapwise Bending

Figures 10-3 through 10-5 present the rotor blade flapwise bending measured by strain gages mounted on the surface of the rotor blade. The locations of the strain gages are at 15, 50 and 90 percent, respectively, of the rotor radius measured out from the rotor hub. The data from the outboard strain gages are an indication of the effects of unsteady aerodynamics. The data from the strain gage at 15 percent rotor radius is an indication of the flapwise shear forces transmitted to the rotor hub.

Quantizing error is apparent by examining the time history of all three signals (only about 50 quantum levels are used in each). The data from all the three strain gages are mostly periodic with a small amount of chaotic or random behavior. The source of this behavior may be due to the rotor blade's unsteady aerodynamics. The frequency content of flapwise bending varies considerably with rotor radius.

4. Blade Chordwise Bending

Figure 10-6 presents the rotor blade chordwise bending measured by a strain gage mounted on the surface of the rotor blade. The location of the strain gage is at 17 % of the rotor radius measured out from the rotor hub. The data from this strain gage is an indication of the edgewise shear forces transmitted to the rotor hub. The chordwise bending has a strong 1P and 4P components. This bending appears more chaotic or random than the flapwise bending. The source may be the rotor blade lead-lag damper.

5. Blade Torsion

Figure 10-7 presents rotor blade torsion measured by a strain gage mounted on the surface of the rotor blade. The location of the strain gage is at 17 % of the rotor radius out from the rotor hub. Torsional response was about a third of chordwise or flapwise bending. Although the peak to peak amplitude contains only 20 quantum levels, the signal appears to be periodic with the strongest component at 1P.

6. Rotor Mast Bending

Figures 10-8 and 10-9 present the longitudinal and lateral mast bending respectively. The rotor mast on the OH-6A is stationary relative to the fuselage. The strain gages mounted on the mast and below the rotor head provide an indication of the vibrations transmitted to

the helicopter. The data from these strain gages reflect vibrations after the rotor filtering of the flapwise and edgewise rotor blade root shears. In theory, only the 4P component should filter through.

The amplitude of the 4P component was more than 10 times greater than any other frequency in the spectrum. Other components are also present in the spectrum. The rotor acts as a filter, but does not completely filter out all the other frequency components.

7. Pilot Seat Acceleration

Figures 10-10, 10-11, 10-12 depict the vertical, longitudinal and lateral accelerations, respectively. A triaxial accelerometer placed under the right pilot's seat provides these accelerations. This main objective of HHC is to reduce this acceleration. These signals have the smallest quantization error of all the signals presented. For these signals, over 100 quantum levels encompass the peak to peak amplitudes.

Observe that chaotic or random vibrations are indicated in all three directions of acceleration. The broad band noise is at least 10 times the Fourier transform calculation noise. At this airspeed, the broad band noise contained about 34 percent of the total vibratory energy in the acceleration signals. The 4P contained the remaining 66 percent. HHC reduced these 4P

vibrations by 90 percent, which meant a 60 percent reduction in overall vibrations.

The Poincare sections show a large spread in the attractors. The distance across the attractors is about 40 percent of peak to peak amplitude in all three signals. In all of the other signals, the attractors were compact and the greatest spread was about 20 percent of peak to peak.

8. Tail Boom Vertical Bending

Figure 10-13 shows vertical bending of the tail boom. The quantization error is the largest of the data samples presented. Only 20 quantum levels represent the entire peak to peak amplitudes. Although quantization errors are high, the tail boom bending appears periodic with strong 1 and 4P components.

Although not presented, lateral bending of the tail boom had roughly the same characteristics as vertical bending.

D. SEARCH FOR CHAOS

At this point, the presence of chaotic vibrations is indicated in a qualitative way in some signals. However, the observed chaotic vibrations may also be periodic vibrations with superimposed random vibrations. This section presents the investigation to characterize quantitatively the observed chaos.

The data from the vertical accelerometer located under the pilot's seat are examined for evidence of chaotic vibrations. This signal has the minimum quantization error of all of the 49 signals that were made available. It has the greatest indication of chaotic vibrations. The HHC system was also conceived to reduce this acceleration. Further, this is the very signal that was presented as the 'Actual' signal in Chapter 6 (that is why it was an example in that chapter).

1. The Strange Attractor

Discovery of a strange attractor in a Poincare section is a sure sign of chaos [Ref 6.15, 6.17, and 6.19]. Figure 10-14 presents a 3-D Poincare section of a 4-D hyperspace for 5 seconds of the vertical accelerometer data.

The points seem to form a strange attractor. They are arranged in the horseshoe like shape of the simple stretching and folding process discussed in Chapter 6.

Figure 10-14 plots 13 points, far too few to deduce the presence of a strange attractor. For more points, steady flight test data is needed for a duration longer than 5 seconds. However, maintaining a steady flight condition in a helicopter for longer than 5 to 10 seconds imposes practical difficulties. Wind tunnel test

data for durations of about two minutes would be worthwhile for further studies in chaos.

2. Implications of the Lyapunov Exponent

The presence of chaos in a nonlinear dynamic system implies a sensitive dependence to initial conditions. That is, if two trajectories were to start from neighboring initial conditions in phase space, then they will move exponentially away from each other after a certain interval of time. Hence, a chaotic system is known to yield at least ONE positive Lyapunov exponent [Ref 6.9].

The size of a positive exponent indicates the time scale on which a dynamical system becomes unpredictable. In other words, positive exponents measure the rate at which a system loses information [Ref 10.1]. In Chapter 6, an averaged Lyapunov exponent estimate of 0.3 to 1.7 bits/sec was presented for the vertical accelerometer data. A 10 bit word measured this signal. This signal, then, represents a system that becomes completely unpredictable after 6 to 30 seconds, since no bits of the original information remain after this time. The small uncertainty in initial measurement of the signal will cover the entire attractor. Thus all information about the initial conditions are lost.

However, the real result is more complex. The Lyapunov exponent is a time average of many computations

of Equation 6.9. Figure 6-18 presents the computation of the instantaneous Lyapunov exponent. The instantaneous exponent varies wildly with a standard deviation of about 15 bits/sec. The peak to peak exponent is from + 67 bits/sec to - 52 bits/sec. A large positive exponent implies that the predictability is lost in less than a 1/6 of a second or little more one rotor revolution.

Figure 7-2(b) confirms this result. An intersection with the Poincare plane is shown for every quarter revolution of the rotor for the vertical acceleration trajectories. The trajectories are seen to intersect the Poincare section at wildly different locations while remaining within the attractor.

Earlier chapters showed that the helicopter vibrations are linear and repeatable in the rotor time domain for a single frequency. In the case of the OH-6A, the frequency is the 4P. The Lyapunov exponent calculations seem to indicate that to suppress vibrations other than the 4P, an adaptive control system may be required. Updating of the 'T' matrix must be done several times during each rotor revolution. The typical HHC system is known to update only once a rotor revolution.

3. Implications of Fractal Dimension

The fractal correlation dimension, discussed in Chapter 6, was computed for the vertical acceleration

signal. The results are presented in Figure 6.22. To obtain an asymptotic value, the pseudo phase space dimensions were increased. The fractal dimension levels off at a value of about 6.6. Similar studies were performed for both lateral and longitudinal accelerations. The final converged values for fractal dimension are 6.3 and 6.4, respectively. Note that the time histories for these three signals differ significantly. Also note that unlike the Lyapunov exponent algorithm, the fractal dimension algorithm was not sensitive to small changes in input parameters and gave consistent results.

The literature reports that obtaining a non-integer for the asymptotic fractal dimension is a definitive indication of chaos. A non-integer fractal dimension also indicates the presence of a strange attractor [Ref 6.13, 6.15, 6.17, 6.19]. However, recently, Osborne and Provenzale [Ref 10.2] contend that the sole observation of a non-integer fractal dimension is not enough to infer the presence of a strange attractor or chaos. They base their hypothesis on finding a finite fractal dimension for colored white noise. Figure 6.22 presents the fractal dimension of the Random signal (generated by a random number generator). The Random signal does not reach an asymptotic value. Note that for a 'true' Random signal, generated without

the truncation and round-off errors in a computer, the fractal dimension should increase linearly with increasing dimension of pseudo phase space (indicated by the dark line in Figure 6.22).

In Figure 6.22, the fractal dimension curve for the vertical acceleration data lies below the Random signal's curve and above both the 32 hertz and Harmon signal's curves. This signifies the fractal dimension calculation for the Actual signal is a result of chaotic vibrations and not random vibrations.

4. Chaos ?

The evidence points to chaos in some helicopter vibrations. This conclusion is based on the non-integer correlation dimension, the observation of broad-band Fourier spectrum, the presence of a positive Lyapunov exponent, together with the evidence of a strange attractor in the Poincare sections.

E. CHAOS IN HELICOPTERS - WHAT DOES IT MEAN ?

The presence of chaos in helicopter vibrations imposes limits on the ability to predict and control vibrations using active vibration control systems. A general belief is that accurate prediction is assumed possible by gathering and processing enough information. A simple deterministic system, even with only a few elements, can result in chaotic behavior. Chaotic

behavior is a system characteristic and gathering more information does not eliminate it or increase the predictability beyond a certain limit.

Many helicopter simulation programs make the assumption that helicopter vibrations are a sum of several harmonic functions. The second example used in the chapter 6, the Harmons example, illustrated the effect of this assumption. Often, discrepancies between experimental and computational results may be explained by the presence of chaos in the experimental results.

Chaos can arise from a finite number of non-linear deterministic equations. Modeling of random vibrations, on the other hand, is limited to a statistical description of the vibrations. The fractal dimension calculation seems to indicate that at least seven coupled first order differential equation can model the pilot's seat vibration response. Future simulation programs may more accurately model vibrations by considering the implications of the nonlinearities present in the system, as evidenced by the chaos.

Finally, only non-linear systems are capable of producing chaos. Typical sources of nonlinearities in helicopters are unsteady aerodynamic effects, large structural deformation, nonlinear material behavior, and control laws. Investigation of helicopter response for

chaos can help identify the effects of these nonlinearities.

F. HOW ABOUT HHC ?

On analyzing the data with HHC on, HHC did not seem to change the chaotic behavior of the vibrations.

Figures 8-2 and 8-3 demonstrated that HHC simply moved the attractor, but it did not change the size of the attractor in toroidal phase space.

Figure 10-15 shows the effects of open loop HHC in 3-D phase space. The data presented is the vertical acceleration under the pilot's seat at 60 knots. The figure presents three conditions; lateral HHC at 270 degree controller phase, baseline (HHC off), and lateral HHC at 90 degree controller phase. Note that minimum vibrations were achieved at 270 degrees controller phase while 90 degree phase lead to worst vibrations. Figure 10-16 presents effects of Closed Loop HHC. The data presented is the vertical acceleration at 100 knots. Both figures show the attractor in 3-D phase space and a Poincare section of this attractor.

The HHC makes the vibrations appear more chaotic in 3-D phase space. In fact, what actually happens is that the HHC removes the deterministic component (the 4P) from the vibrations, leaving the chaotic portion behind.

To further study the effects of HHC, Lyapunov exponent and fractal correlation dimension were computed. Both HHC on and HHC off conditions were considered. No significant changes were noted in both the exponent and the fractal dimension. The fractal dimension changed little with HHC on or off, regardless of mode. The Lyapunov exponent also remained in the range of 0.3 to 1.7. HHC does not appear to change the chaotic nature of helicopter vibrations either way.

E. SUMMARY

Although helicopter vibrations are generally assumed to be periodic, the evidence suggests that some helicopter vibrations are chaotic.

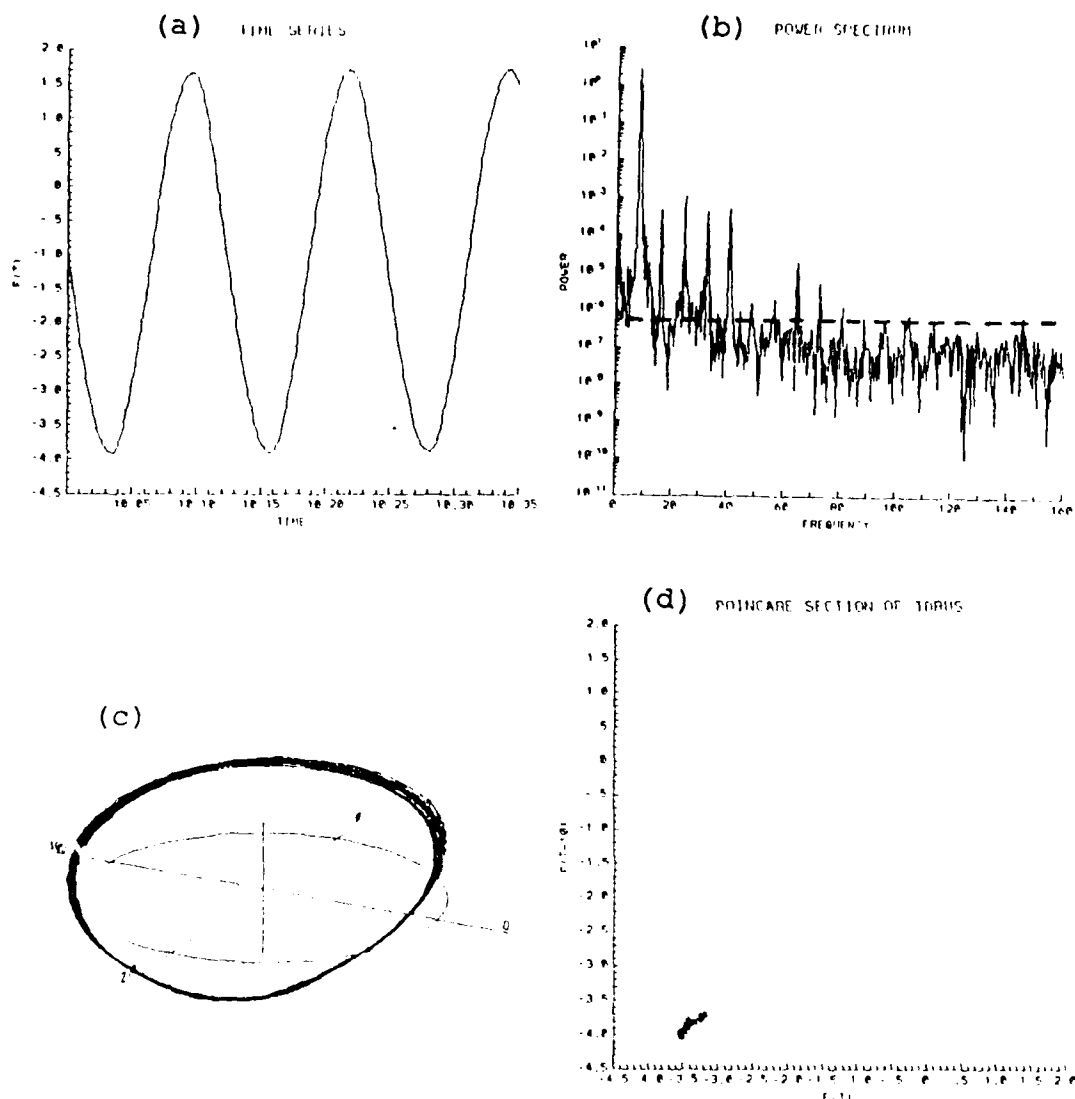


Figure 10-1. Blade Feathering Angle. (a) Time history. (b) Fourier power spectral density plot. (c) Attractor in toroidal phase space. (d) Poincare section of attractor at 270 degrees azimuth.

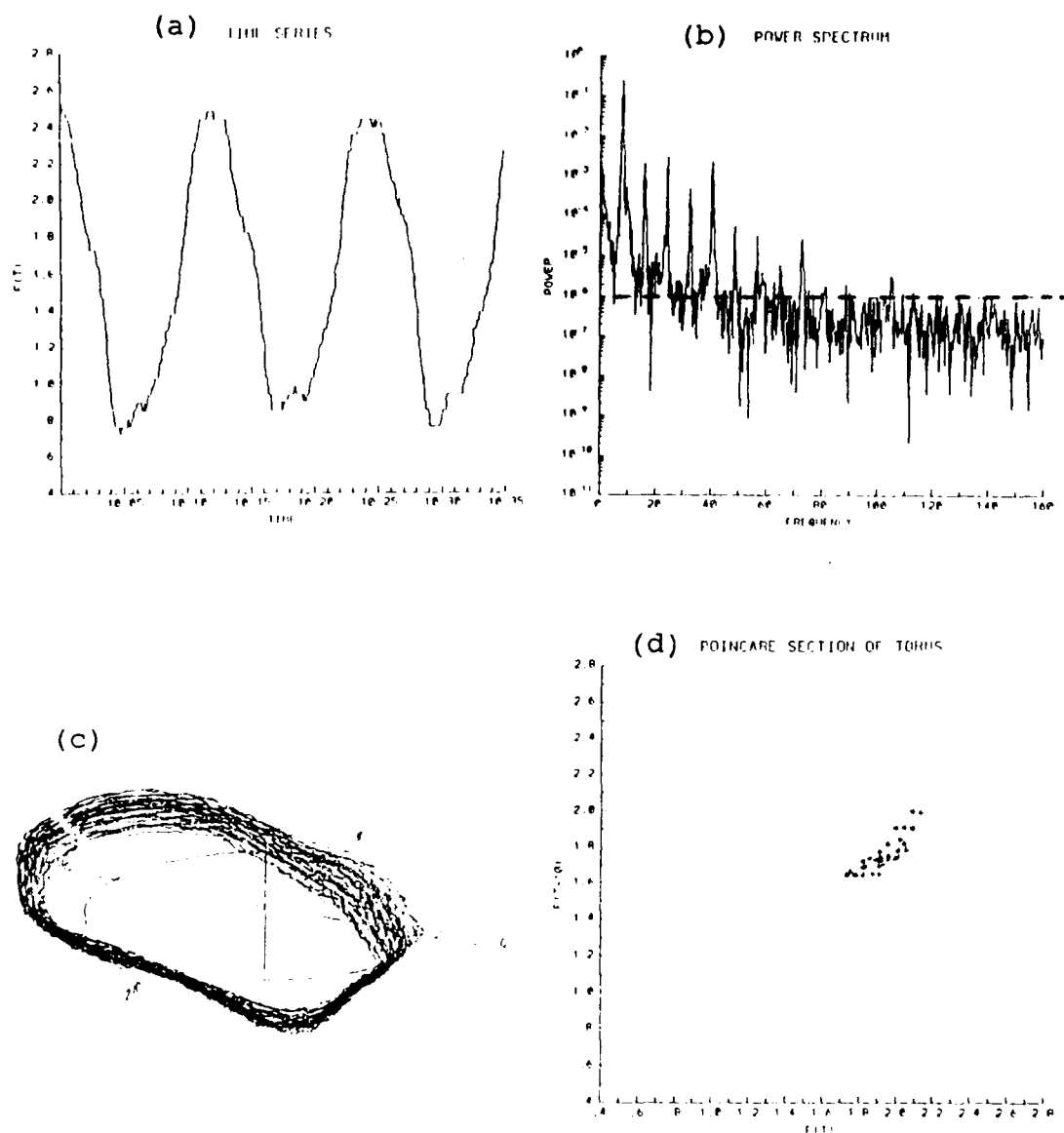


Figure 10-2. Blade Flapping Angle. (a) Time history. (b) Fourier power spectral density plot. (c) Attractor in toroidal phase space. (d) Poincare section of attractor at 270 degrees azimuth.

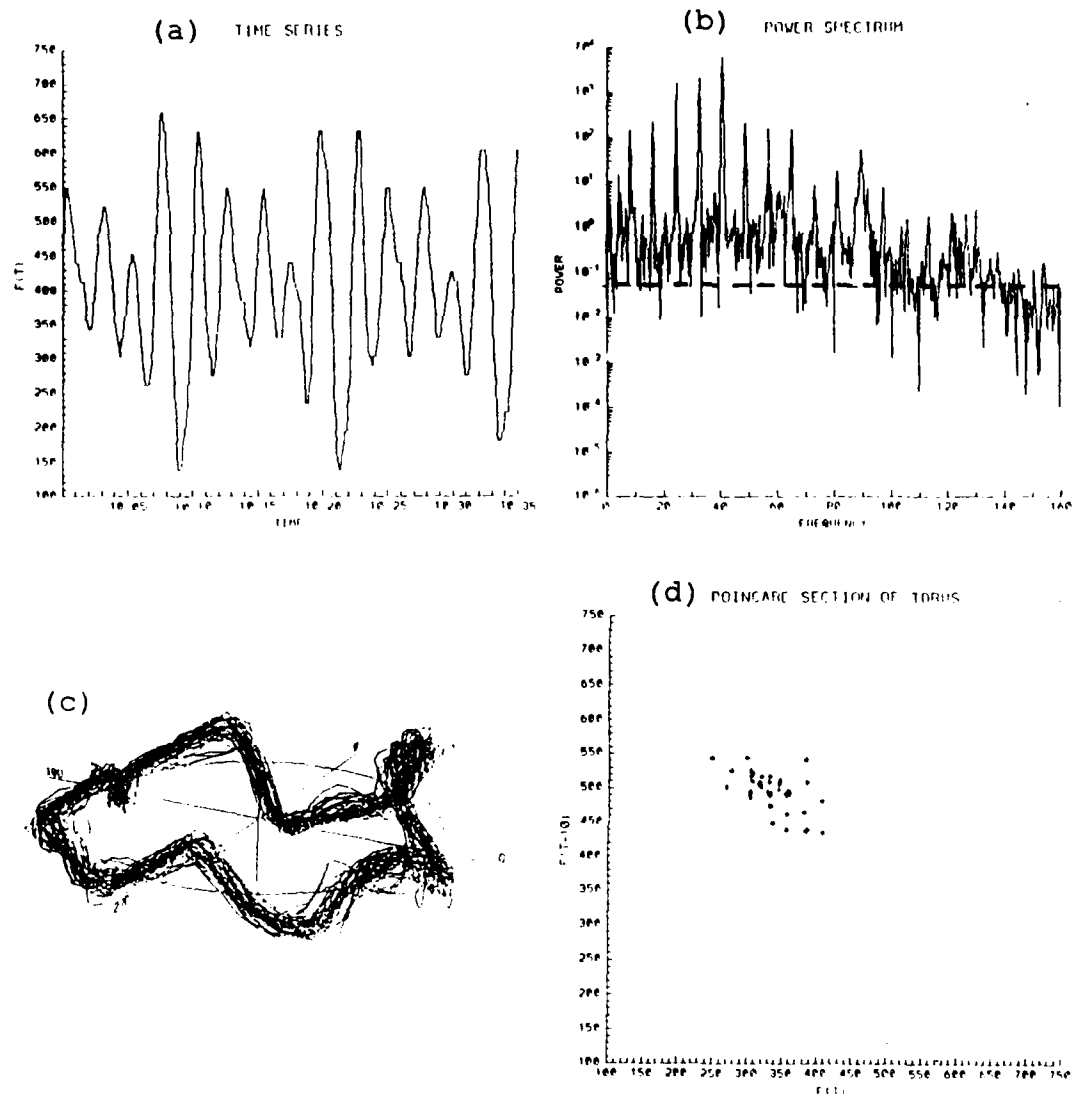


Figure 10-3. Blade Flapwise Bending @ 15 %. Blade flapwise bending at 15 percent rotor radius. (a) Time history. (b) Fourier power spectral density plot. (c) Attractor in toroidal phase space. (d) Poincare section of attractor at 270 degrees azimuth.

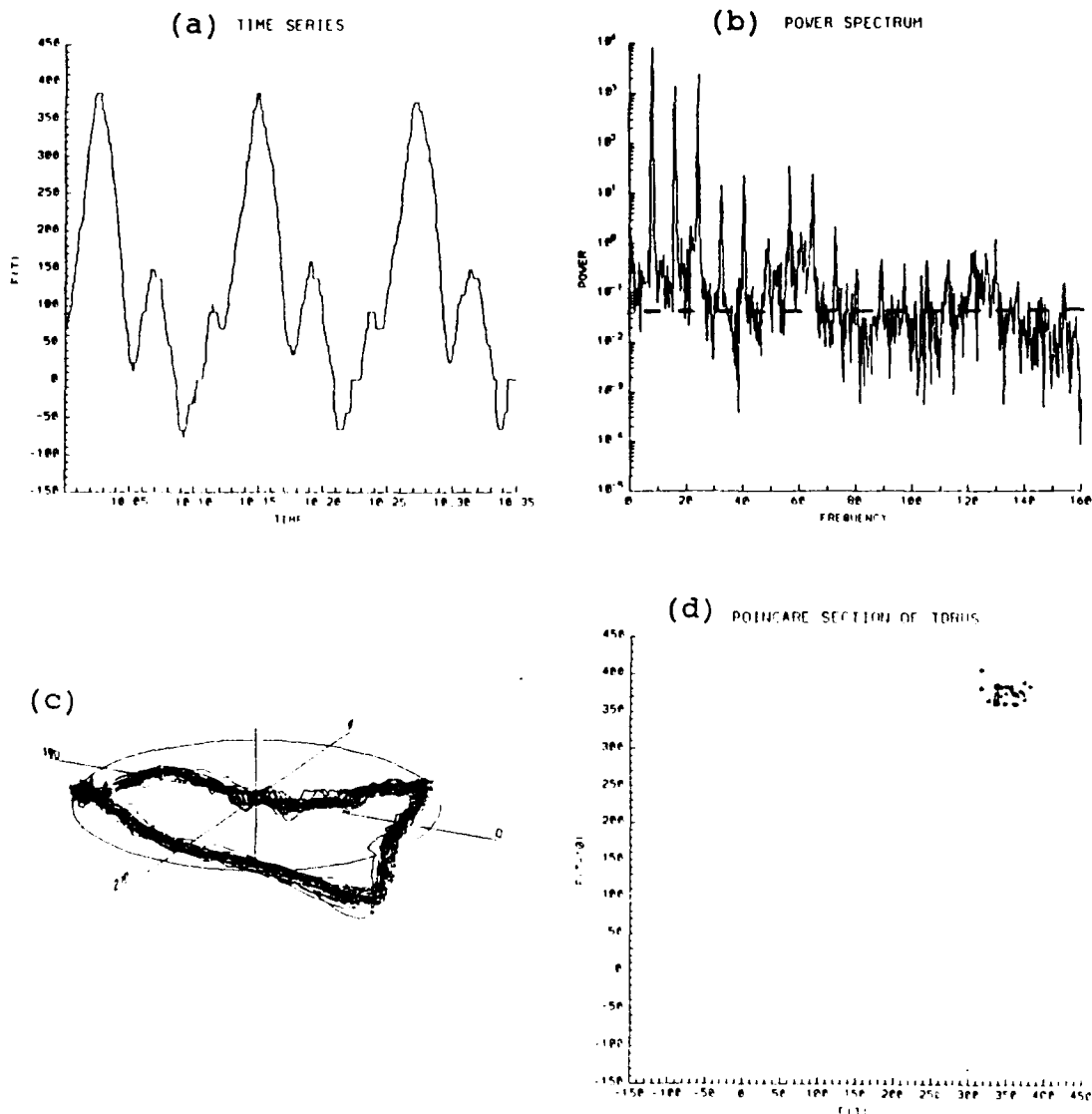


Figure 10-4. Blade Flapwise Bending @ 50 %. Blade flapwise bending at 50 percent rotor radius. (a) Time history. (b) Fourier power spectral density plot. (c) Attractor in toroidal phase space. (d) Poincare section of attractor at 270 degrees azimuth.

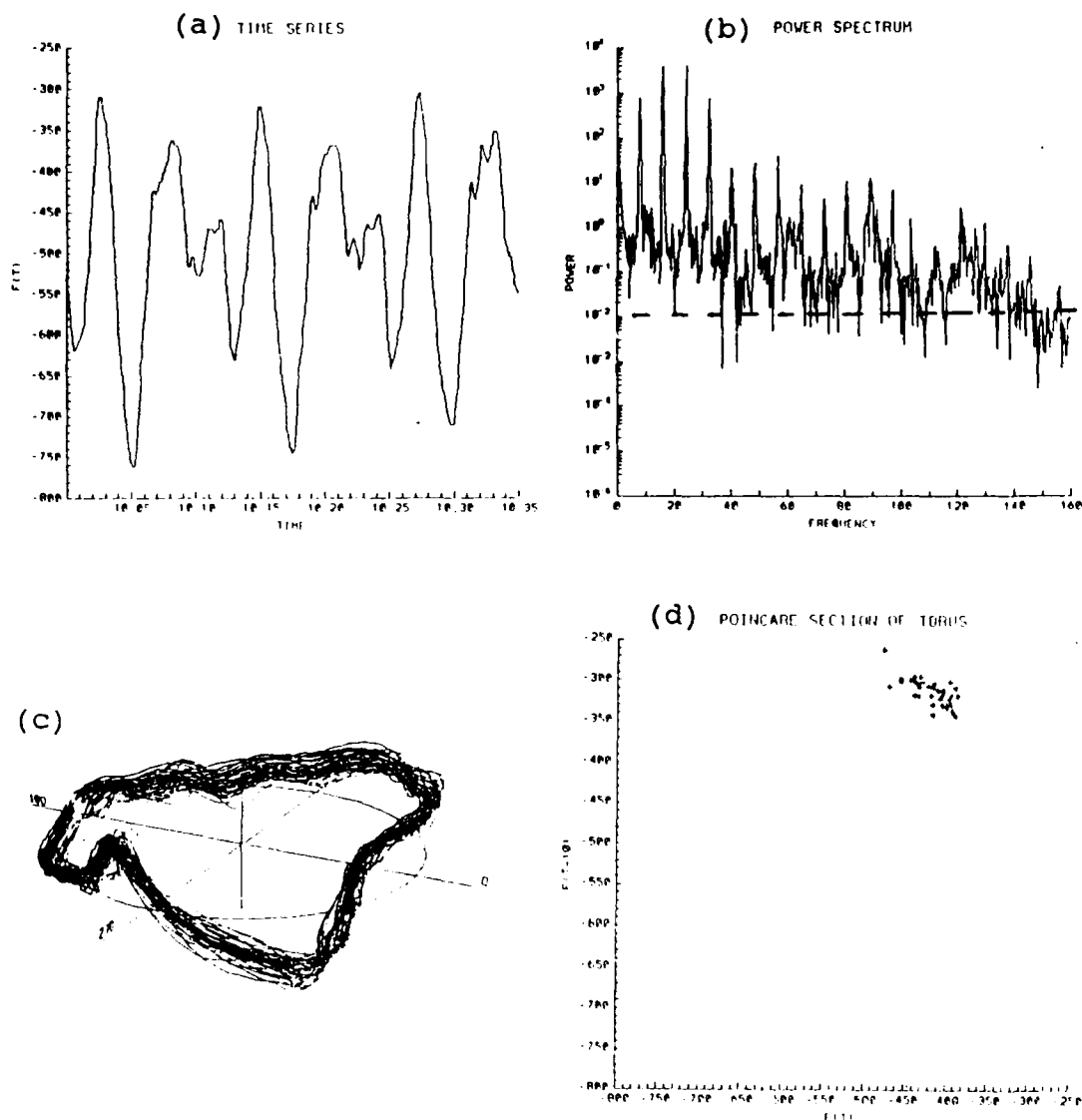


Figure 10-5. Blade Flapwise Bending @ 90 %. Blade flapwise bending at 90 percent rotor radius. (a) Time history. (b) Fourier power spectral density plot. (c) Attractor in toroidal phase space. (d) Poincare section of attractor at 270 degrees azimuth.

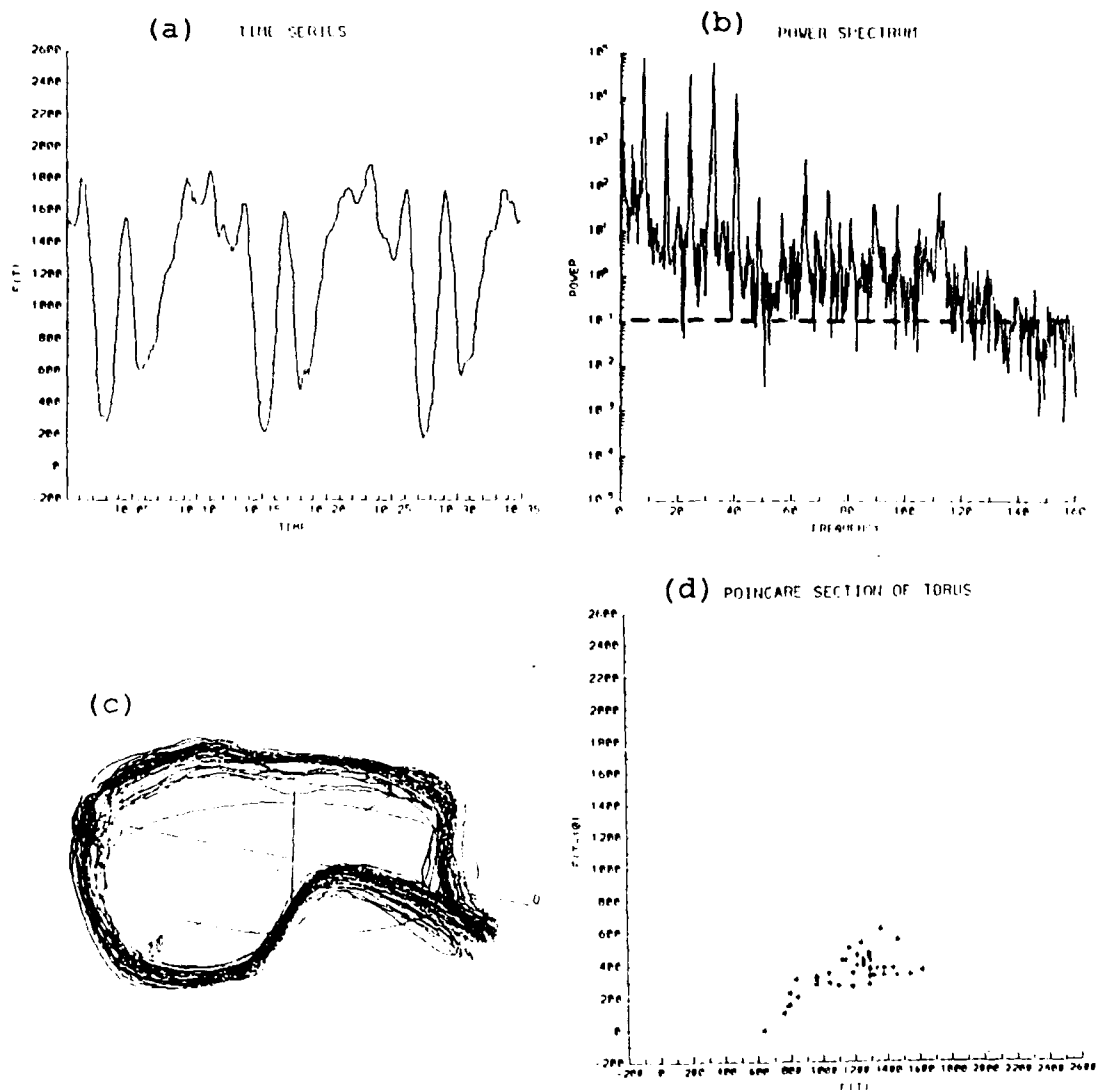


Figure 10-6. Blade Chordwise Bending. Blade chordwise bending at 17 percent rotor radius. (a) Time history. (b) Fourier power spectral density plot. (c) Attractor in toroidal phase space. (d) Poincaré section of attractor at 270 degrees azimuth.

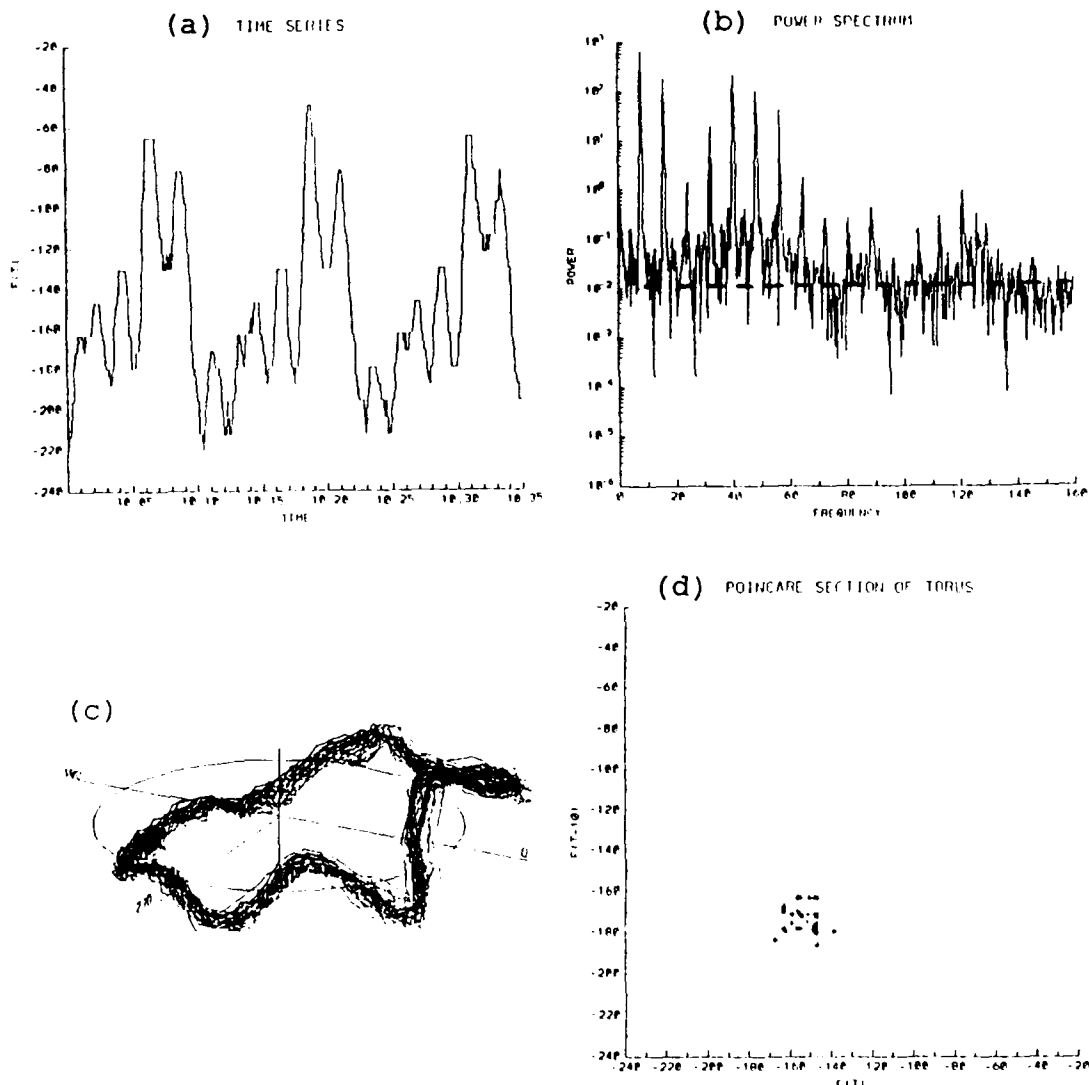


Figure 10-7. Blade Torsion. Blade torsion at 17 percent rotor radius. (a) Time history. (b) Fourier power spectral density plot. (c) Attractor in toroidal phase space. (d) Poincaré section of attractor at 270 degrees azimuth.

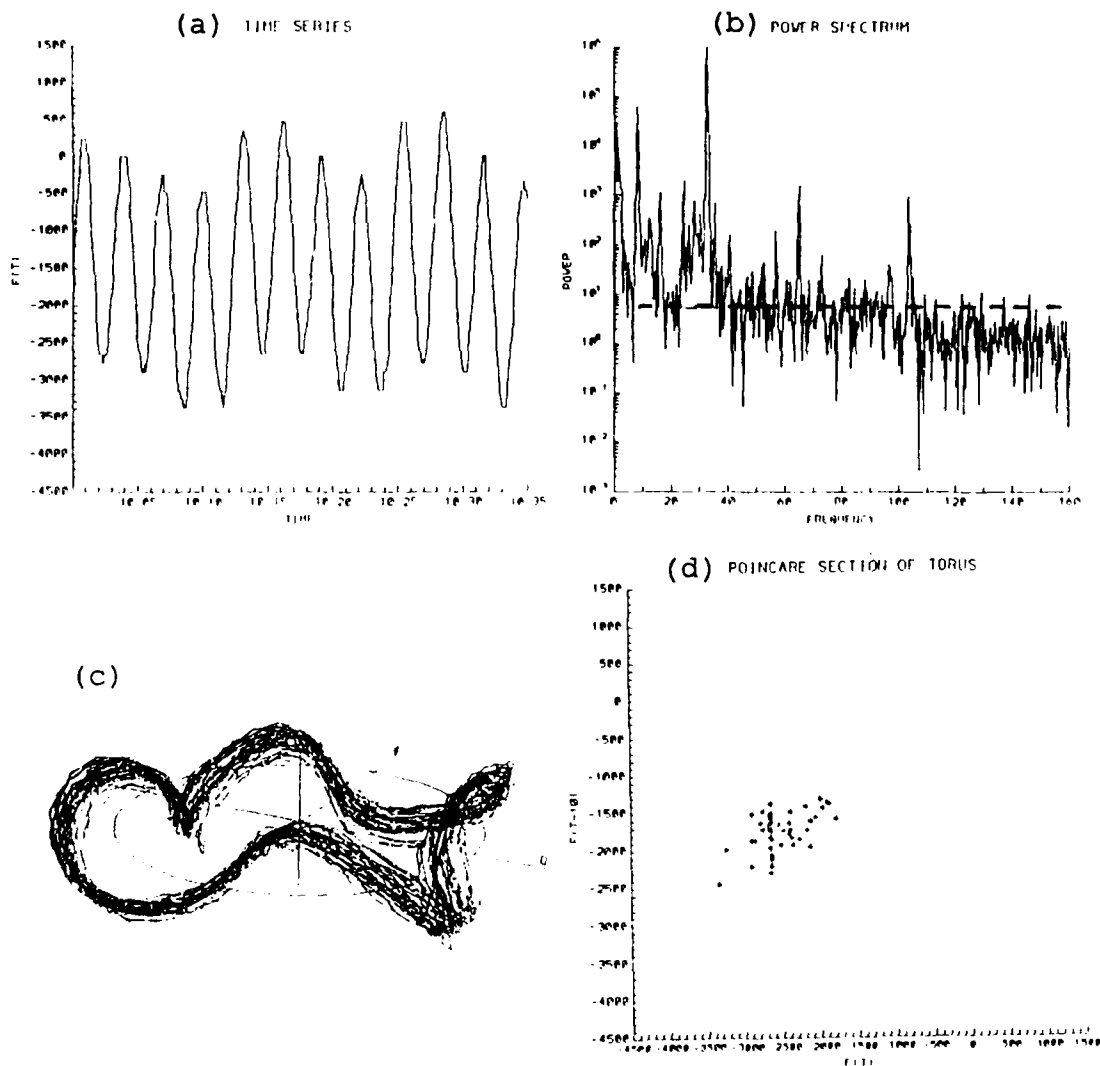


Figure 10-8. Mast Longitudinal Bending. (a) Time history. (b) Fourier power spectral density plot. (c) Attractor in toroidal phase space. (d) Poincare section of attractor at 270 degrees azimuth.

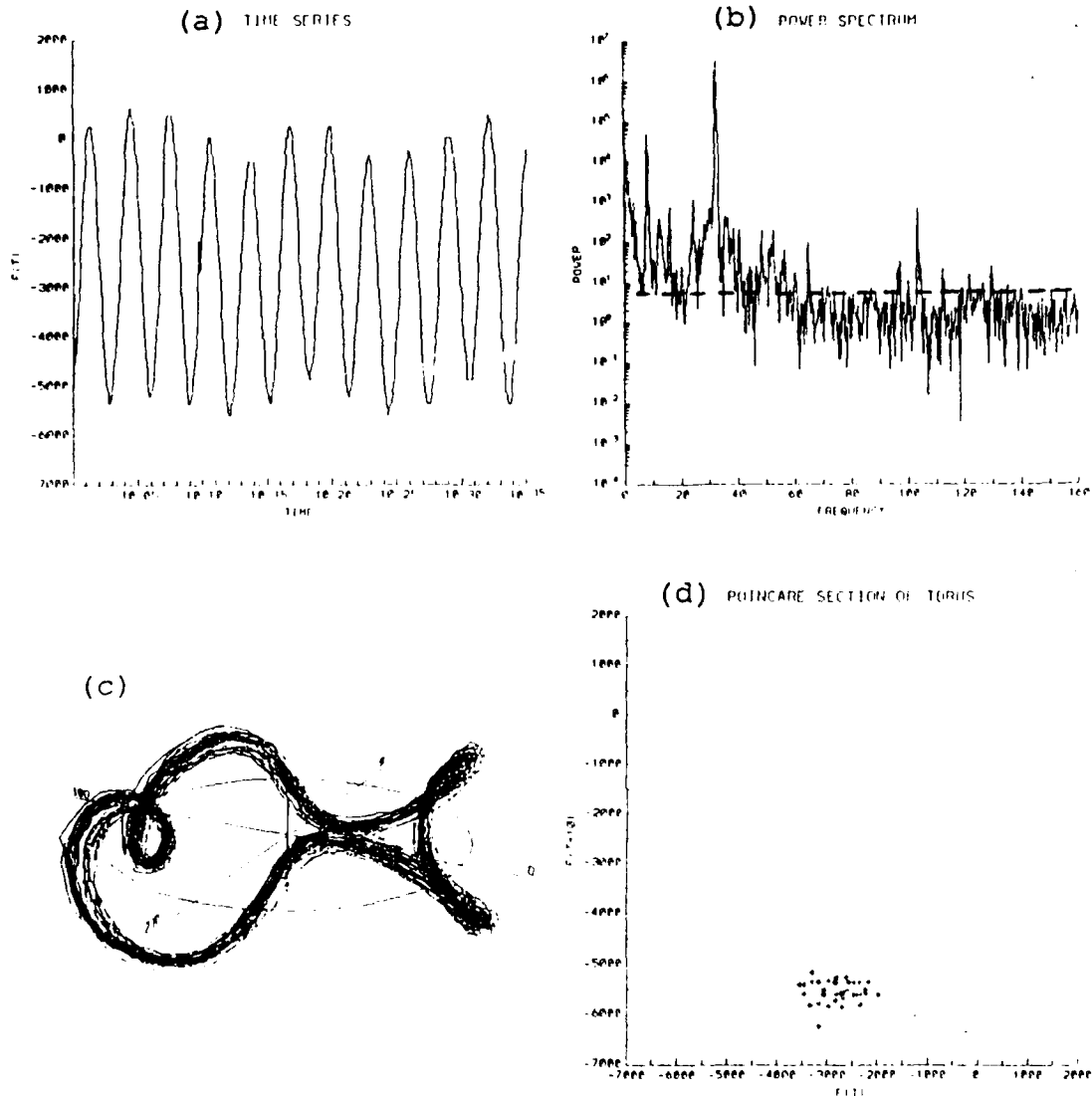


Figure 10-9. Mast Lateral Bending. (a) Time history. (b) Fourier power spectral density plot. (c) Attractor in toroidal phase space. (d) Poincaré section of attractor at 270 degrees azimuth.

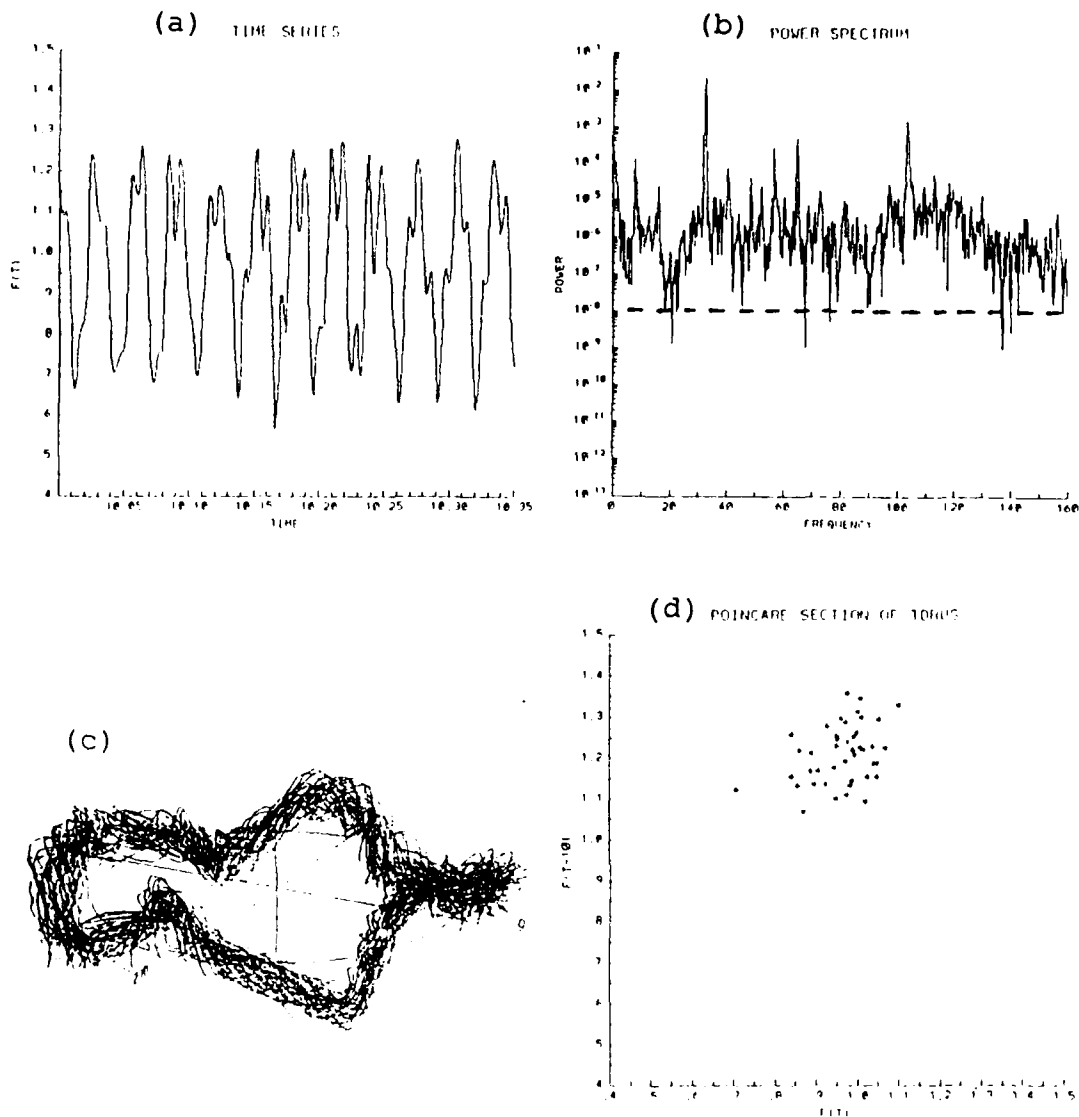


Figure 10-10. Vertical Pilot Seat Acceleration.
 (a) Time history. (b) Fourier power spectral density plot. (c) Attractor in toroidal phase space. (d) Poincare section of attractor at 270 degrees azimuth.

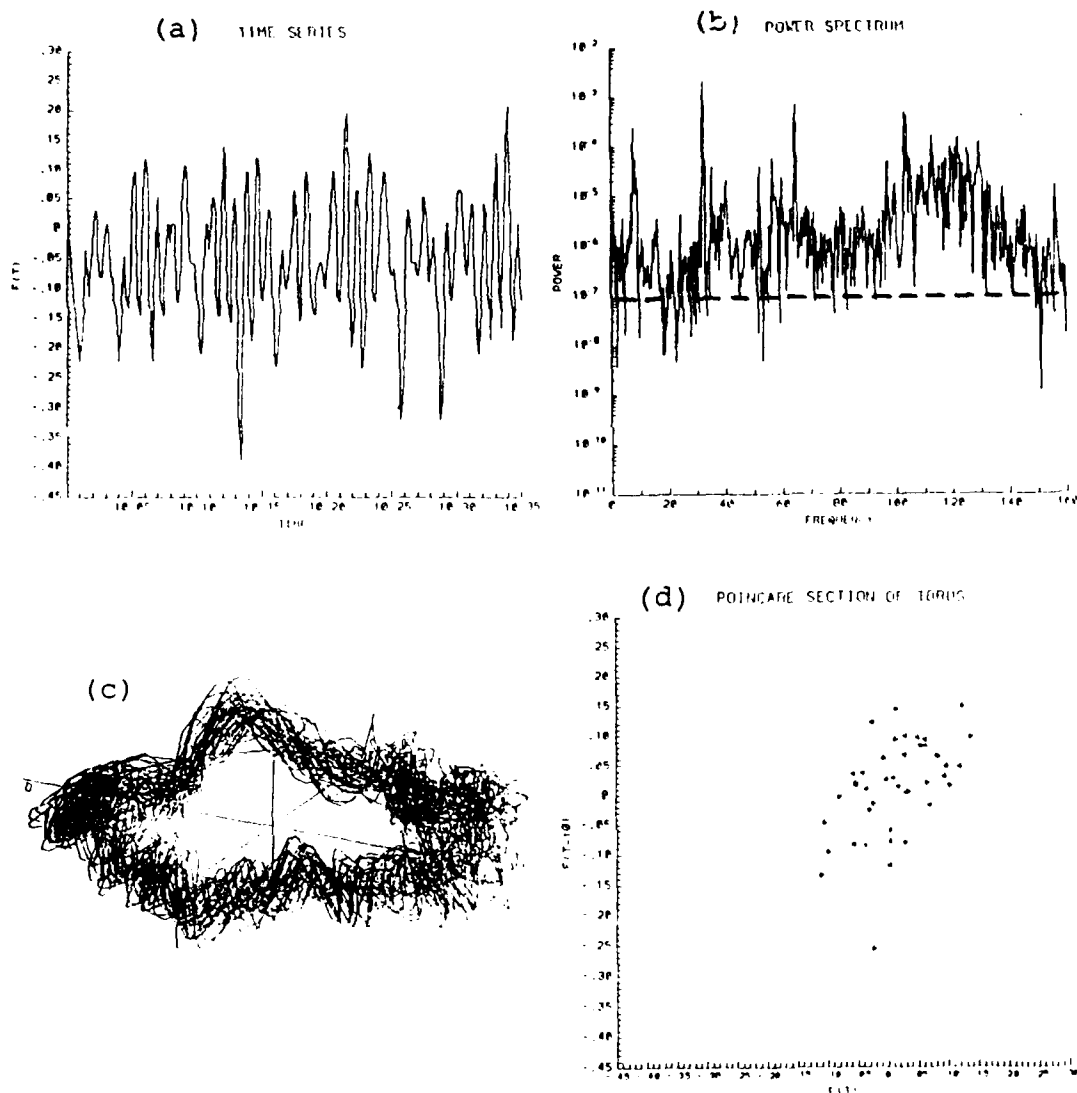


Figure 10-11. Longitudinal Pilot Seat Acceleration.
 (a) Time history. (b) Fourier power spectral density plot. (c) Attractor in toroidal phase space. (d) Poincaré section of attractor at 270 degrees azimuth.

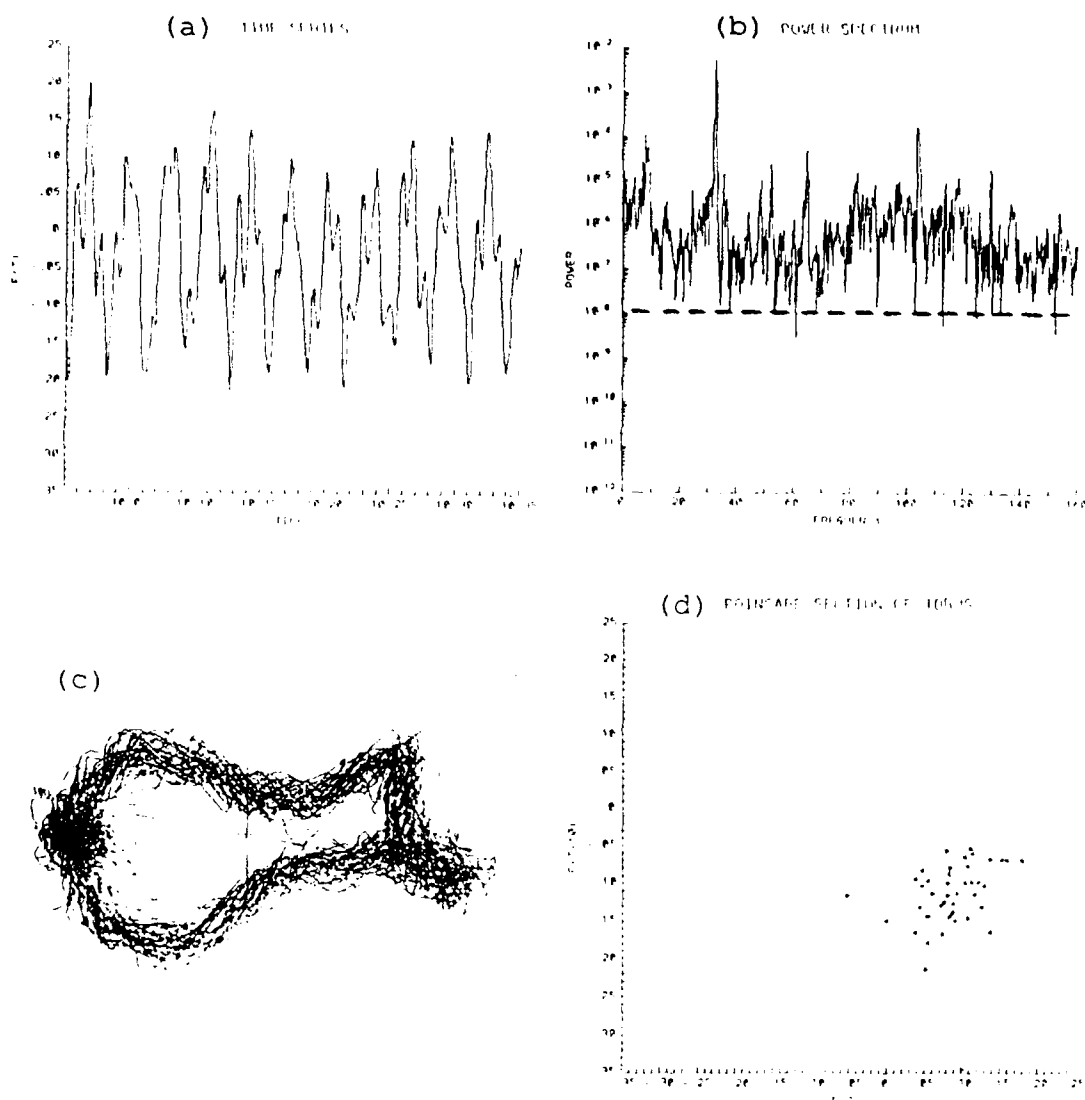


Figure 10-12. Lateral Pilot Seat Acceleration. (a) Time history. (b) Fourier power spectral density plot. (c) Attractor in toroidal phase space. (d) Poincare section of attractor at 270 degrees azimuth.

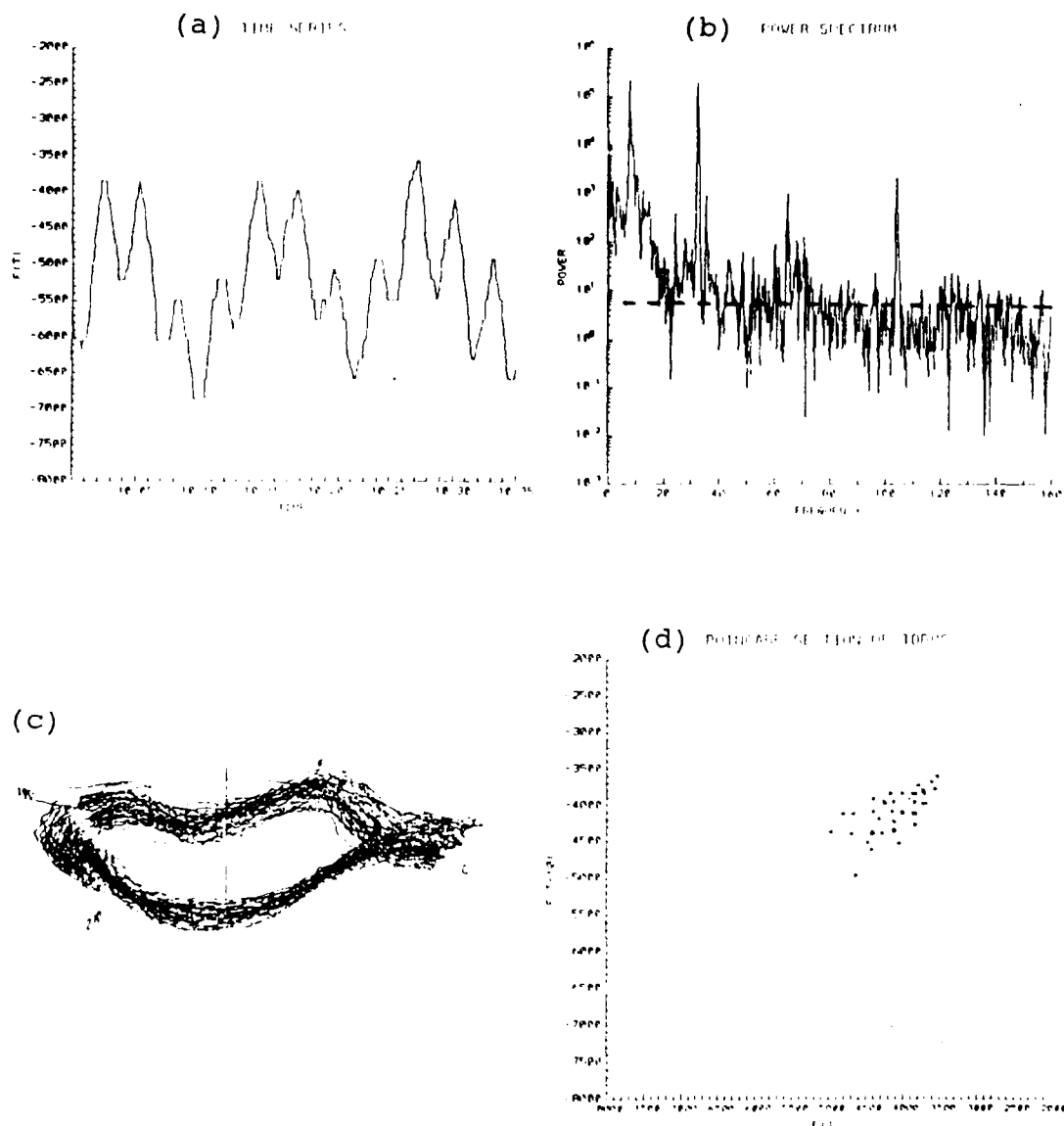


Figure 10-13. Tail Boom Vertical Bending. (a) Time history. (b) Fourier power spectral density plot. (c) Attractor in toroidal phase space. (d) Poincare section of attractor at 270 degrees azimuth.

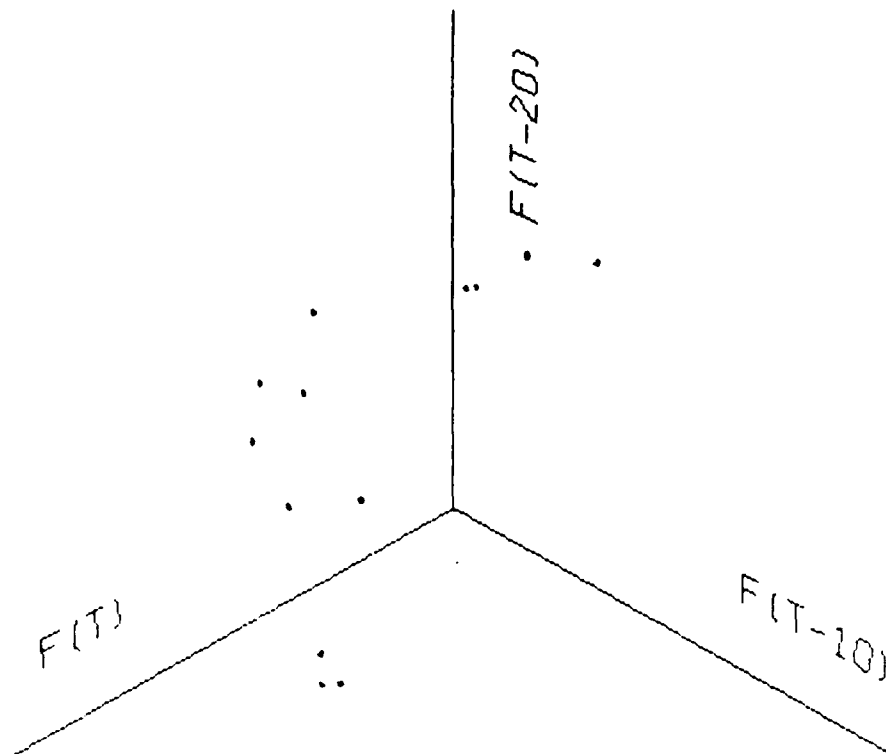


Figure 10-14. A Strange Attractor. A 3-D Poincare section of the pilot seat vertical acceleration. The section is formed by strobing the fourth data array, $F(T-30)$, at a value of 1.37.

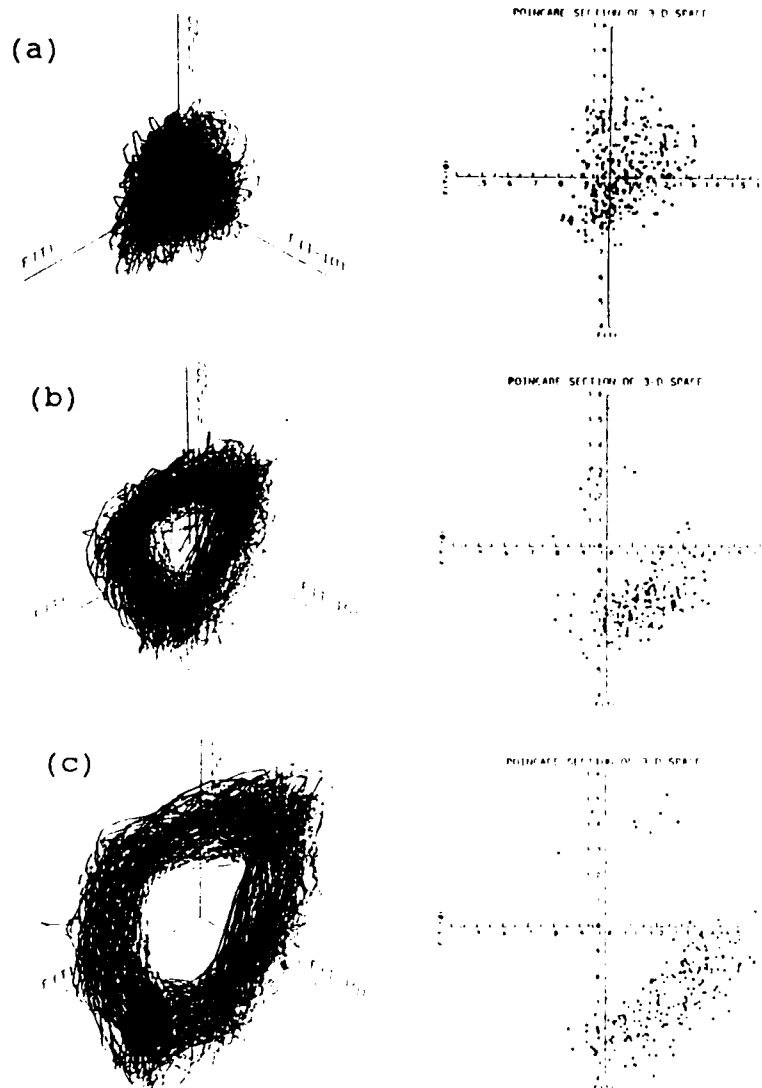


Figure 10-15. Open Loop HHC in 3-D Phase Space.
 Vertical acceleration under the pilot's seat at 60 knots
 airspeed in 3-D phase space (left column). Poincaré
 section taken at $F(T-20)$ equal to 1.0 (right column).
 Only intersections of trajectories traveling upward are
 plotted. Embedding time is 10 samples. Open loop HHC
 with lateral only excitation of swashplate and:
 (a) 270 degree manual controller phase.
 (b) Baseline (HHC off).
 (c) 90 degree manual controller phase.

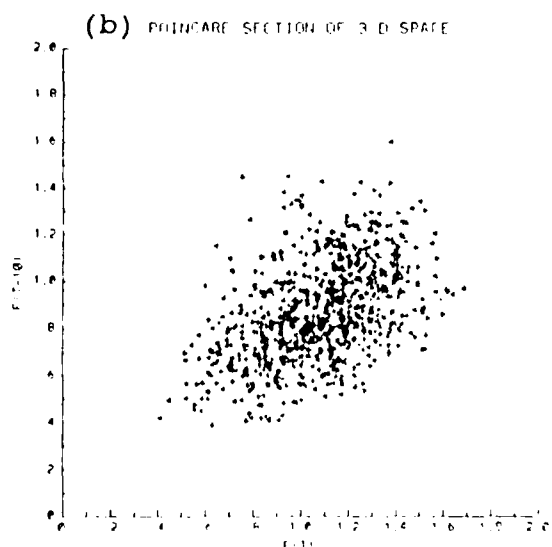
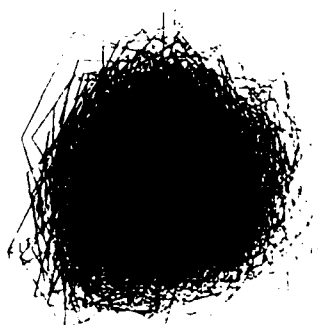
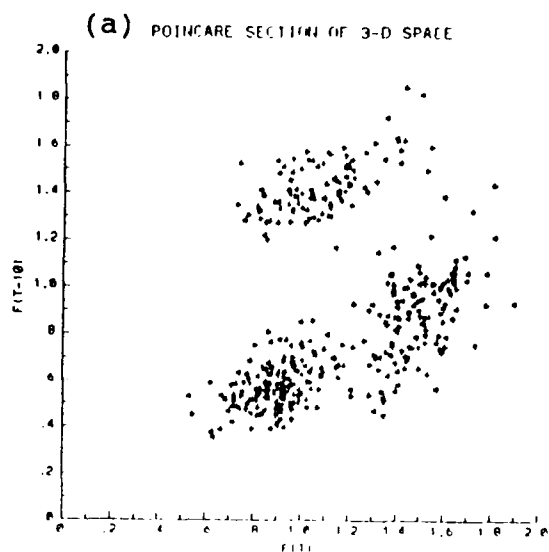


Figure 10-16. Closed Loop HHC in 3-D Phase Space. Vertical acceleration under the pilot's seat at 100 knots airspeed plotted in 3-D phase space (left column). Poincaré section taken at $F(T-20)$ equal to 1.0 (right column). Only intersections of trajectories traveling upward are plotted. Embedding time is 10 samples.

(a) Baseline (HHC off).

(b) Closed loop HHC on.

XI. CONCLUSIONS AND SCOPE FOR FUTURE RESEARCH

The geometric and topological methods of Chaos theory were applied, for the first time, to study flight test data. The data used in this research were from the McDonnell Douglas OH-6A HHC test helicopter. New engineering applications of the Chaos methods were demonstrated with the HHC flight test data.

Although helicopter vibrations are known to be mostly periodic, evidence of chaotic vibrations was found in this study. First, the presence of a strange attractor is shown by computing the Lyapunov exponent and fractal correlation dimension. Then, a broad band Fourier spectrum and a well defined attractor in pseudo phase space were also observed.

An important outcome of this research is that a limit exists to HHC vibration reduction due to the presence of chaos. A new technique based on a relationship between the Chaos methods (the Poincare section and Van der Pol plane) and the vibration amplitude and phase was discovered. This newly introduced technique results in the following: 1) it gives the limits of HHC vibration reduction, 2) it allows rapid determination of best phase for a HHC controller, 3) it determines the minimum HHC controller requirement for any helicopter from a few

minutes duration of flight test data (as an example, for the OH-6A, a scheduled gain controller for HHC appears to be adequate for steady level flight), 4) it shows that the HHC controller transfer matrix is linear and repeatable when the vibrations are defined in the "Rotor time domain" and the matrix is nonlinear and nonrepeatable when the vibrations are defined in the "Clock Time Domain." These deductions have major implications in the design and characterization of controllers.

As a result, this technique will reduce future HHC flight test requirements. Further, although the helicopter must be instrumented, the technique does not require the helicopter to be equipped with HHC to determine the limit of HHC performance or to determine the minimum HHC controller requirement.

These approaches also have potential applications to other vibration control and flight testing problems. Further investigation of chaos in helicopter vibrations is recommended by using several minutes duration of wind tunnel test data. Also, the methods introduced here should be tested with maneuvering flight test data in addition to the steady level flight investigated here.

APPENDIX A
DESCRIPTION OF COMPUTER CODE

A. PURPOSE

This appendix provides a brief description of the programs used in this dissertation. All programs were written in Fortran. Calls were made to GRAFkit, a suite of Fortran callable graphical utilities. It is produced by SCO, Inc. of Louisville, Colorado. GRAFkit is similar to DISSPLA or PV WAVE.

A users manual, source code listing and source code on disk is available by writing the Aeronautics and Astronautics Department, U. S. Naval Postgraduate School, Monterey, Ca.

B. PROGRAM CHAOS

The program CHAOS is a calling program for the subroutines described in this section. It analyzes flight test data using the classical time and frequency domain methods as well as the new chaos methods. Figure A-1 presents a flow chart for this program.

1. Subroutine TIMSER

The subroutine TIMSER (for TIME SERIES) plots the data file as a time series. Different start and stop times may be selected.

2. Subroutine TORUS

The subroutine TORUS (for TORoidal phase Space) plots the trajectory onto 3-D toroidal phase space. Rate of plotting can be fixed at a single frequency or synchronized with the helicopter rotor. The resulting 3-D attractor may be viewed from any perspective.

3. Subroutine PCARE

The subroutine PCARE (for PoinCARE section) plots the Poincare section of a toroidal phase space. Rate of plotting and azimuth angle for the section may be selected.

4. Subroutine PPLANE

The subroutine PPLANE (for Phase PLANE) plots the trajectory onto a 2-D phase plane.

5. Subroutine VDP

The subroutine VDP (for Van Der Pol plane) plots the trajectory onto a Van der Pol plane. The rate of untwisting is selectable.

6. Subroutine PSPACE

The subroutine PSPACE (for Phase SPACE) plots the trajectory onto a 3-D phase space. The resulting 3-D attractor may be viewed from any perspective.

7. Subroutine PCARE2

The subroutine PCARE2 (for PoinCARE 2-d section) plots the 2-D space strobed Poincare section of the 3-D phase space. The orientation of the section, the

direction, and the value to take the section are all selectable.

8. Subroutine PCARE3

The subroutine PCARE3 (for PoinCARE 3-d section) plots the 3-D space strobed Poincare section of the 4-D hyper space. The orientation, direction, and value to take the section at are all selectable. The resulting 3-D section may be viewed from any perspective.

9. Subroutine PSD

The subroutine PSD (for Power Spectral Density) compute and plots the Fourier power spectrum. Seven different window functions are available and the number of points to transform is selectable.

10. Subroutine STATS

The subroutine STATS (for STATistics) computes the time domain statistics. It computes the average, average deviation, variance, standard deviation, skewness, kurtosis and maximum and minimum of the data file.

11. Subroutine LAP

The subroutine LAP (for LyAPunov exponent) estimates the largest non-negative Lyapunov Exponent from a time series.

12. Subroutine COD

The subroutine COD (for fractal Correlation Dimension) estimates the fractal correlation dimension from a time series.

13. Subroutine READATA

The subroutine READATA (for READ DATA) reads data from a file. The data may be differentiated, integrated or time shifted to form a 'fake' observable. The subroutine counts the number of data points in the file and also finds the maximum and minimum amplitude. This subroutine is specialized to read HHC data.

14. Subroutine COLOR

The subroutine COLOR setups the color table for various printers and screens.

15. Subroutine READPIP

The subroutine READPIP (for READ PIPer) reads a pippier data file created by the utility program PIPPER. It passes the time the pippier fires to the subroutines TORUS, PCARE, and VDP.

C. UTILITY PROGRAMS

1. Program PIPPER

The program PIPPER reads the HHC data pippier data file (over 6000 data points) and generates a new data file (less than 50 points) which contains the time the

rotor pipper fired. The subroutine READPIP reads this file during the program CHAOS execution.

2. Program EQPLOT

The program EPLOT (for Equation PLOT) allows analysis of derived quantities by multiplying, dividing, adding, subtracting or raising to a power HHC data files. The results may be immediately plotted or they may be sent to a file for later analysis by program CHAOS.

3. Program CORRECTDAT

The program CORRECTDAT (for CORRECTION of DATA) rewrites 307.5 hertz data into the standard HHC 1230 Hertz sampling rate format.

4. Program CHKTIM

The program CHKTIM (for CHECK TIME) finds the errors in the data files caused by the McDonnell Douglas Helicopter Company's conversion from PCM format into ASCII format.

5. Program TDATA

The program TDATA (for Test DATA) generates a file of test data usable by the program CHAOS or EQPLOT.

CHAOS - The Program

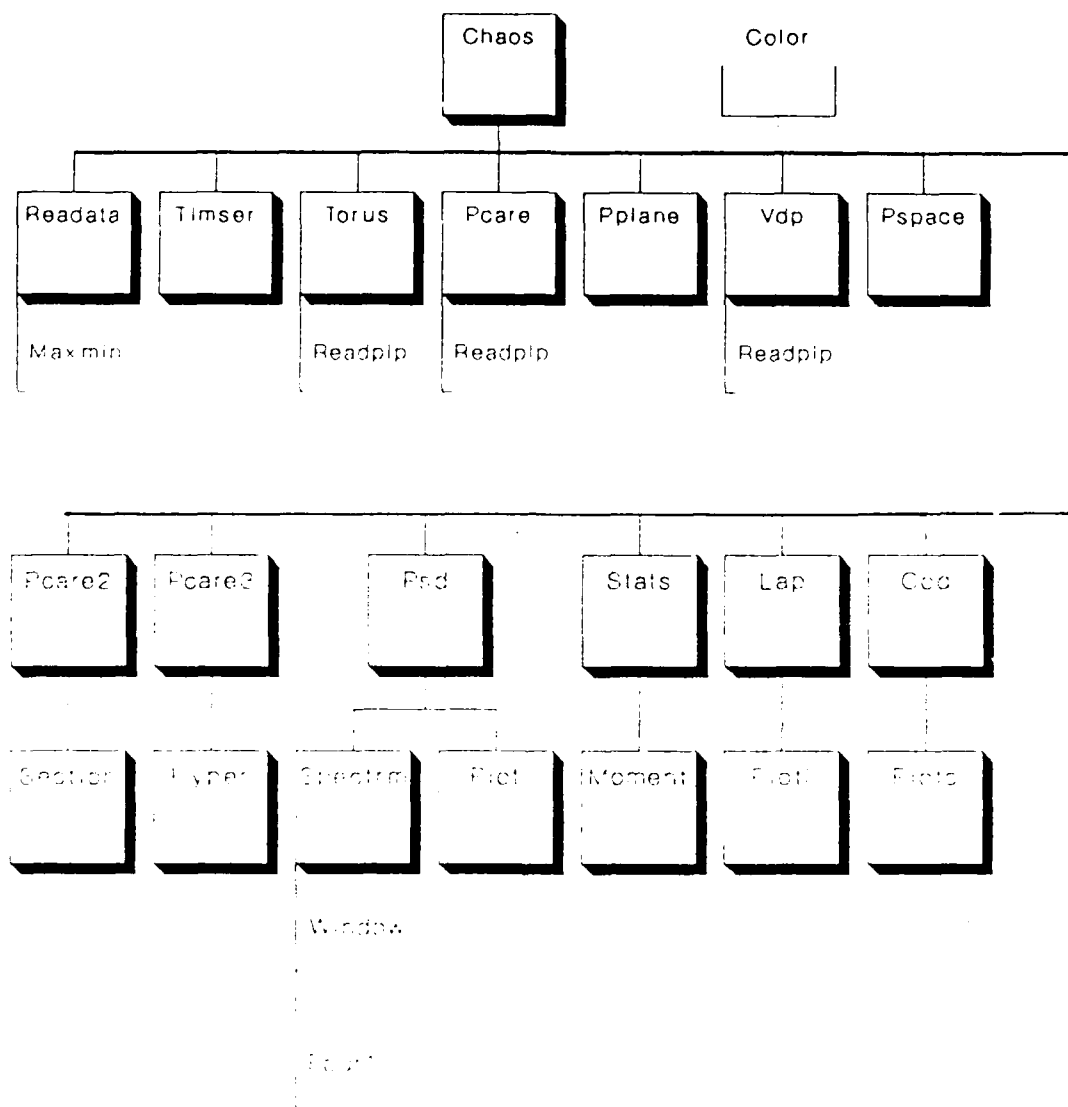


Figure A-1. Flow Diagram for program Chaos.
Program is written in Fortran. For a copy of the users manual and source code, write the Naval Postgraduate School.

APPENDIX B

HHC MEASUREMENT LIST

This appendix presents the measurements available from the OH-6A helicopter. Given are the McDonnell Douglas measurement number, the measurement name, the units of the measurement and frequency cutoff of the anti-aliasing filter (if known). The measurements were translated into ASCII files, readable by a VAX computer. They were stored in data files with ten measurements per file. For the open loop test data, to store all 49 measurements at each flight test condition took 5 groups of files. In the case of closed loop test data, only 9 measurements were made available. Hence only one data file represented all the data at one flight test condition for closed loop data.

Each open loop test data file was given a 7 character file name. The first letter of the file name indicated mode (i.e. 'L' for lateral excitation), the second number indicated airspeed (i.e. '6' for 60 knots, '1' for 100 knots), the next two numbers the controller phase (i.e. 'BL' for baseline, '33' for 330 degrees) and the last letter indicated which group of files (i.e. '_A' for the first group, '_E' for the last group).

Each closed loop test data file was given a 7 character file name. The first two letters indicated

mode (i.e. 'CL' for closed loop), the third number indicated airspeed, and the last two or three characters indicated HHC on or off (i.e. 'HHC' for HHC on, and 'BL' for baseline).

Open Loop Data

L***_A.DAT

1000	M.R. Pitch Link Load B1	Lbs	250 Hz
1001	M.R. Blade Flapwise Bending @ 15%	In-lbs	250 Hz
1002	M.R. Blade Flapwise Bending @ 50%	In-lbs	250 Hz
1003	M.R. Blade Chordwise Bending @ 17%	In-lbs	250 Hz
1004	M.R. Mast Longitudinal Bending @ W.L. 68.25	In-lbs	250 Hz
1005	M.R. Mast Lateral Bending @ W.L. 68.25	In-lbs	250 Hz
1006	Longitudinal Load Link	Lbs	
1009	M.R. Mast Longitudinal Bending @ W.L. 73.0	In-lbs	250 Hz
1010	M.R. Mast Lateral Bending @ W.L. 73.0	In-lbs	250 Hz
1038	M.R. Pitch Link Load B2	Lbs	250 Hz

L***_B.DAT

1020	M.R. Torque	In-lbs	250 Hz
1022	M.R. Blade Chordwise Bending @ 50%	In-lbs	250 Hz
1024	M.R. Blade Flapwise Bending @ 20%	In-lbs	250 Hz
1025	M.R. Blade Flapwise Bending @ 30%	In-lbs	250 Hz
1026	M.R. Blade Flapwise Bending @ 70%	In-lbs	250 Hz
1027	M.R. Blade Torsion @ 17%	In-lbs	250 Hz
1028	M.R. Blade Torsion @ 50%	In-lbs	250 Hz
1030	M.R. Blade Flapwise Bending @ 90%	In-lbs	250 Hz
9017	HHC Left Lateral Actuator Position	In-lbs	250 Hz
9026	HHC Right Lateral Actuator Position	In-lbs	75 Hz

L***_C.DAT

9028	HHC Longitudinal Actuator Position	In-Lbs	250 Hz
1103	Tailboom Vertical Bending @ Sta 211	In-lbs	
1104	Tailboom Lateral Bending @ Sta 211	In-lbs	
1200	Collective Control Rod Load	In-lbs	
1201	HHC Longitudinal Actuator Load No. 3	Lbs	75 Hz
1202	HHC Left Lateral Actuator Load	Lbs	75 Hz
1203	HHC Right Lateral Actuator Load	Lbs	75 Hz
2002	Boom Static Pressure	FSI	
2124	Boom Airspeed	Knots	
3002	Exhaust Gas Temperature	Deg C	

L***_D.DAT

5008	Vertical Accel - Right Seat	G's	75 Hz
5009	Lateral Accel - Right Seat	G's	75 Hz
5010	Longitudinal Accel - Right Seat	G's	75 Hz
5052	HHC Longitudinal Feedback Accelerometer	G's	250 Hz
5053	HHC Lateral Feedback Accelerometer	G's	250 Hz
5054	HHC Vertical Feedback Accelerometer	G's	250 Hz
6007	C.G. Vertical Acceleration Sta 100	G's	6 Hz
6008	C.G. Lateral Acceleration Sta 100	G's	6 Hz
6009	C.G. Longitudinal Acceleration Sta 100	G's	6 Hz
6010	Vertical Acceleration at C.G. High Frequency	G's	250 Hz

L***_E.DAT

6011	Lateral Acceleration at C.G. High Frequency	G's	250 Hz
6012	Longitudinal Acceleration at C.G. High Frequency	G's	250 Hz
9003	Lead Lag Angle M.R. 1	Deg	250 Hz
9001	Main Rotor Flap Angle Blade 1	Deg	250 Hz
9002	Feathering Angle M.R.1	Deg	250 Hz
9027	M.R. Azimuth Index	Counts	250 Hz
8002	HHC ECU Sine Reference Output	Sin/Cos	
8003	HHC ECU Cosine Reference Output	Sin/Cos	
7001	Main Rotor RPM	PercentM	

Closed Loop Data

CL*HHC.DAT or CH*BL.DAT

5008	Vertical Accel - Right Seat	G's	75 Hz
5009	Lateral Accel - Right Seat	G's	75 Hz
5010	Longitudinal Accel - Right Seat	G's	75 Hz
6010	Vertical Accel at C.G. at high frequency	G's	250 Hz
6011	Lateral Accel at C.G. at high frequency	G's	250 Hz
6012	Longitudinal Accel at C.G. at high frequency	G's	250 Hz
9017	HHC Left Actuator Position	In	75 Hz
9026	HHC Right Actuator Position	In	75 Hz
9027	HHC Longitudinal Actuator Position	In	75 Hz

LIST OF REFERENCES

- 1.1 Cronhike, J. D., Berry, V. L., Dompka, R. V., "Summary of the Modeling and Test Correlations of a NASTRAN Finite Element Vibrations Model for the AH-1G Helicopter," NASA CR 178201, January, 1987.
- 2.1 Bramwell, A. R. S., "Helicopter Dynamics," Edward Arnold Publishers, London, 1976.
- 2.2 Prouty, R. W., "Helicopter Performance, Stability, and Control," Prindle, Weber and Schmidt Publishers, Boston, MA, 1986.
- 2.3 Johnson, W., "Helicopter Theory," Princeton University Press, Princeton, NJ, 1980.
- 2.4 Gessow, A. and Myers, G. C., "Aerodynamics of the Helicopter," Frederick Ungar Publishing, 1952.
- 2.5 Gunsallus, C. T., Pellum, W. L., and Flannelly, W. G., "Holometrics: An Information Transformation Methodology," paper presented at the American Helicopter Society 44th Annual Forum, Washington, D. C., June, 1988.
- 3.1 Johnson, W., "A Comprehensive Analytical Model of Rotorcraft Aerodynamics and Dynamics - Part II," NASA Technical Memorandum 81183.
- 3.2 Sangha, K. B., "Bearingless Rotors and Higher Harmonic Control Modeling using Racap," McDonnell Douglas Helicopter Company, Mesa, Az.
- 3.3 Nygren, K. P. and Schrage, D. P., "Fixed-Gain versus Adaptive Higher Harmonic Control Simulation," Journal of the American Helicopter Society, pp. 51- 58, July 1989.
- 3.4 Daughaday, H., "Suppression of Transmitted Harmonic Rotor Loads by Blade Pitch Control," Proceedings of the 23rd Annual National Forum of the American Helicopter Society, pp. 65-82, Washington, D. C., May, 1967.
- 3.5 Shaw, J., "Higher Harmonic Blade Pitch Control for Helicopter Vibration Reduction: A Feasibility Study," MIT Report ASRL TR 150-1, Dec. 1968.

- 3.6 Balcerak, J. C. and Erickson, J. C., Jr., "Suppression of Transmitted Harmonic Vertical and Inplane Rotor Loads by Blade Pitch Control," USAAVLABS Technical Report 69-39, July 1969.
- 3.7 McHugh, F. and Shaw, J., "Helicopter Vibration Reduction with Higher Harmonic Blade Pitch," Journal of the American Helicopter Society, pp. 63-77, 1978.
- 3.8 Yen, Jing G., "Higher Harmonic Control for Helicopters with Two-Bladed and Four-Bladed Rotors," Journal of Aircraft, vol. 18, no. 12, pp. 1064-1069, December 1981.
- 3.9 Chopra, I. and McCloud, J. L., III, "A Numerical Simulation Study of Open-Loop, Closed-Loop and Adaptive Multicyclic Control Systems," Journal of the American Helicopter Society, pp. 63-77, January 1983.
- 3.10 Johnson, W., "Self-tuning Regulators for Multicyclic Control of Helicopter Vibration," Tech. Rep., NASA, 1982, Technical Paper 1996.
- 3.11 Gupta, N. and Du Val, R., "A New Approach for Active Control of Rotorcraft Vibration," Journal of Guidance, Control and Dynamics, vol. 5, no. 2, pp. 143-150, 1982.
- 3.12 Molusis, J., "The Importance of Nonlinearity in the Higher Harmonic Control of Helicopter Vibration," 39th Annual Forum of the American Helicopter Society, pp. 624-627, 1983.
- 3.13 Ham, N, " Helicopter Individual-Blade-Control research at MIT 1977-1985," Vertica, vol. 11, no. 1/2, pp. 109-122, 1987.
- 3.14 Davis, M. W., "Refinement and Evaluation of Helicopter Real-Time Self Adaptive Active Vibration Controller Algorithms," NASA CR 3821, November 1983.
- 3.15 Jacklin, S. A., "Adaptive Inverse Control for Rotorcraft Vibration Reduction," NASA TR 86829, October 1985.

- 3.16 Hanagud, S., Meyyappa, M., Sarkar, S., and Craig, J. I., "A Coupled Rotor/Airframe Vibration Model with Higher Harmonic Control Effects," presented at 42nd Annual Forum of the American Helicopter Society, Washington, D. C., 1986.
- 3.17 Robinson, L. H. and Friedmann, P. P., "Analytic Simulation of Higher Harmonic Control Using a New Aeroelastic Model," presented at the 30th AIAA SDM Conference, Mobile, AL, April, 1989.
- 3.18 Hall, S. R. and Wereley, N. M., "Linear Control Issues in the Higher Harmonic Control of Helicopter Vibrations," presented at the 45th Annual Forum of the American Helicopter Society, Boston, MA, May, 1989.
- 3.19 McCloud, J. L., III, "Multicyclic Jet-Flap Control for Alleviation of Helicopter Blade Stresses and Fuselage Vibration," Rotorcraft Dynamics, NASA SP-352, 1974.
- 3.20 Sissingh, G. J. and Donham, R. E., "Hingeless Rotor Theory and Experiment on Vibration Reduction by Periodic Variation of Conventional Control," Rotorcraft Dynamics, NASA SP-352, 1974.
- 3.21 Wood, E. R., Powers, R. W., and Hammond, C. E., "On Methods for Application of Harmonic Control," Vertica, Vol. 4, (1), 1980.
- 3.22 Shaw, J. and Albion, N., "Active Control of the Helicopter Rotor for Vibration Reduction," presented at 36th Annual Forum of the American Helicopter Society, Washington, D. C., May 1980.
- 3.23 Hammond, C. E., "Wind Tunnel Results Showing Rotor Vibratory Loads Reduction using Higher Harmonic Blade Pitch," presented at the 36th Annual Forum of the American Helicopter Society, Washington, D.C., May 1980.
- 3.24 Molusis, J. A., Hammond, C. E. and Cline, J. H., "A Unified Approach to the Optimal Design of Adaptive and Gain Scheduled Controllers to achieve minimum Helicopter Rotor Vibration," Proceedings of the 37th Annual Forum of the American Helicopter Society, New Orleans, LA, May 1981.

- 3.25 Shaw, J., Albion, N., Hanker, E. J., Jr. and Teal, R. S., "Higher Harmonic Control: Wind Tunnel Demonstration of Fully Effective Vibratory Hub Force Suppression," Journal of the American Helicopter Society, pp. 14-25, January 1989.
- 3.26 Wernicke, R. K. and Drees, J. M., "Second Harmonic Control," Proceedings of the 19th Annual National Forum of the American Helicopter Society, Washington, D.C., May 1963.
- 3.27 Wood, E. R., Powers, R. W., Cline, J. H. and Harwood, C. E., "On Developing and Flight Testing a Higher Harmonic Control System," Journal of the American Helicopter Society, pp. 3-20, January 1985.
- 3.28 Wood, E. R. and Powers, R. W., "Practical Design Considerations for a Flightworthy Higher Harmonic Control System," Proceedings of the 36th Annual Forum of the American Helicopter Society, Washington, D.C., May 1980.
- 3.29 Straub, F. K. and Byrns, E. V., Jr., "Application of Higher Harmonic Blade Feathering on the OH-6A Helicopter for Vibration Reduction," NASA CR 4031, 1986.
- 3.30 Walsh, D. M., "Flight Tests of an Open Loop Higher Harmonic Control System on an S-76A Helicopter," presented at the 42nd Annual Forum of the American Helicopter Society, Washington, D.C., 1986.
- 3.31 Miao, W., Kottapalli, S. and Frye, H., "Flight Demonstration of Higher Harmonic Control (HHC) on S-76," presented at the 42nd Annual Forum of the American Helicopter Society, Washington, D.C., 1986.
- 3.32 Polychroniadis, M. and Achache, M., "Higher Harmonic Control: Flight Tests of an Experimental System on SA 349 Research Gazelle," presented at the 42nd Annual Forum of the American Helicopter Society, Washington, D.C., 1986.
- 4.1 Otnes, R. K. and Enochson, L., "Applied Time Series Analysis," John Wiley and Sons, New York, NY, 1978.

- 5.1 Press, Flannery, Teukolsky, and Vetterling, "Numerical Recipes," Cambridge University Press, MA, 1986.
- 5.2 Turner, J. D., "Instrumentation for Engineers," Springer-Verlag New York Inc., NY, 1988.
- 5.3 Marple, S. L., "Digital Spectral Analysis with Applications," Prentice-Hall, Inc., Englewood Cliffs, NJ, 1987.
- 5.4 Kay, S. M., "Modern Spectral Estimation," Prentice-Hall, Englewood Cliffs, NJ, 1988.
- 6.1 Moon, F. C., "Chaotic Vibrations," John Wiley & Sons, New York, NY, 1987.
- 6.2 Crutchfield, J. P., Farmer, J. D., Packard, N. H., and Shaw, R. S., "Chaos," Scientific American, pp. 46 to 57,
- 6.3 Cvitanovic, P. and Predrag, P, "Universality in Chaos," Heyden, Philadelphia, PA, 1984.
- 6.4 Blacher, S. and Perdang, J., "The Power of Chaos," Physica 3D, North-Holland Publishing Co., pp. 512-529, 1981.
- 6.5 Packard, N. H., Crutchfield, J. P., Farmer, J. D., and Shaw, R. S., "Geometry from a Time Series," Physical Review Letters, Vol. 45, No. 9, pp. 712-716, September 1980.
- 6.6 Takens, F., "Detecting Strange Attractors in Turbulence," Lecture Notes in Mathematics, Springer Verlag, Vol 898, 1981.
- 6.7 Abraham, R. H. and Shaw, C. D., "Dynamics: the Geometry of Behavior," Aerial Press, Santa Cruz, CA., 1983.
- 6.8 Thompson, J. M. T. and Stewart, H. B., "Nonlinear Dynamics and Chaos," John Wiley and Sons, New York, NY, 1986.
- 6.9 Wolf, A., Swift, J. B., Swinney, H. L., and Vastano, J. A., "Determining Lyapunov Exponents from a Times Series," Physica 16D, North-Holland, Amsterdam Publishing Co., pp. 285 to 317, 1985.

- 6.10 Eckmann, J. P., Kamphorst, S. O., Ruelle, D., and Ciliberto, S., "Liapunov exponents from time series," *Physical Review A*, Vol 34, No. 6, pp. 4971 to 4979, December 1986.
- 6.11 Tongue, B. H. and Smith, D., "Determining Lyapunov Exponents by means of Interpolated Mapping," *Journal of Applied Mechanics*, Vol 56, pp. 691 to 696, September 1989.
- 6.12 Mandelbrot, B. B., "Fractals, Form, Chance, and Dimension," W. H. Freeman, San Francisco, CA., 1977.
- 6.13 Guckenheimer, J. and Holmes, P., "Nonlinear Oscillations, Dynamical Systems, and Bifurcations of Vector Fields," Springer-Verlag, New York, NY, 1983.
- 6.14 Roux, J. C., Simoy, R. H., and Swinney, H. L., "Observation of a Strange Attractor," *Physica 8D*, North-Holland Publishing Co., pp. 257-266, 1983.
- 6.15 Berge, P., Pomeau, Y. and Vidal, C., "Order within Chaos," John Wiley and Sons, New York, NY, 1984.
- 6.16 Farmer, J. D., Ott, E., and Yorke, J. A., "The Dimension of Chaotic Attractors," *Physica 7D*, North-Holland Publishing Co., Amsterdam, pp. 153 to 180, 1983.
- 6.17 Malraison, B., Atten, P., Berge, P. and Dubois, M., "Dimension of strange attractor: an experimental determination for the chaotic regime of two convective systems," *Journal de Physique, Letters 44*, pp. 897 to 902, November 1983.
- 6.18 Froehling, H., Crutchfield, J. P., Farmer, D., Packard, N. H., and Shaw, R., "On Determining the Dimension of Chaotic Flows," *Physica 3D*, North-Holland Publishing Co., pp. 605 to 617, 1981.
- 6.19 Grassberger, P. and Proccacia, I., "Characterization of Strange Attractors," *Physics Review Letters*, No 50, pp 346 to 349, 1983.

- 10.1 Shaw, R., "Strange Attractors, Chaotic Behavior, and Information Flow," Z. Naturforsch 36A, No. 80, 1981.
- 10.2 Osborne, A. R. and Provenzale, A., "Finite Correlation Dimension For Stochastic Systems with Power-Law Spectra," Physica D35, North-Holland Publishing Co., Amsterdam, pp. 357 to 381, 1989.

INITIAL DISTRIBUTION LIST

1. Defense Technical Information Center 2
Cameron Station
Alexandria, VA 22304-6145
2. Library, Code 0142 2
Naval Postgraduate School
Monterey, CA 93943-5002
3. Professor R. Kolar 20
Code 67Kj
Department of Aeronautics & Astronautics
Naval Postgraduate School
Monterey, CA 93943-5000
4. Professor Nesrin Sarigul-Klijn 10
University of California, Davis
Dept. of Mech, Aero, & Material Eng.
Bainer Hall
Davis, CA 95616
5. Dr. Mamiyama, T. S. 1
Director Aircraft Division, AIR-931
Room 430 JP-1
Naval Air Systems Command
Washington, D. C. 20361
6. Dr. Robert E. Singleton 1
Director, Engineering Sciences Div
U. S. Army Research Center
Box 12211
Research Triangle Park, NC 27709